Summer 2021

Anisotropic Plasticity Modeling of Thin Sheets and Its Application to Micro Channel Forming of Steel Foils

Jie Sheng
Southern Methodist University, sheng@smu.edu

ANISOTROPIC PLASTICITY MODELING OF THIN SHEETS AND ITS APPLICATION TO MICRO CHANNEL FORMING OF STEEL FOILS

Approved by:

Prof. Wei Tong
Mechanical Engineering
Dissertation Committee Chairperson

Prof. Radovan Kovacevic
(Mechanical Engineering)

Prof. Xu Nie
(Mechanical Engineering)

Prof. David Willis
(Mechanical Engineering)

Prof. Brett Story
(Civil and Environmental Engineering)

Prof. Usama El Shamy
(Civil and Environmental Engineering)

ANISOTROPIC PLASTICITY MODELING OF THIN SHEETS AND ITS APPLICATION TO MICRO CHANNEL FORMING OF STEEL FOILS

A Dissertation Presented to the Graduate Faculty of the

Bobby B. Lyle School of Engineering

Southern Methodist University

in

Partial Fulfillment of the Requirements

for the degree of

Doctor of Philosophy

with a

Major in Mechanical Engineering

by

Jie Sheng

M.S., Mechanical Engineering, Lehigh University
B.Eng., Process Equip. and Control Engineering, East China Uni. of Sci. and Tech.

August 4, 2021

ACKNOWLEDGMENTS

I would like to express my appreciation and endless gratitude to my advisor, Professor Wei Tong, who never let me lose my motivation and was always available and patient for support whenever I needed him over the years. His ability to question the existing and come up with new ideas is surely what has shaped and guided me to where I am today. I would like to extend my sincere thanks to every member of my supervisory committee for taking the time to evaluate my dissertation and defense, who has a significant influence on my academic career and professional development. I also want to thank my colleagues, collaborators, and sponsors (General Motors and Sandia National Laboratories), without their help and financial supports, this work would not have been possible.

I am truly grateful for the continuous supports and aids from my friends, and a special thanks to my family for their endless supports, encouragement, and care throughout my studies.

Sheng, Jie M.S., Mechanical Engineering, Lehigh University, 2015
B.Eng., Process Equip. and Control Eng., East China Uni. of Sci. & Tech., 2012

Anisotropic Plasticity Modeling of Thin Sheets and
Its Application to Micro Channel Forming of Steel Foils

Advisor: Prof. Wei Tong

Doctor of Philosophy conferred August 4, 2021

Dissertation completed August 4, 2021

Thin sheet metals and ultrathin metal foils produced by industrial rolling processes are textured polycrystalline materials and their mechanical behaviors may depend strongly on the orientation of applied loading. Consideration of such plastic anisotropy in advanced modeling of these materials is of the paramount importance in designing optimal manufacturing processes for automotive and other applications using finite element methods. This research addresses several critical issues in anisotropic plasticity modeling and its applications in analyzing micro channel forming of ultrathin stainless-steel foils. An experimental study has first been carried out on the accuracy and sensitivity of measuring the plastic strain ratios of an aluminum alloy AA6111-T4 thin sheet under uniaxial tension by digital image correlation. The plastic strain ratios are found to be virtually constant at the axial strain of 2% and beyond. Besides large measurement uncertainties at small strains, non-homogeneous deformation and out-of-plane translation of test coupon are found to be the main causes of their observed variations. With the aid of extensive numerical optimization calculations, a theoretical analysis has then been conducted to evaluate two formulations of convex fourth-order stress functions. Gotoh's yield function is found to be more capable and better suited for parameter identification while fourth-order Yld2000 function may be used to convexify a calibrated but non-convex Gotoh's yield function with reduced plastic anisotropy. Polycrystalline plasticity modeling has subsequently been considered to account for the discrete nature of individual grains in ultrathin foils. A quadratic crystal plasticity

model of FCC single crystals with orthotropic plastic anisotropy has been successfully calibrated using finite element polycrystal plasticity modeling and uniaxial tension test data. Both macroscopic and polycrystalline plasticity models have been successfully incorporated in finite element analyses of micro channel forming of 304L stainless steel thin foils. Plastic anisotropy, grain heterogeneity distribution, strain hardening, and contact friction are all shown to affect the springback of the formed micro-channels and polycrystalline finite element simulations provide an improved prediction of experimentally measured springback.

TABLE OF CONTENTS

LIST OF FIGURES

LIST OF TABLES

LIST OF SYMBOLS

$R_\theta, \bar{R}, R_b$	The plastic strain rate ratio or the plastic strain ratio when the tensile loading axis is at angle θ from the rolling direction ,the average plastic strain ratio, and plastic strain ratio under equal biaxial tension
ε_a, ε_a^e, ε_a^p, $\mathrm{d}\varepsilon_a^p$	The total axial strain, the elastic axial strain, the true plastic axial strain and the true plastic axial strain increment
ε_w, ε_w^p, $\mathrm{d}\varepsilon_w^p$	The total width strain, the true plastic width strain and the true true plastic width strain increment
ε_t, ε_t^p, $\mathrm{d}\varepsilon_t^p$	The total thickness strain, the total true thickness strain and the true thickness strain increment
E, ν	Young's modulus and Poisson's ratio
A_0, A	The initial and current (deformed) cross-section area
d, D	The amount of out-of-plane translation of the tensile sample towards the camera and the camera-to-object distance
x, y, z	The rolling (RD), transverse (TD), normal (ND) directions of an orthotropic material symmetry axes
$\sigma_x, \sigma_y, \sigma_z,$ $\tau_{xy}, \tau_{yz}, \tau_{xz}$	The Cartesian components of an applied Cauchy stress $\boldsymbol{\sigma}$ in the orthotropic coordinate system of material
$\sigma_f, \bar{\sigma}$	The current yield strength and equivalent stress of material

$\dot{\boldsymbol{\varepsilon}}^p, \dot{\bar{\varepsilon}}^p$ The plastic strain increments and equivalent plastic strain increment of flow rule

$\Phi_g, A_1, A_2, ..., A_9$ Gotoh's 1977 fourth-order anisotropic yield stress function in Cartesian stress components and its five on-axis ($A_1, ..., A_5$) and four off-axis ($A_6, ..., A_9$) polynomial coefficients or material constants.

ϕ_g Gotoh's 1977 fourth-order yield function in principle plane stress (σ_1, σ_2) and loading angle θ

$F(\theta), G(\theta), H(\theta)$ The Fourier cosine series of Gotoh's 1977 fourth-order yield function in principle plane stress

$2\Phi_{2k}^{(\alpha)}, \alpha_1, \alpha_2, ..., \alpha_8$ The fourth-order Yld2000-2d by Barlat et al. and its eight polynomial coefficients(material constants)

$2\Phi_{2k}^{(\beta)}, \beta_1, \beta_2, ..., \beta_8$ The fourth-order Yld2000-2d by Aretz et al. and its eight polynomial coefficients(material constants)

$\phi_{gio}(\sigma_1, \sigma_2)$ In-plane isotropic Gotoh's 1977 fourth-order yield function

σ_θ, σ_b The yield stress when the tensile loading axis is at angle θ from the rolling direction and yield stress under equal biaxial tension

η_0, b The plastic thinning ratio and stress ratio of the mechanical property space

$\bar{\tau}_s, \dot{\varepsilon}^p$ The stress-based plastic potential and plastic strain rate for continuum plasticity

$\bar{\gamma}^p, \dot{\bar{\gamma}}^p$ The equivalent plastic strain and equivalent plastic strain rate of a flow or yield function

τ_f, τ_{vf} The equivalent visocoplastic flow strength of a rate-independent and rate-dependent material

$\boldsymbol{m}^{(\alpha)}$ and $\boldsymbol{s}^{(\alpha)}$ The normal vector and the slip direction of α^{th} slip system, α =1,...,N

$\dot{\tau}^{(\alpha)}$, b, $\tau_0^{(\alpha)}$, w_α The crystallographic slip rate, power exponent, slip resistance, and weight coefficient of the slip potential of each individual slip system

$\Phi_2(\boldsymbol{\sigma_d})$,$A_1$,...,$A_{15}$ The general quadratic plastic potential or yield stress function of macroscopic anisotropic plasticity in material coordinate system with its material constants (A_1,...,A_{15})

$\Phi_2(\boldsymbol{\sigma_d^*})$,$a_1$,...,$a_{15}$ The general quadratic plastic potential or yield stress function of macroscopic anisotropic plasticity in crystal coordinate system with its material constants (a_1,...,a_{15})

Φ_{2fcc} The quadratic plastic potential of an FCC single crystal may be associated with its crystallographic slips in a micromechanical multi-surface plasticity theory

$\tau^{(1)}$,$\tau^{(2)}$,...,$\tau^{(12)}$ The resolved shear stresses of the quadratic plastic potential of twelve slip systems in the FCC crystal

w_1,w_2,...,w_{12} The non-negative weights related to the relative slip resistance of twelve slip systems in the FCC crystal

ϕ_{2m} The reduced number of independent polynomial coefficients of $\Phi_2(\sigma^*)$ and crystallographic slip weights of quadratic plastic potential $\Phi_{2fcc}(\sigma^*)$ for monoclinic anisotropy

ϕ_{2o} The reduced number of independent polynomial coefficients of $\Phi_2(\sigma^*)$ and crystallographic slip weights of quadratic plastic potential $\Phi_{2fcc}(\sigma^*)$ for orthotropic anisotropy

ϕ_{2ia} The reduced number of independent polynomial coefficients of $\Phi_2(\sigma^*)$ and crystallographic slip weights of quadratic plastic potential $\Phi_{2fcc}(\sigma^*)$ for in-plane axial isotropy

ϕ_{2ip} The reduced number of independent polynomial coefficients of $\Phi_2(\sigma^*)$ and crystallographic slip weights of quadratic plastic potential $\Phi_{2fcc}(\sigma^*)$ for in-plane isotropy

ϕ_{2c} The reduced number of independent polynomial coefficients of $\Phi_2(\sigma^*)$ and crystallographic slip weights of quadratic plastic potential $\Phi_{2fcc}(\sigma^*)$ for cubic anisotropy

$\mathbf{Q}$, $\mathbf{e}'_{RD}$, $\mathbf{e}'_{TD}$, $\mathbf{e}'_{ND}$ The coordinate transformation matrix and unit vectors of RD,TD and ND axes expressed in the crystal coordinate system

ϕ_1,Φ,ϕ_2 The Bunge convention of Euler angle

θ,ψ,ω The Rodriguez (crystal orientation) angles

d_1,d_2,d_3,c,s The parameters of the Rodriguez formula for the rotated cubix axes

$\Psi_2(\dot{\boldsymbol{\varepsilon}}_d)$,$B_1$,...,$B_{15}$ The general quadratic plastic strain rate potential of macroscopic anisotropic plasticity in material coordinate system with its material constants (B_1,...,B_{15})

$\Phi_{2o}^{(k)}(\boldsymbol{\sigma}_d)$, $\Psi_{2o}^{(k)}(\dot{\boldsymbol{\varepsilon}}_d)$ The quadratic yield stress function for each orthotropic quartet of single crystals and its dual plastic strain-rate function.

$K, V^{(k)}$ The number of constituent single crystals and volume fraction of individual texture components or single crystals with $V^{(k)} = 1/K$

$\bar{\Phi}_{2o}^{S}(\boldsymbol{\sigma}_d)$, $\Psi_{2o}^{(k)}(\dot{\boldsymbol{\varepsilon}}_d)$ The Sachs quadratic yield stress function and the Taylor quadratic strain-rate function

$\Phi_h(\boldsymbol{\sigma})$ General Hill's 1948 quadratic yield stress function

F, G, H, J, M, N The constants of General Hill's 1948 quadratic yield stress function

R_{ij} The yield stress ratio in the ij direction for ANSYS plasticity inputs

P,t,D,R,γ P is half length of pitch, t is the thickness of test specimen, D is depth, R and γ are the radius and the central angle of the curve part.

φ_d,φ_f,$\triangle\varphi$ φ_d is the rotated angle by rotating punch or lower die to match the drawn box, t is the thickness of test specimen, φ_f is the rotated angle by rotating foil specimen after removing loads to match the drawn box, and $\triangle\varphi$ is angle difference between these two angles

H_d,H_f,$\triangle H$ H_d is the height of punch or lower die (peak to valley), H_f is the height of deformed foil (peak to valley), and $\triangle H$ is height reduction between these two heights

$\triangle H_{\mathrm{E}}^{\mathrm{L}}$,$\triangle \varphi_{\mathrm{E}}^{\mathrm{L}}$ The height reduction and springback angle measured via local measurement method for experiments

$\triangle H_{\mathrm{E}}^{\mathrm{G}}$,$\triangle \varphi_{\mathrm{E}}^{\mathrm{G}}$ The height reduction and springback angle measured via global measurement method for experiments

$\triangle H_{\mathrm{F}}^{\mathrm{L}}$,$\triangle \varphi_{\mathrm{F}}^{\mathrm{L}}$ The height reduction and springback angle measured via local measurement method for simulations

$\triangle H_{\mathrm{F}}^{\mathrm{G}}$,$\triangle \varphi_{\mathrm{F}}^{\mathrm{G}}$ The height reduction and springback angle measured via global measurement method for simulations

Chapter 1
INTRODUCTION

1.1 Motivation

Metallic products from farming tools to the aircraft industries have been widely accepted and used in our daily life due to their good malleability and ductility [1]. There are several approaches to shape a metal piece into a particularly designed geometry, such as machining, forming [2,3], and joining or welding. Metal forming is a process that reshapes a metal piece without or with little adding or removing the material [4], like tensile forming, compressive forming, and hydroforming, etc. Among various sheet-metal forming processes, stamping is the one commonly used in the fabrication of complex parts since it is a mass-production economical process [5, 6]. Many metallic materials have face-centered cubic (FCC) crystallographic structures, including aluminum and copper alloys, austenitic stainless steels, etc. A6111-T4 aluminum alloy thin sheet is one of the leading materials used to produce the vehicle body due to its good properties, like high strength, good corrosion resistance, lightweight [6–9]. Microforming is to down-scale the products to micro-scale specimens using commercial laboratory equipment to complete the associate tests. In micro channel forming, stainless steel 304L (SS304L) ultrathin foil is one of the popular materials studied for possible applications in fuel-cell bipolar plates [10–12].

Formality and dimensional accuracy are two primary considerations for a micro channel forming application. For down-scaled specimens, how to minimize the variations on dimensions is a crucial task in such processes. Material properties and sheet metal thickness are two factors that may lead to the inaccuracy on final dimensions of the formed parts. Depending on the thickness of the to-be-used material, it is broadly categorized into three types: plate metal, sheet metal, and metal foil [4, 13]. Metal foil refers to a very thin sheet that has been rolled flat by a machine, about 0.2 mm thick or less, while sheet metal is a thicker

material compared with foil but thinner than a thick metal plate. Any metal sheet with a thickness of 6 mm or more is considered as plate metal. Metal with different thickness may have varied uses depending on the durability and weight requirements.

The plastic deformation caused by material anisotropy is one of the main concerns for improving metal forming design and analysis. There are two major aspects of the metal plastic anisotropy involved of yielding and plastic flow. They are to be modeled via yield stress functions and associated flow rules. Unlike an isotropic material, which has identical properties in all loading directions, the mechanical properties of an anisotropic material change along with loading directions with respect to the material symmetry axes. Anisotropic plastic behaviors of widely used industrial products such as the thin rolled sheet, ultrathin foil, and so on have been studied over the years [13–19]. Some researchers have focused on improving constitutive models via better experimental calibration to obtain more accurate and efficient numerical simulations [20, 21]. Others have studied the relevant experimental and computational methods with different material types and test conditions to understand and predict the plastic responses, such as the Bauschinger effect [22–29].

For a polycrystalline metal alloy, its anisotropic plastic properties are considered as the results of the collective motion of dislocations on certain crystallographic planes in single crystal grains [30,31]. Understanding the grain-level material behaviors will provide crucial information to develop best constitutive formulations and numerical models used to predict and simulate the corresponding material responses in macro-scale experiments. Two approaches in metal plasticity modeling have been employed over the years: macroscopic and micromechanical. The macroscopic or mathematical theory of plasticity is to consider a polycrystalline metal as an anisotropic solid without explicitly accounting for its microstructural details, while the micromechanical or physical theory of plasticity is to explicitly incorporate the effect of the crystallographic slips of single crystal grains in the polycrystalline aggregates [32–36].

1.2 Objectives

The current research focuses on improving the anisotropic plasticity modeling and its applications of thin sheet metals and ultrathin foils (such as AA6111-T4 and SS304L) through

experimental investigations, macroscopic and polycrystal plasticity modelings, and numerical simulations. The specific four topics have been studied in this dissertation, and the objectives of studying each topic are summarized in the following.

Rolled sheet metals are in general textured polycrystalline solids and their plastic flow behavior depends on the sheet metal orientations [34,35]. Based on the material behaviors, a sheet metal may be classified and modeled as an isotropic or anisotropic material. The R-value, which is also known as the Lankford coefficient, is probably one of the simplest approaches to describe the plastic flow pattern of the plastic anisotropy of sheet metals at various stress states [35,37,38]. In most studies, two measurement methods or definitions of the R-value have been used: the plastic strain rate ratio and the plastic strain ratio. When the R-value is treated as a constant as often being the case in the past, both definitions of the R-value are equivalent. However, some recent publications report that the R-value may strongly depend on the accumulated plastic strain [39], so anisotropic hardening may have to be incorporated in modeling. Therefore, an accurate and precise measurement of the plastic strain ratio is first carefully assessed experimentally for an aluminum alloy AA6111-T4 sheet metal.

Two formulations of fourth-order orthotropic yield functions in plane stress are the simplest non-quadratic case in the advanced anisotropic plasticity modeling in the literature [20, 36, 40, 41] : Gotoh's complete fourth-order polynomial with nine coefficients and Yld2000-2d function with eight material constants and a stress exponent of four. While a calibrated Yld2000 yield function is automatically guaranteed to be convex while the convexity of a calibrated Gotoh's yield function requires further certification. On the other hand, Yld2000 function is less capable than Gotoh's yield function with less material constants and its parameter identification is highly nonlinear and non-unique. The question about how to best develop a convex fourth-order yield function of a sheet metal is thus investigated next through extensive numerical evaluations.

Due to the limited number of grains distributed across the thickness of ultrathin steel foil, explicit crystal plasticity modeling of grains may be needed in analyzing micro channel forming of the foil. It is well known that the plasticity of metal crystals at ambient conditions takes place primarily due to collective motion of dislocations on certain crystallographic

planes [30–33, 42]. Such plastic deformation within a single crystal has been treated as smooth (continuous) and homogeneous simple shear deformations occurring on activated slip systems [43–45]. A continuum crystal plasticity model of single crystals is thus the basis of polycrystalline modeling of the steel foil. In particular, upon the derivation of a quadratic plastic potential (yield stress function) of a FCC single crystal based on crystallographic slips, how to best estimate the slip systems weights and thus the material parameters of the yield stress function for single crystals is the central issue studied through polycrystalline modeling and uniaxial tension testing.

In automotive industries, sheet metal forming is one of the major processes commonly used in manufacturing, in which the upper punch and the lower die form the metal into a desired shape. To down-scale the size of a product such as a thin 304L stainless steel bipolar plate in a fuel cell, micro channel forming is one of the suitable methods for its mass production [11]. After channel forming, an extensive springback recovery of the formed parts may lead to an undesired dimensional variation or inaccuracy. Several factors including material properties and forming conditions may affect the final shape of the formed micro channels. Therefore, studies of so-called springback of the ultrathin stainless steel foil materials are necessary to improve the product quality and reduce the production cost. Both macroscopic and polycrystal models are introduced in finite element analyses to assess various factors that may influence the micro channel forming process and its springback prediction.

1.3 Outline

The experimental investigation, constitutive modeling, and numerical analysis on the above four specific topics in anisotropic plasticity study of thin sheet metals and ultrathin foils are described in the subsequent four chapters respectively. A more detailed introduction about the background and motivation of each research topic is included at the beginning of each following chapter. A brief outline of each chapter is first given in the following.

In Chapter 2, some experimental methods for achieving accurate and precise plastic strain ratio measurements via a series of uniaxial tensile tests with different angles between the tensile loading axis and the rolling direction of tensile coupon are investigated, including some common practices on plastic strain ratio measurements used in previous studies. Compared

with the contact measurement methods (i.e., extensometers), digital image correlation (DIC) is a non-contact optical technique applying to shape measurement and motion tracking, which provides a full-field strain data of elastic-plastic deforming materials [46, 47]. A new approach of plastic strain ratio measurements using a digital image-based full-field strain mapping technique and periodic unloading and reloading is introduced. The relevant analysis on possible sources of errors is discussed to evaluate the anisotropic plastic flow in thin sheet metals under uniaxial tension.

Chapter 3 evaluates Gotoh's complete fourth-order polynomial with nine coefficients and Yld2000-2d function with eight material constants and a stress exponent of four in anisotropic plasticity modeling of four selected sheet metals reported in the literature. Different sets of independent experimental inputs and additional modeling assumptions are introduced to identify all the parameters of two yield functions. Calibrated with the same three, five, seven, or eight independent experimental inputs, the similarities and differences between these two fourth-order yield functions in anisotropic plasticity modeling of the four selected sheet metals are investigated. A detailed discussion about the parameter calibrations and the associated polynomial coefficients or material constants of different sheet metals is included.

Chapter 4 investigates and calibrates the quadratic plastic potential for an FCC single crystal via macroscopic and polycrystal plasticity models. A possible method of identifying parameters of the quadratic plastic potential through the experimental uniaxial tensile test results and microtexture data is presented. A polycrystalline tensile bar is simulated using finite elements and rate-independent crystal plasticity. In such simulations, parameters of the quadratic yield function are different from one grain to another as they are dependent on the Bunge Euler angles contained in the EBSD data. The estimated slip system weights based on Sachs or Taylor model are used as an initial guess of the single crystal plasticity model parameters in the finite element polycrystalline analysis. A direct comparison between the FE-predicted and experimentally measured R-values is used to obtain final slip system weights for the single crystal plasticity model.

Chapter 5 focuses on the experimental study and numerical analysis of micro channel forming of ultrathin 304L stainless steel foils. Both macroscopic and polycrystalline plasticity modeling are used in the numerical simulations to assess the possible factors affecting the

springback of the formed SS304L micro channels. Possible effects of varying Young's modulus, contact friction, and strain hardening are considered and examined with the macroscopic plasticity model, and additional effects caused by grain heterogeneity distribution and plastic anisotropy are evaluated using the polycrystal plasticity model. For both experiments and simulations, the same two measurement methods of springback are used to evaluate the two simulation approaches in comparison with the experimental measurements.

Finally, Chapter 6 summarizes briefly the main results on the four topics as covered in detailed in Chapters 2-5. Some possible future research directions or efforts on further studying these topics are also given.

Chapter 2

ON THE ACCURATE MEASUREMENT OF R-VALUES OF FLAT SHEET METALS UNDER UNIAXIAL TENSION

2.1 Introduction

Rolled sheet metals are in general textured polycrystalline solids and their plastic flow behavior depends on the sheet metal orientations [34, 35]. The plastic anisotropy of a sheet metal can be in part characterized by its plastic flow pattern when the sheet metal is subjected to a simple stress state. The plastic strain rate ratio R, defined as the ratio of the true width strain increment $\mathrm{d}\varepsilon_w^p$ over the true thickness strain increment $\mathrm{d}\varepsilon_t^p$ (see p. 322-323 in [35]), is probably one of the simplest plastic flow pattern measures applied to a sheet metal loaded in uniaxial tension undergoing a true axial strain increment $\mathrm{d}\varepsilon_a^p$ (assuming plastic deformation is volume preserving $\mathrm{d}\varepsilon_a^p + \mathrm{d}\varepsilon_w^p + \mathrm{d}\varepsilon_t^p = 0$),

$$R(\varepsilon_a^p) = \frac{\mathrm{d}\varepsilon_w^p}{\mathrm{d}\varepsilon_t^p} = -\frac{\mathrm{d}\varepsilon_w^p}{\mathrm{d}\varepsilon_a^p + \mathrm{d}\varepsilon_w^p}. \tag{2.1}$$

As shown in Fig.2.1, a higher R-value will have a better resistance to thinning and a higher flow strength in biaxial tension [34, 48]. In practice, the plastic strain ratio R (also called the *Lankford coefficient* in some literature) is often used, which is defined as the ratio of the total true width strain ε_w^p over the total true thickness strain ε_t^p (see p.10 and p.311 in [49], p.452 in [50], p.271 in [48], p.72 and p.140 in [51]),

$$R(\varepsilon_a^p) \approx \tilde{R} = \frac{\varepsilon_w^p}{\varepsilon_t^p} = -\frac{\varepsilon_w^p}{\varepsilon_a^p + \varepsilon_w^p}. \tag{2.2}$$

If one assumes that the change of plastic strain rate ratio with axial elongation strain ε_a^p is negligible, then the two definitions are equivalent. This constancy of R-value is important when R is used to evaluate anisotropic flow potential constants in considering isotropic or

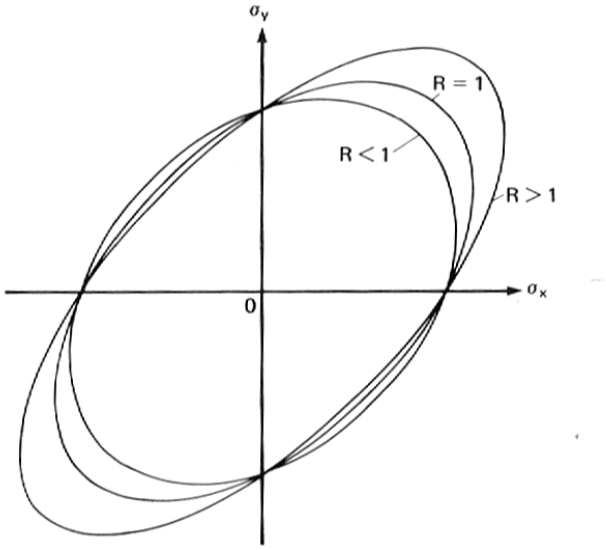

Figure 2.1: Schematic of biaxial yield surfaces of a planar isotropic sheet metal with various R-values.

anisotropic hardening behavior of a sheet metal [34, 48]. For example, when the Hill's 1948 anisotropic plastic flow potential is modified to account for the effects of back stresses or kinematic hardening, the resulting plastic strain ratios are found to be dependent on the plastic strain (especially at the small strain ranges, see [52, 53]). In this study, the term plastic strain ratio will be used for both definitions above but their calculation methods will be called *differential* (Eq.(2.1)) and *total* (Eq.(2.2)) strain methods, respectively.

As the plastic strain ratio values usually vary with the test direction, R_θ is used to indicate the plastic strain ratio measured when the tensile loading axis is at an angle θ from the rolling direction of the sheet metal. It is common to characterize a sheet metal material by an average R-values, $\bar{R}$, where

$$\bar{R} = \frac{R_0 + 2R_{45} + R_{90}}{4}. \tag{2.3}$$

Another parameter,

$$\Delta R = \frac{R_0 - 2R_{45} + R_{90}}{2}, \tag{2.4}$$

is also widely used to assess the earing height and location for deep drawing operations [34, 35, 48, 51]. These two parameters have also been computed via polycrystal orthotropic plasticity modeling via

$$\bar{R} = \frac{2}{\pi} \int_0^{\frac{\pi}{2}} R(\theta) \mathrm{d}\theta, \tag{2.5}$$

and

$$\Delta R = \frac{2}{\pi} \int_0^{\frac{\pi}{2}} |R(\theta) - \bar{R}| \mathrm{d}\theta. \tag{2.6}$$

A formability parameter B (also called the Backofen coefficient) is defined in terms of the uniaxial tension plastic strain ratios as well, namely [54]

$$B = \sqrt{\frac{(1 + R_0)(R_0 + 4R_0R_{90} + R_{90})}{4R_0(1 + R_0 + R_{90})}}. \tag{2.7}$$

The plastic strain ratio values and their changes upon rolling, annealing and further deformation can be used as a quality control measure for various manufacturing processes. R-values are also used to evaluate anisotropic flow potential constants in modeling parameter identification process. Accurate determination of plastic strain ratios is thus desirable and important. This study deals with the experimental measurement methods and the potential sources of errors in plastic strain ratio values. The focus here is to assess a new digital image based full-field strain mapping technique for determining the plastic strain ratios and its possible applications in studying the anisotropic plastic flow of sheet metals upon the changes in strain paths, at large plastic strains, and under simple stress states other than uniaxial tension.

2.2 A Sensitivity Analysis on the R-value Measurement Errors

Although details for R-value determination have been given by the ASTM Standard Test Method for Plastic Strain Ratio r for Sheet Metal (E517-00), the experimental procedures in practice vary somewhat [49]. Typically, up to ten different width and thickness measurements made in the central 2-in gage section of a tensile specimen at the maximum load point are used for computing the R-values. The width and thickness measurements are also made at 5%, 10%, 15% or other axial elongations, depending on the materials and individual labs. Because the thickness dimension is much smaller than the width and axial dimensions of

the tensile specimens, the axial elongations are often used instead of the sheet thickness. Before presenting the new measurement technique and associated data analysis procedure on R-values in flat sheet metals, a brief review of various R-value measurement methods and their potential sources of errors [55] are first summarized in this section.

2.2.1 Typical Sources of Measurement Errors

Depending on the instrument and calibration method used, the experimental procedures can be classified (1) as either continuous (loaded) or interrupted (unloaded); (2) as either the length or strain calibrated measurements. A total of four possible cases are summarized in the following. For simplicity, only one set of formulas are given for both differential and total strain methods, with the understanding that either strain increments or total strains can be used in those formulas.

Case A : Interrupted or unloaded with length measurements calibrated (using micrometers or any other length measuring gages). The plastic strain ratio for this case is given by

$$R = -\frac{\ln(w/w_0)}{\ln(w/w_0) + \ln(l/l_0)}, \tag{2.8}$$

where the initial reference gage length l_0 and width w_0 as well as the current deformed gage length l and width w of the sheet metal tensile specimen are measured by precision micrometers under completely unstressed conditions. If the initial dimensions are measured from the previous deformation step, the R-value is obtained by the differential strain method as given by Eq.(2.1). If the initial dimensions are measured from the undeformed state, then the R-value is computed using the total strain method given by Eq.(2.2).

The measurement error in R-values can be estimated from the errors in axial elongation and width measurements

$$\frac{\delta R}{R} = \eta^* \frac{1+R}{\ln(l/l_0)}, \tag{2.9}$$

where

$$\eta^* = \sqrt{\left(1+\frac{1}{R}\right)^2 \left[(\frac{\delta w}{w})^2 + (\frac{\delta w_0}{w_0})^2\right] + (\frac{\delta l}{l})^2 + (\frac{\delta l_0}{l_0})^2}. \tag{2.10}$$

Assuming all the length measurement errors are the same as δw, one then has

$$\frac{\delta R}{R} = \left[\frac{(1+R)\sqrt{2+4R+4R^2}}{R}\frac{1}{\ln(l/l_0)}\right]\frac{\delta w}{w}. \tag{2.11}$$

Consequently, the errors in the width measurements are likely dominant (four times of the axial ones if R=1). It is also evident that the error in R-values grows quickly as the true axial strain $\ln(l/l_0)$ approaches zero. That is, R-value becomes increasingly unreliable at the initial plastic yielding point.

Case B : Interrupted or unloaded with strain measurements calibrated (using clip gages or other strain measuring methods). The plastic strain ratio in this case is given by Eq.(2.2) and its error can be estimated from the errors in strain measurements

$$\frac{\delta R}{R} = (1+R)\frac{\delta\varepsilon_w^p}{\varepsilon_w^p} + R\frac{\delta\varepsilon_a^p}{\varepsilon_w^p}, \tag{2.12}$$

or (if $\delta\varepsilon_w^p = \delta\varepsilon_a^p$)

$$\frac{\delta R}{R} = (1+2R)\frac{\delta\varepsilon_w^p}{\varepsilon_w^p} = \frac{(1+2R)(1+R)}{R}\frac{\delta\varepsilon_a^p}{\varepsilon_a^p}. \tag{2.13}$$

The errors in strain measurements are amplified when computing the R-values (as $R > 0$ usually holds).

Case C : Continuous (loaded) with length measurements calibrated (using attached micrometers or any other length measuring gage). The plastic strain ratio is given by correcting for elastic strains first in the strain calculations, namely,

$$R = -\frac{\ln(w/w_0) + \nu\varepsilon_a^e}{\ln(w/w_0) + \ln(l/l_0) + (\nu-1)\varepsilon_a^e}, \tag{2.14}$$

where the total strains are assumed to be additive of elastic and plastic strains, ε_a^e is the elastic axial strain, and ν is the Poisson's ratio of the material. The difference between the R-values obtained via Eq.(2.8) and via Eq.(2.14) is only noticeable at very small strain levels of plastic deformation.

Case D : Continuous (loaded) with strain measurements calibrated (using clip gages or other strain measuring methods). After correcting for the elastic strains, the plastic strain

ratio is given by

$$R = -\frac{\varepsilon_w + \nu\varepsilon_a^e}{\varepsilon_a + \varepsilon_w + (\nu - 1)\varepsilon_a^e}, \tag{2.15}$$

where ε_a and ε_w are the total axial and width strains directly measured. In both cases C and D, the elastic axial strain ε_a^e is computed via the axial stress σ divided by the Young's modulus E of the material, and the axial (true) stress in terms of the applied axial load F and the current (deformed) cross-section area A of the tensile sample is usually obtained approximately as (A_0 is the initial cross-section area)

$$\sigma = \frac{F}{A} \approx \frac{F}{A_0}\frac{l}{l_0} = \frac{F}{A_0}\mathrm{e}^{\varepsilon_a}. \tag{2.16}$$

2.2.2 Additional Sources of Measurement Errors Using Digital Image Correlation

When the digital image based full-field strain mapping technique [56–58] is used, some other sources of errors in strain measurements may exist. One is the misalignment between the camera and the tensile specimen. If the misalignment is only in-plane (i.e., the image coordinate system is not completely aligned with the tensile axis and the transverse axis of the specimen), the errors in axial and width strains can be estimated from

$$\delta\varepsilon^{(\beta)} = \varepsilon_a^* - \varepsilon_a^p = (-\varepsilon_a^p + \varepsilon_w^p)\sin^2\beta, \quad \varepsilon_w^* - \varepsilon_w^p = (\varepsilon_a^p - \varepsilon_w^p)\sin^2\beta = -\delta\varepsilon^{(\beta)}, \tag{2.17}$$

where β is the misalignment angle between the image coordinates and the specimen axes. When the misalignment between the camera and the tensile specimen is out-of-plane, non-uniform magnifications will be induced in the digital images, resulting non-uniform scaling (virtual straining) over the image region of the tensile specimen. Proper calibration and pre-test adjustments of the experimental set-up are the best way to eliminate such misalignments.

Another significant source of errors may be due to the relative out-of-plane movements between the camera and the tensile specimen (even though the initial alignment between the camera and the specimen has been well adjusted). The specimen grips may cause some noticeable out-of-plane movements during the elastic loading and initial plastic yielding stages (typically accompanying a large increase of loads). If the error in strains due to the

out-of-plane movement is $\Delta\varepsilon$, then the two in-plane axial strain components are equally affected, namely,

$$R + \delta R = -\frac{\varepsilon_w + \Delta\varepsilon}{\varepsilon_a + \varepsilon_w + 2\Delta\varepsilon}, \quad \text{or} \quad \frac{\delta R}{R} = \frac{\varepsilon_w + \Delta\varepsilon}{\varepsilon_a + \varepsilon_w + 2\Delta\varepsilon}\frac{\varepsilon_a + \varepsilon_w}{\varepsilon_w} - 1. \tag{2.18}$$

The reduction in the sheet thickness during the subsequent plastic deformation can also induce some biaxial surface strain measurement errors by digital image correlation, namely

$$\Delta\varepsilon^{(h)} \approx \frac{h - h_0}{D}, \tag{2.19}$$

where h_0 and h are the initial and current thickness of the sheet metal specimen, and D is the camera-to-object distance (usually $D >> h_0$). The error is always negative (underestimating R-values). The error in the R-value due to plastic thinning can thus be expressed as (via some algebraic manipulation)

$$\frac{\delta R}{R} = \frac{h_0 - h}{D - 2h_0 + 2h}(2 + \frac{1}{R}). \tag{2.20}$$

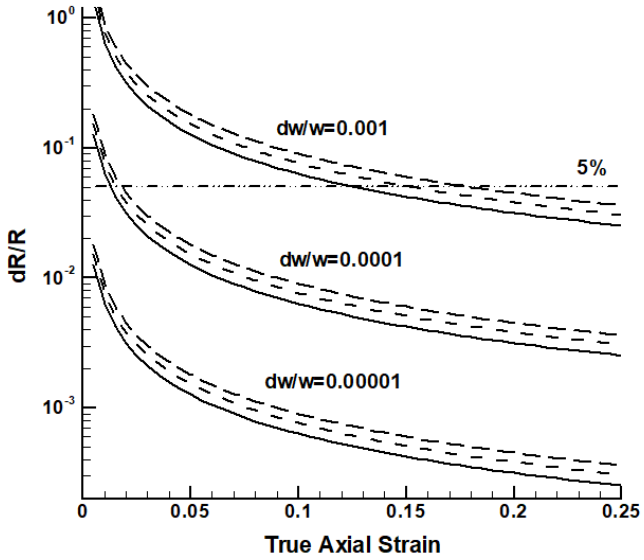

Figure 2.2: Errors in R-value measured in length.

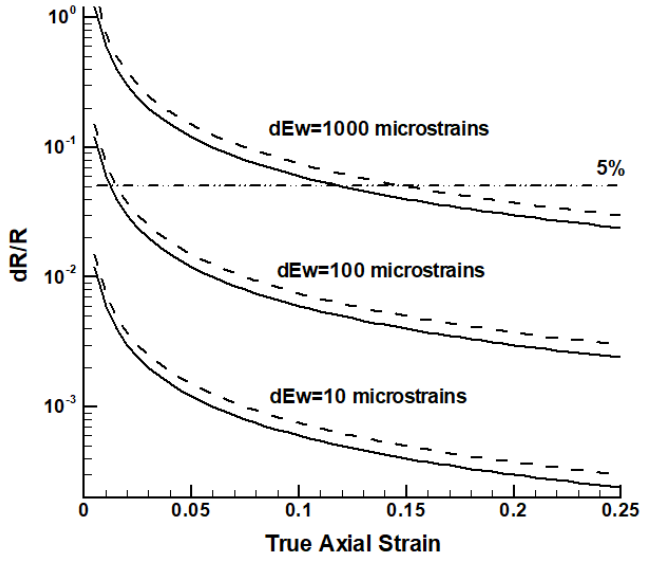

Figure 2.3: Errors in R-values measured in strain.

2.2.3 Numerical Examples of Errors in R-value Measurements

The errors in R-values are first examined numerically using several simulated data sets. For simplicity, the R-values are assumed to be constant with increasing true axial strains (ranging from 0.5% to 25%). For a given true axial strain and R-value, the true width strain (as needed in some of the equations used to compute the relative errors in R-values) are computed via

$$\varepsilon_w^p = -\frac{R}{1+R}\varepsilon_a^p. \tag{2.21}$$

Fig.2.2 shows errors in R-values in terms of the length measurement errors as given by Eq.(2.11). The three cases considered correspond to the errors in the width measurements of 0.127 μm, 1.27 μm and 12.7 μm respectively when the ASTM standard sheet metal tensile specimens with a width of 12.7 mm (0.5 inch) are used. The horizontal dashed-and-dotted line indicates the cut-off for a 5% error level in R-values. The results indicate that the error in the width measurements should be of ± 1.27 μm or less to ensure the errors in the R-values to be within 5%.

Fig.2.3 shows errors in R-values in terms of the strain measurement errors as given by

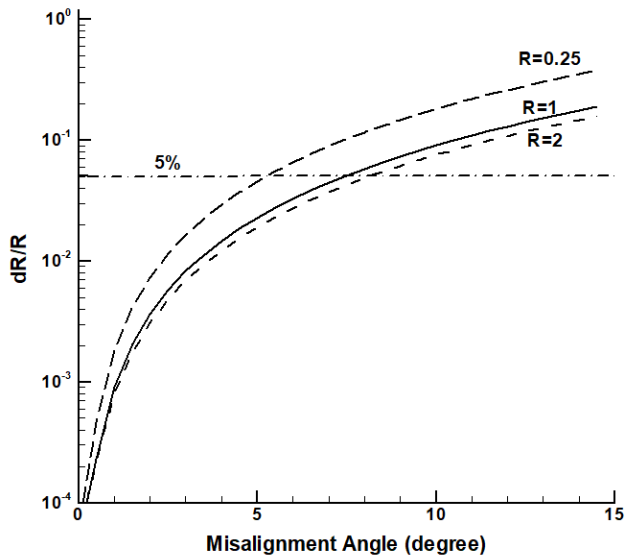

Figure 2.4: Errors in R-values measured based on misalignment between tensile specimen and digital image.

Eq.(2.13). Again, the horizontal dashed-and-dotted line indicates the cut-off for a 5% error in R-values. Clearly, if the strains can be measured within ±100 microstrains or less, the R-values can be determined within 5% even at small strain levels. According to Eq.(2.13), the minimum relative errors in R-values is 5.828 times of the relative strain errors when R=0.707. If the strain errors are of the order of 1,000 microstrains, the R-values may only be reliable for axial strains larger than 15%.

When the strains are measured based on the digital images, there may exist some misalignments between the image coordinates and the tensile specimen axes. The effect of such a misalignment on the errors in R-values is shown in Fig.2.4 (see Eq.(2.17)). If the misalignment angle is 5° or less, the error is about 5% or less for R=0.25 to 2.

The effect of elastic strains on the measured R-values as given by Eq.(2.16) is shown in Fig.2.5-Fig.2.7. Three materials are considered: copper (E=120 GPa, $\nu = 0.33$), aluminum (E=70 GPa, $\nu = 0.33$) and steel (E=210 GPa, $\nu = 0.33$). A linear strain hardening law is assumed for all three materials with the yield stress and the slope (plastic modulus) of 150 MPa and 650 MPa, respectively. It is apparent that if the strains are measured when

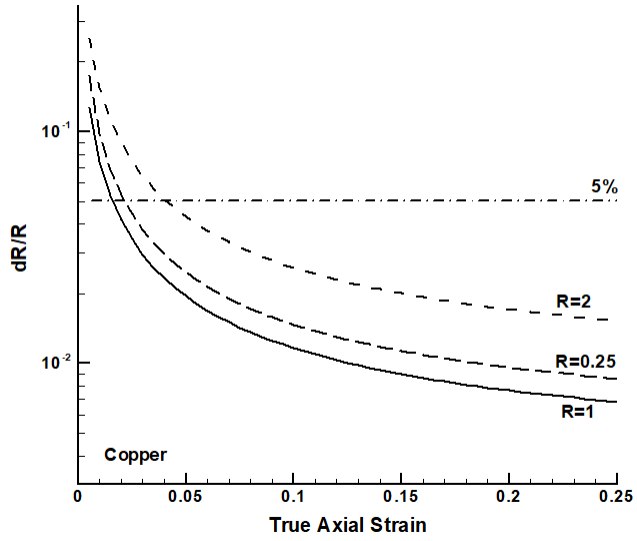

Figure 2.5: Errors in R-values for a copper sheet while not subtracting elastic strain from the total strain.

the tensile specimen is still loaded, then the correction for the elastic strain components is necessary to reduce the errors of R-values at small axial strain levels. The effect of elasticity is strongest for aluminum as it has the lowest Young's modulus.

Finally, some out-of-plane rigid body translations between the camera and the tensile specimen may occur when taking digital images during the deformation steps for strain measurements. Such translations will induce a virtual biaxial strain field superimposed on the actual plastic flow patterns, namely (assuming a pinhole projection and a parallel alignment between the camera and the tensile specimen),

$$\Delta\varepsilon_a^{(d)} = \Delta\varepsilon_w^{(d)} \approx \frac{d}{D-d}, \tag{2.22}$$

where d is the amount of out-of-plane translation of the tensile sample towards the camera, D is again the camera-to-object distance (usually $D >> d$). When the camera and the tensile specimen moves closer towards each other, both d and D are set positive; otherwise, they are set to be negative. Based on the above equation and Eq.(2.18), the effect of the out-of-plane translations on the errors in R-values can be obtained and the results are illustrated

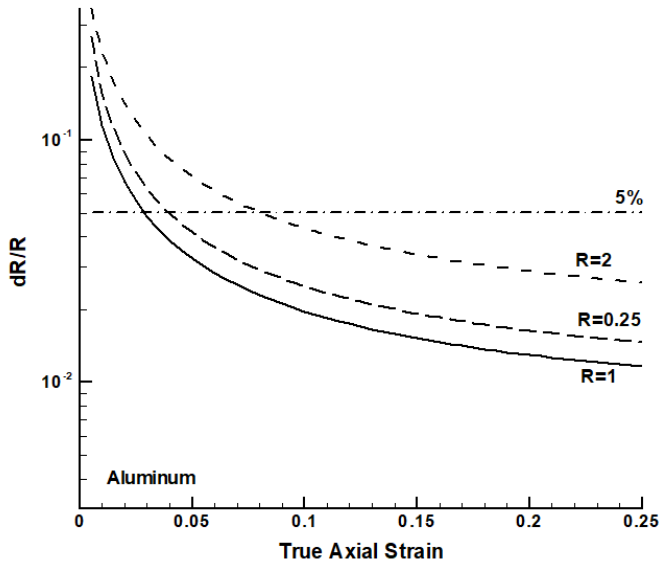

Figure 2.6: Errors in R-values for an aluminum sheet while not subtracting elastic strain from the total strain.

in Fig.2.8 for R=0.25, 1, and 2. If the out-of-plane translation d/D is about ±0.0001 or less, the induced errors in R-values are negligible. However, when the out-of-plane translations are significant (say, d/D=±0.0025 or larger), correction of the virtual strains is necessary to minimize the errors in R-values.

Using the copper sheet metal samples as an example and assuming their R-values in the rolling direction is a constant of 0.6 [55], the errors in measured R-values as a function of the axial strain are shown in Fig.2.9 and Fig.2.10. Different levels of errors in the width measurements by a micrometer and strain measurements by digital image correlation are assumed. For the tests on both the compact and standard tensile samples, the lower bound error on the dimension measurements is about 0.00025" or 6 μm and the upper bound can be as high as 0.00125" or 16 μm or higher (surface roughening and edge wrinkling effects due to plastic deformation). The intrinsic errors (due to image noises) in the average strains by digital image correlation are 100 microstrains or less but the extrinsic errors (due to deformation and motions) can be as high as 500-1000 microstrains or higher. When measuring R-values at small strain levels of 1-5%, the errors in strains should be controlled

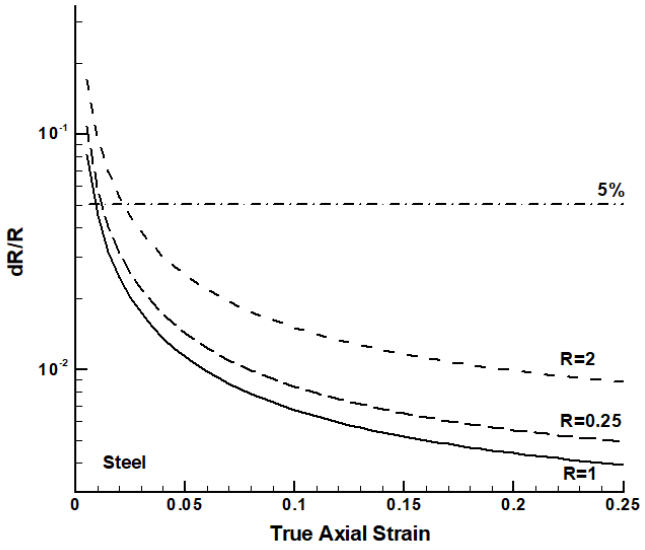

Figure 2.7: Errors in R-values for a steel sheet while not subtracting elastic strain from the total strain.

to be within 20 microstrains, then the errors in R-values can be limited to 1-2%.

The precision and accuracy of plastic strain ratio values are easily affected by the errors in the dimension or strain measurements of plastically deformed sheet metals. Existing manual methods measuring dimension changes by micrometers are not suitable for either small (5% or less) or very large (after necking) strain levels. The digital image based strain measurement technique in principle can be used instead. However, some efforts are required to minimize strain errors due to optical misalignments. By using the proper experimental measurement and data processing procedure to be presented in this study, the plastic strain ratio R may be determined with an error of 2.5% or less over a wide range of strain levels.

2.3 Uniaxial Tensile Testing of Flat Sheet Coupons

2.3.1 Sheet Metal Material and Test Coupon Preparation

Each test coupon was cut from an aluminum alloy sheet metal AA6111-T4 of 1.2mm in thickness on a water-jet machine. Multiple tensile test coupons with five different orientations to the rolling direction of the sheet metal were obtained. A digital image of an as-machined AA6111-T4 sheet test coupon is shown in Fig.2.11 along the machining schematic of showing

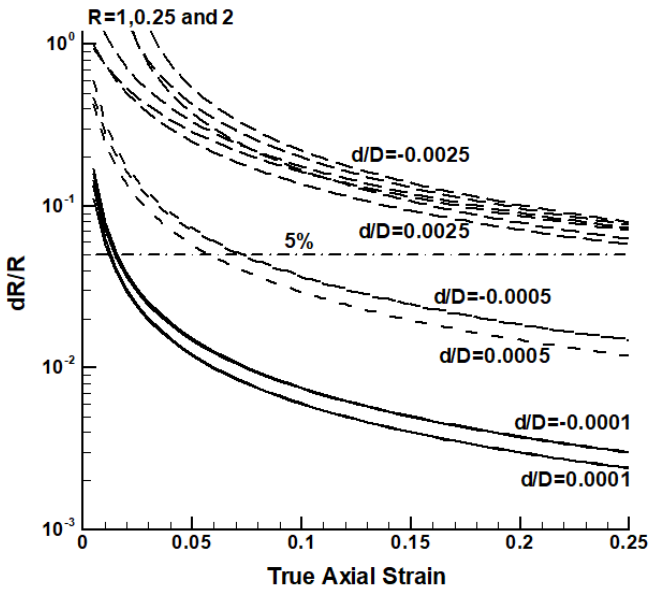

Figure 2.8: Errors in R-values due to the out-of-plane translations between the camera and the tensile specimen.

orientations of the test coupons. Such an aluminum sheet metal has been used in some prior laser welding and anisotropic plasticity modeling studies [59, 60].

2.3.2 Uniaxial Tension Testing

The uniaxial tensile experiments using compact test coupons were carried out in the displacement control mode on an Instron 5967 universal materials test machine with a 30 kN static load cell. A constant cross-head speed of 0.025 mm/min was used in all experiments. Three sets of test samples with five different loading angles were tested, see Fig.2.12. They consist of samples subjected to the tensile loading along 0-degree or rolling direction (RD), 22.5-degree, 45-degree or diagonal direction (DD), 67.5-degree and 90-degree or transverse direction (TD) from the RD of the sheet metal respectively. Each test coupon was held at both ends by a pair of wedge grips with flat but serrated faces and was tensile loaded to final fracture while the upper cross-head displacement and load cell reading were recorded continuously at 10 Hz data acquisition rate. During each test, a monochrome digital CCD camera from Point Grey Research Inc. (www.ptgrey.com) with a telecentric zoom lens was

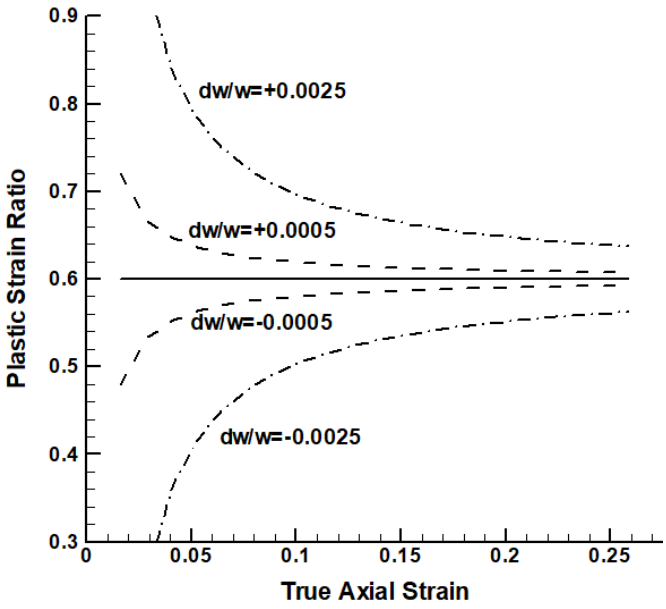

Figure 2.9: Upper and lower bounds on the errors of R-values determined by the width and length of the deformed sheet specimens.

used to image one surface of the gage zone of the flat test sample at 0.5 fps. A total of about 700 or more images were acquired for each test. Each 8-bit grayscale image has a size of 1920-by-1200 pixels with a typical pixel resolution around 28 microns/pixel.

The camera for acquiring digital images should be properly aligned with the tensile specimen. The tensile loading direction of the specimen should be parallel with the horizontal axis of the images. The quality of the alignment and the errors in strain measurements by digital image correlation can be assessed following the procedure described in [56]. Strains errors of 100 microstrains or less due to image noises and small rigid body motions can be easily achieved. For small strain applications, the strain errors should be reduced to 10-20 microstrains or less.

If it is desirable to measure the strain errors due to relative out-of-plane motions between the camera and the specimen during the tensile test, a small flat reference object (such as a microscope glass slide with sprayed paints) can be mounted on top of the tensile specimen by a rubber band or soft adhesive. The reference object will be placed inside the field-of-view of

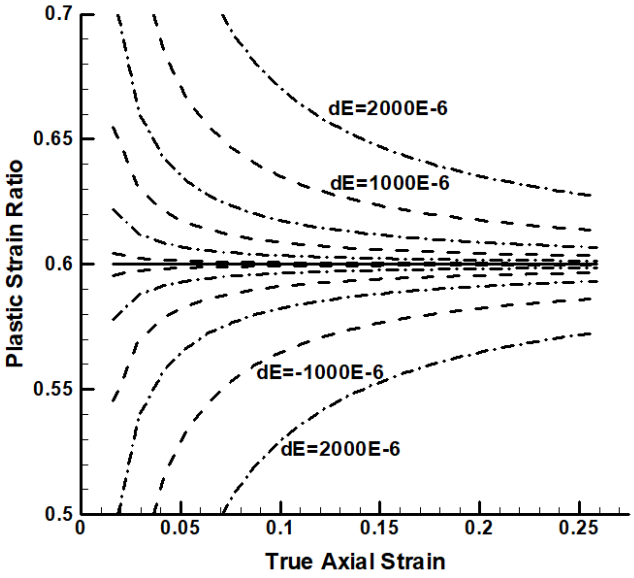

Figure 2.10: Upper and lower bounds on the errors of R-values determined by the axial and width strains of the deformed sheet specimens. The errors in strains are assumed to be 20,100,250,500,1000 and 2500 microstrains.

the digital images (without blocking the central section of the specimen gage section). The reference object will remain undeformed and the strains detected by correlation of its images can be used as a measure of the strain errors due to rigid body motions of the specimen in the test.

A series of digital images are acquired during the tensile test. The digital images for plastic strain ratio measurements shall be in general taken at least 1%-2% strain increment apart. To improve the image quality, the crosshead of the loading machine may be stopped while acquiring the digital images (but the specimen can still be loaded). One can also completely unload the specimen before taking the images.

As only one end of the specimen grips moves in conventional material testing machines (such as those manufactured by Instron or MTS), some significant in-plane translations along the tensile loading direction will occur as the sheet specimen plastically deforms. The initial field-of-view of the images should be set to take such translations into account to ensure that the central section of the tensile specimen always stays in the center part of the images.

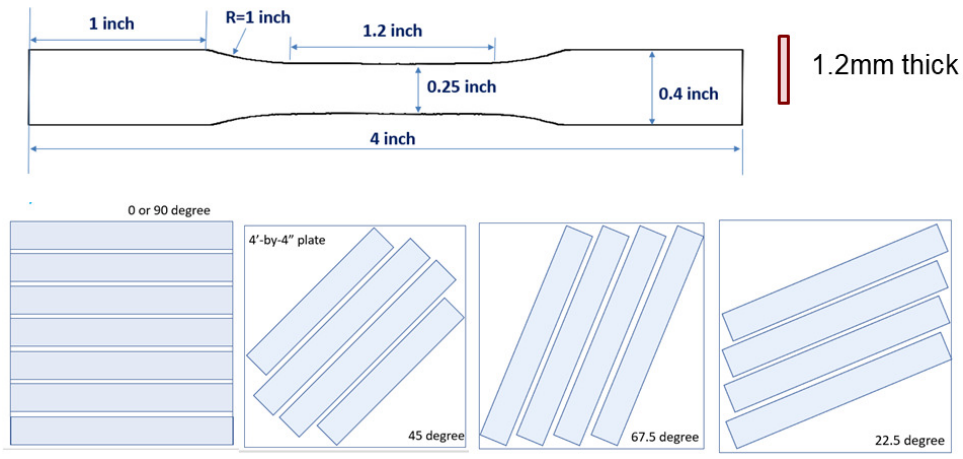

Figure 2.11: Geometry and orientation of tension test coupon.

This is not a problem for specially built tensile testing apparatus with symmetrical loading frames (the center of the field of view of the specimen hardly moves in such cases).

2.3.3 Strain Measurements by Digital Image Correlation Analysis

The digital image set acquired during the tensile test can be processed using a digital image correlation (DIC) program implemented in MATLAB based on the well-known Lucas-Kanade inverse compositional algorithm [61–63] for computation of the average in-plane strains and then the R-values. Typically, large subset sizes and gage sizes (80 and up to 120 pixels) should be used to reduce the errors in the average strain measurements. To minimize the effects such as machining errors and plastic wrinkling at the specimen edges, the processed region of the interest of the images should not include the boundary regions of the specimen in image (including the processing option for average strain calculations as well). By inspecting the strain maps obtained from digital image correlation, one needs also to ensure that no gross inhomogeneous deformation exist with the region of interest (especially at both ends of the specimen gage section that are close to the tapered grip sections). On the other hand, as the plastic strain ratio is a macroscopic measure of plastic flow anisotropy, the region of interest used to compute the average strains should be as large as possible.

The R-values should be computed by using either the incremental strain method (by

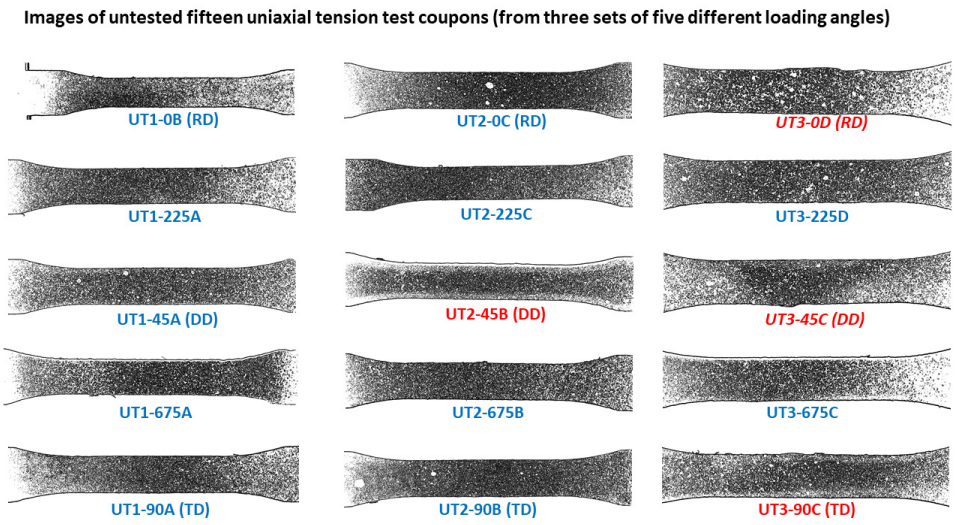

Figure 2.12: A summary of 15 tension test coupons.

directly computing the true strain increments between images) or the differential strain method (by numerically computing the derivatives of the total true width strain with respect to the total true axial strain). If the errors due to rigid body motions during the test are measured, both width and axial strains should be corrected first. If there is a significant degree of in-plane misalignment between the image coordinates and the tensile specimen orientation, a strain transformation may be needed to correct the strains. Alternatively, one can simply output the principal true strains from the MATLAB digital image correlation program and used them as the corrected width and axial strain data for computing R-values. The errors in R-values can be easily achieved to within 5% by the procedure outlined here for both small and large deformation applications. With extra precautions, measurements of out-of-plane motions, and more advanced camera calibrations, limiting the errors in R-values to 1% or less is achievable by digital image strain mapping technique.

2.4 Experimental Results

As described in previous section, a typical tensile test was carried out in the displacement control mode on an Instron 5967 universal materials test machine with a 30 kN static load cell, see Fig.2.13(a). Unlike the conventional tension test protocol, up to 11 periodic unloading

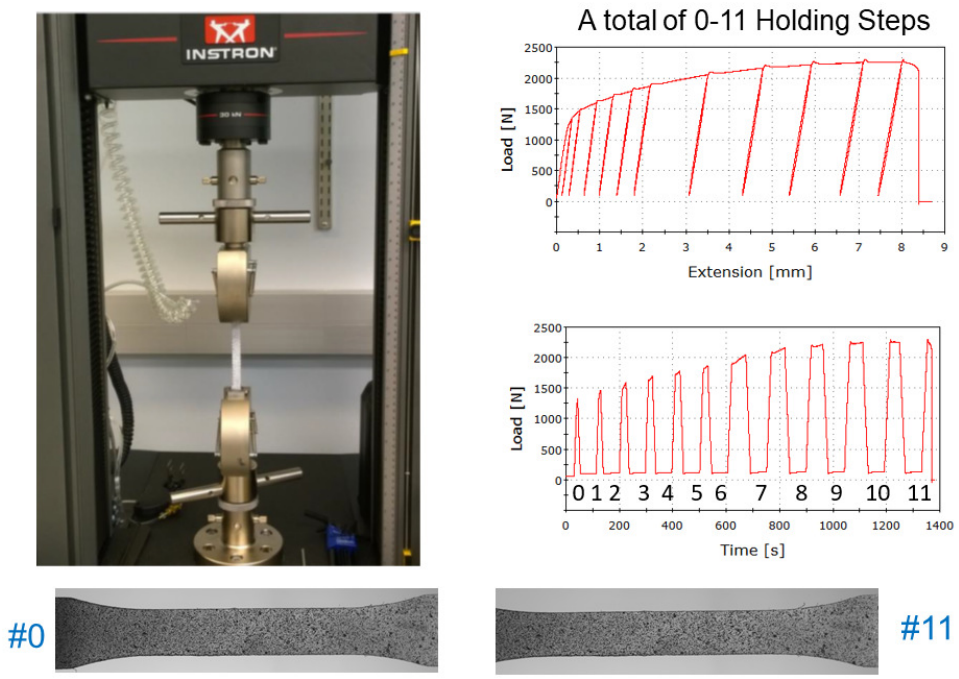

Figure 2.13: Test setup, loading history and image frame: (a) Instron material testing machined used in the study; (b) the axial tensile load versus displacement or extension curve and the time history of the axial tensile load of a typical test (Sample #UT1ST0B); (c) the frame-averaged image frame at #0 and #11 holding steps during tension testing of the sample.

and reloading steps were imposed during the tensile test, see Fig.2.13(b). At each unloaded state with only a small tensile load of about 50 N (an engineering stress of about 7 MPa or an engineering strain of about 100 microstrains), a holding time of 60 seconds was used to acquire abut 30 image frames of the stationary tensile sample in each test. Those image frames were then averaged to obtain a total of 12 images labeled #0 to #11 with reduced image noises. Representative of image frame #0 (undeformed prior to any tensile plastic deformation) and #11 (deformed at the last unloaded state prior to necking and final fracture of the test coupon) are shown in Fig.2.13(c).

The nominal axial tensile true stress versus true strain curve of the aluminum alloy sheet AA6111-T4 from the tensile test sample #UT1ST0B is shown in Fig.2.14. The nominal axial true strain and true stress was obtained by using the cross-head displacement, axial force from the load cell, the 1-inch initial gage length of the tension coupon and the usual assumption

of plastic incompressibility. A custom-made video extensometer program based on digital image correlation was used to analyze the 12 frame-averaged images #0 to #11 to obtain the axial plastic strains. As illustrated in Fig.2.14, two vertical rectangular boxes in images #0 and #11 were the regions of interest (600-by-230 pixels) used in the video extensometer measurement. Table 2.1 lists total plastic axial strains at each of the 11 holding steps with negligible tensile loading.

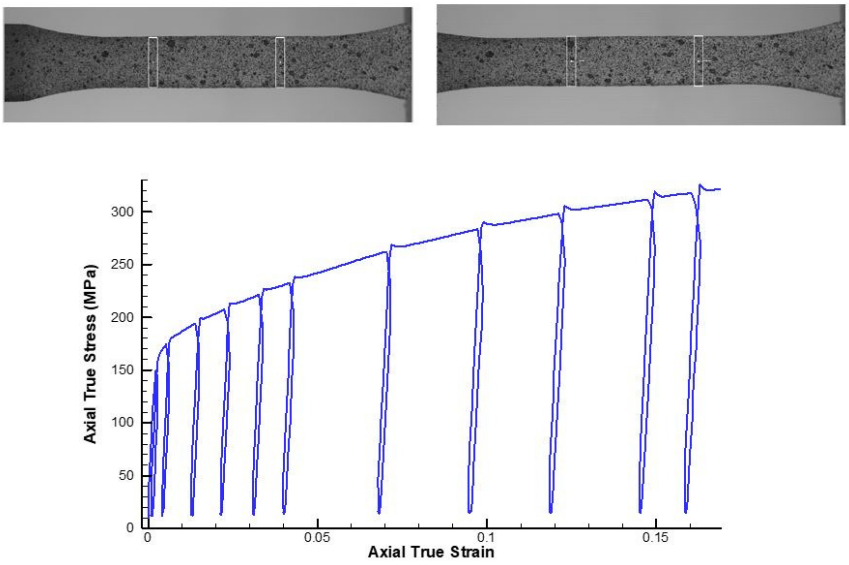

Figure 2.14: The nominal axial tensile true stress versus true strain curve of the aluminum alloy sheet from the tensile test sample #UT1ST0B.

Fig.2.15 - Fig.2.17 and Table 2.2 - Table 2.4 summarize the measurement results on R-values of AA6111-T4 sheet from the total of 15 tension test coupons in this study. A gage section of 600-by-230 pixels were used to compute the average strains of the tensile test coupon by digital image correlations. Two different methods of computing the plastic strain ratios were used: the differential strain method of Eq.(2.1) and the cumulative strain method of Eq.(2.2) respectively. To reduce the detrimental effect of noisy strain data upon

Table 2.1: Total axial plastic strain at the 11 unloaded steps of the test

No.	Axial Plastic Strain
1	0.00101
2	0.00425
3	0.01285
4	0.02140
5	0.03105
6	0.04011
7	0.06816
8	0.09486
9	0.11884
10	0.14517
11	0.15895

the numerical differentiation, the finite difference was used instead for Eq.(2.1), that is

$$R(\varepsilon_a^p) = \frac{\mathrm{d}\varepsilon_w^p}{\mathrm{d}\varepsilon_t^p} \approx -\frac{\Delta\varepsilon_w^p}{\Delta\varepsilon_a^p + \Delta\varepsilon_w^p}. \tag{2.23}$$

Table 2.2: Uniaxial tension plastic strain ratios obtained from the first set of test coupons

$\theta(^\circ)$	0	22.5	45	67.5	90
$\bar{R}_\theta$	0.89	0.65	0.40	0.45	0.67
R_θ	0.87	0.67	0.42	0.48	0.67

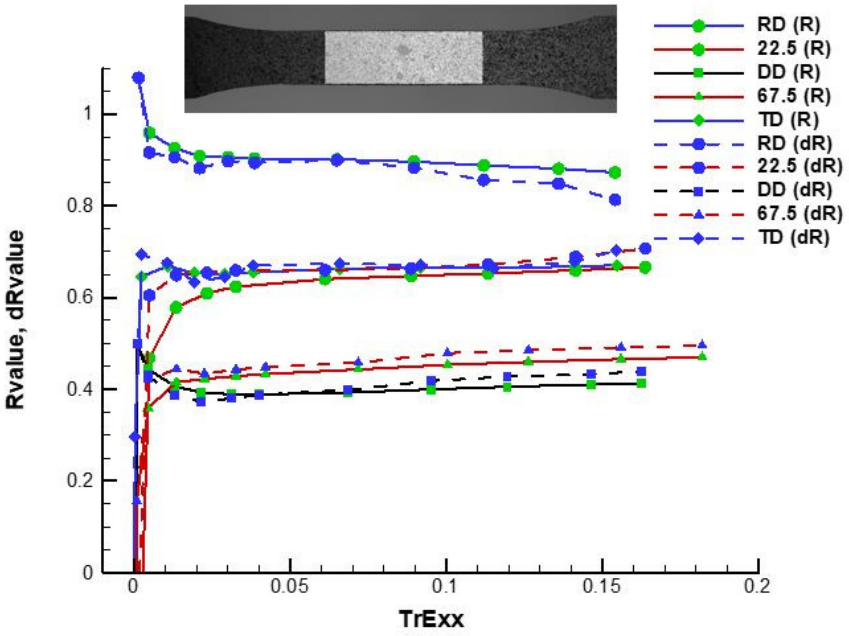

Figure 2.15: Uniaxial tension plastic strain ratios obtained from the first set of five test coupons at five different orientations.

Table 2.3: Uniaxial tension plastic strain ratios obtained from the second set of test coupons

$\theta(^{\circ})$	0	22.5	45	67.5	90
$\bar{R}_\theta$	0.97	0.66	0.38	0.47	0.67
R_θ	0.95	0.69	0.38	0.49	0.66

2.5 Discussions and Conclusions

2.5.1 On the Evolution of R-value with Plastic Strain

In order to better visualize the possible variations of R-values with increasing axial plastic strain, the experimental results based on two calculation methods for six on-axis tension test coupons (i.e., the loading angle = 0 or 90 degrees) are further compared side-by-side in Fig.2.18. For the three 90° or TD tension test coupons, their R-values are rather consistent with each other and virtually remain constant beyond the axial plastic strain of 1-2%. The R-

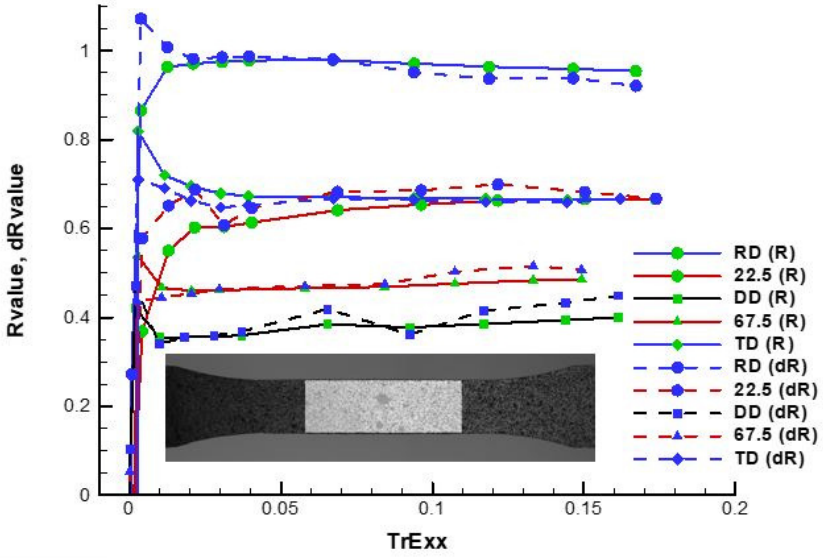

Figure 2.16: Uniaxial tension plastic strain ratios obtained from the second set of five test coupons at five different orientations.

Table 2.4: Uniaxial tension plastic strain ratios obtained from the third set of test coupons

$\theta(^{\circ})$	0	22.5	45	67.5	90
$\bar{R}_\theta$	0.92	0.65	0.39	0.47	0.65
R_θ	0.91	0.65	0.41	0.48	0.65

values from the strain difference method start to deviate at the last unloaded step. A further inspection of the whole-field increment strain map obtained by digital image correlation indicates the occurrence of diffuse necking in the tension coupon. As shown in Table 2.2 - Table 2.4, the average R-values at $\varepsilon_a^p = 0.1$ are $\bar{R}_{90} = 0.663$ and $R_{90} = 0.660$ with a very small standard deviation of 0.012 or less.

On the other hand, there are some noticeable sample-to-sample variations in R-values from the three 0° or RD tension test coupons. As shown in Table 2.2 - Table 2.4, the average

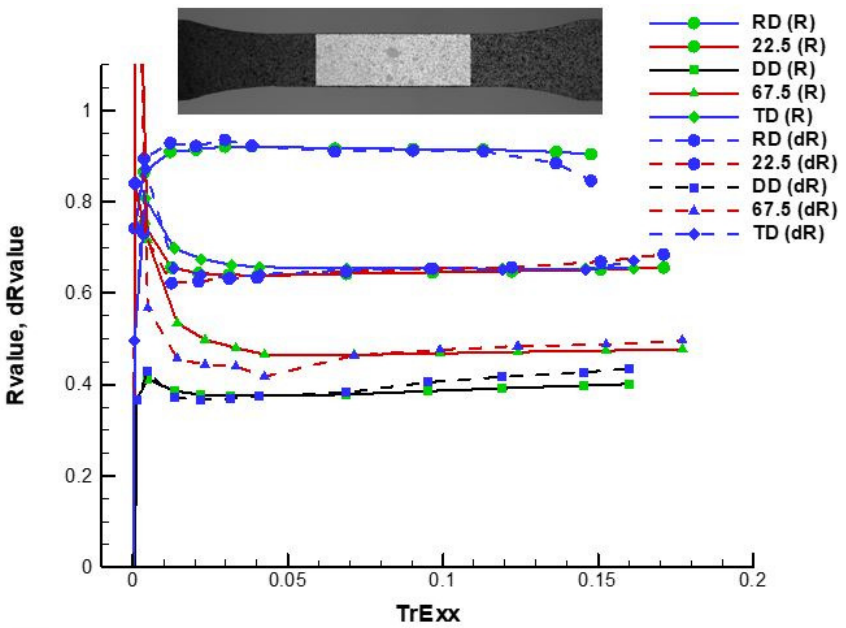

Figure 2.17: Uniaxial tension plastic strain ratios obtained from the third set of five test coupons at five different orientations.

R-values at $\varepsilon_a^p = 0.1$ are $\bar{R}_0 = 0.927$ and $R_0 = 0.910$ with a much larger standard deviation of 0.040. A closer examination of the geometry of those three tested tension coupons under a microscope founds that the sample edges are clearly irregular due to improper water-jet cutting of the coupon from the as-received sheet blank. This may have contribute to such a larger scattering in sample-to-sample R-values. Nevertheless, each R-value still tends to be constant beyond the axial plastic strain of 2%.

2.5.2 Possible Measurement Errors and Their Effects on Measured R-values

As discussed in details in Section 2.2 that there are many potential factors affecting the measurement accuracy and precision of R-values. Because only the images of unloaded tension coupons were used in digital image correlation based strain measurements, any uncertainty about subtracting elastic strains from total strains has thus been minimized in this study for computing R-values. The optical effect of any out-of-plane motion, lens distortion and camera misalignment may play a role in creating the initial large changes in R-values with increasing axial plastic strains.

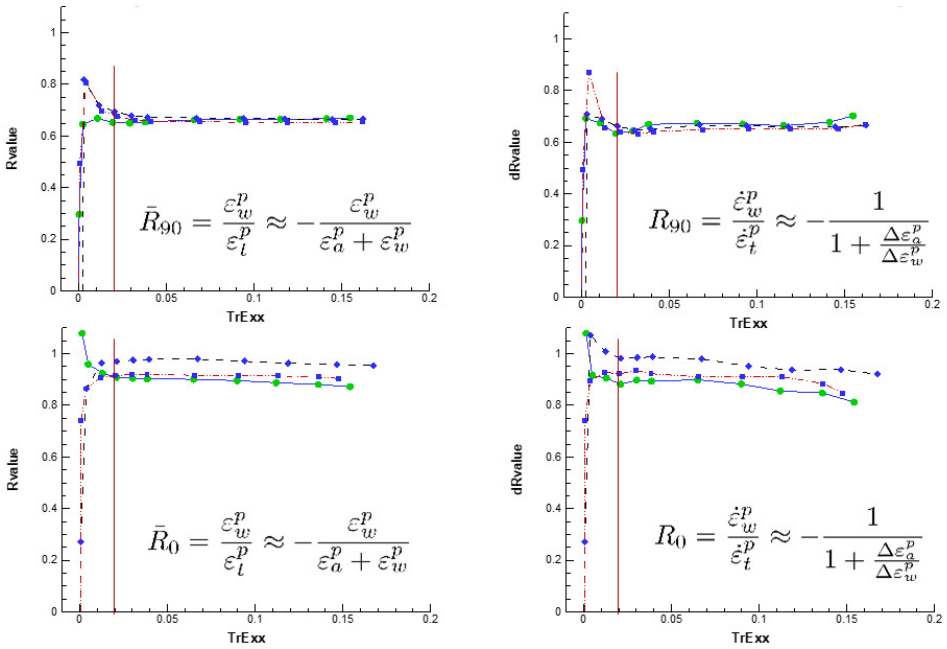

Figure 2.18: Comparison between the experimental results based on two calculation methods for six on-axis tension test coupons.

One additional factor may be due to the non-homogeneity of deformation field (and the initial state of the aluminum sheet) at small strains. Incremental axial strain maps were obtained from digital image correlation analysis of the first five frame-averaged images of the unloaded tension test coupon #UT1-90A, and the resulting contour plots are shown in Fig.2.19. Clearly, the strain increments are non-uniform prior to the load steps #4 ($\varepsilon_a^p = 1.93\%$) and #5 ($\varepsilon_a^p = 2.91\%$), indicating the uniform strain and thus uniform stress states for an ideal uniaxial tension loading condition of a homogeneous gage section may have not existed at all in small strains.

2.5.3 Concluding Remarks

Anisotropic plastic flow of a thin sheet metal is often characterized by plastic strain ratios determined in a series of uniaxial tensile tests with angles between the tensile loading axis and the rolling direction of the sheet metal ranging from 0 to 90 degrees. Existing experimental methods used to measure the plastic strain ratios in common practice are briefly reviewed and a new approach using a digital image based full-field strain mapping technique and associated

camera calibration is introduced. Potential sources of errors in both old and new methods are discussed in great details with the emphasis on achieving best precision and accuracy in plastic strain ratio values. Some theoretical results relating the anisotropic plasticity models to the plastic strain ratios are also included. Within the measurement uncertainties and sample-to-sample variations, the experimental results on AA6111-T4 obtained in this study show that the unaxial tension plastic strain ratios are virtually constant at axial plastic strain of 2% and beyond. It is thus concluded at least for this sheet metal that a general anisotropic hardening model may not be needed to be included in anisotropic plasticity analysis.

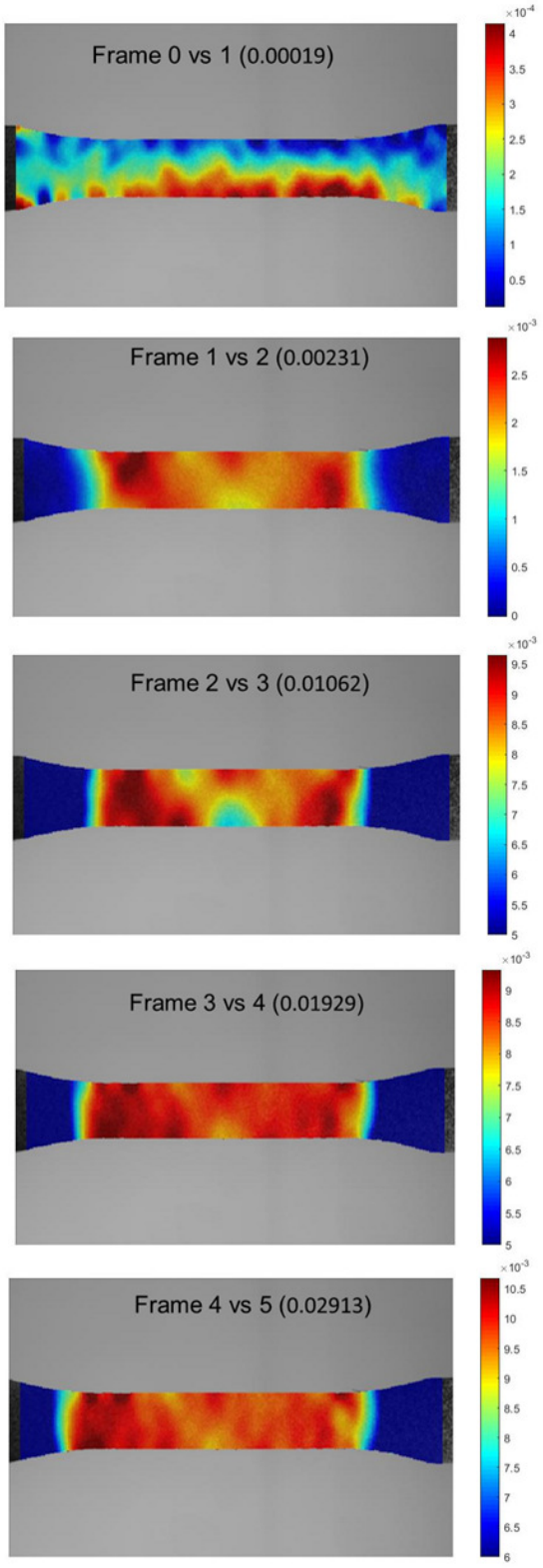

Figure 2.19: Incremental axial strain maps of the first five frame-averaged images of the unloaded tension test coupon #UT1-90A.

Chapter 3

A COMPARATIVE EVALUATION OF TWO FORMULATIONS OF A FOURTH-ORDER ORTHOTROPIC YIELD FUNCTION IN PLANE STRESS

3.1 Introduction

In mathematical modeling of yielding and associated plastic flow of a sheet metal in plane stress, a suitable scalar-valued norm function $f(\sigma_x, \sigma_y, \tau_{xy})$ of the applied Cauchy stress expressed in orthotropic in-plane sheet metal symmetry axes xy as $\boldsymbol{\sigma} = (\sigma_x, \sigma_y, \tau_{xy})$ plays an essential role as the so-called yield stress function in three aspects [20, 34, 36]: it is used (1) to set the yield condition $f(\boldsymbol{\sigma}) = \sigma_f$ (where σ_f is the current yield strength of the sheet metal), (2) to compute the plastic strain increments using an associated flow rule $\dot{\boldsymbol{\varepsilon}}^p \propto \partial f / \partial \boldsymbol{\sigma}$, and (3) to define an equivalent stress $\bar{\sigma} = f(\boldsymbol{\sigma})$ and its plastic work conjugate equivalent plastic strain increment $\dot{\bar{\varepsilon}}^p$ via $\bar{\sigma}\dot{\bar{\varepsilon}}^p = \boldsymbol{\sigma} : \dot{\boldsymbol{\varepsilon}}^p \geq 0$. Most often, the yield strength of the sheet metal is taken as a monotonically increasing function of the equivalent plastic strain to account for strain hardening, $\sigma_f = \sigma_f(\bar{\varepsilon}^p)$ with $\sigma_f'(\bar{\varepsilon}^p) > 0$.

In principle, any scalar-valued function $f(\sigma_x, \sigma_y, \tau_{xy})$ of the Cartesian stress components of the stress tensor can be used as the yield function for the sheet metal as long as it is *positive* and *convex* and obeys the orthotropic material symmetry, i.e., $f(\sigma_x, \sigma_y, \tau_{xy}) = f(\sigma_x, \sigma_y, -\tau_{xy})$ [35, 64, 65]. There are two commonly used formulations or approaches in constructing such a yield function. The first formulation is to use a polynomial function of second or higher order and its positivity and convexity has to be further certified mathematically upon the calibration of its polynomial coefficients [34–36, 65–67]. The second formulation is to use a positive and convex non-quadratic isotropic function of the so-called linearly transformed stresses and its positivity and convexity is automatically ensured upon the calibration of its real-valued material constants [20, 40, 68]. When the stress exponent M is set to an even order in the second formulation, the resulting yield function is shown to be in general a

reduced form of a *positive* and *convex* polynomial function of the same order [68,69].

In this study, we consider the fourth-order yield functions developed by these two formulations, namely, Gotoh's fourth-order polynomial yield function and Yld2000-2d yield function with a stress exponent M=4. Historically, the development of Gotoh's 1977 quartic polynomial yield function is a natural continuation and extension of Hill's 1948 quadratic polynomial yield function. It is one of the earliest and capable *non-quadratic* yield functions for advanced sheet metal plasticity modeling [36,60,70–74]. As the total number of eight independent material constants in the fourth-order Yld2000-2d is one less than the total number of nine independent polynomial coefficients in Gotoh's yield function, a detailed comparative evaluation about the similarities and differences of these two fourth-order yield functions is warranted.

In the following, fourth-order yield functions by these two formulations are summarized in Section 3.2 along with the nonlinear relationship between polynomial coefficients in Gotoh's yield function and material constants in Yld2000-2d. In Section 3.3, parameter identification is detailed for these two versions of the fourth-order yield function when the same three, five, seven or eight independent experimental inputs are used. Examples of calibrated yield functions for modeling four representative sheet metals are presented and compared in Section 3.4. Discussion and conclusions of the study are given in Section 3.5, including comments about some recent results as reported by Uppaluri and Helm [74] on the convex fourth-order yield function.

3.2 Fourth-order Yield Functions in Plane Stress

3.2.1 Gotoh's 1977 Yield Function

The complete fourth-order homogeneous polynomial as a plane stress yield function has the following form according to Gotoh [36]

$$\begin{aligned}\Phi_g(\sigma_x,\sigma_y,\tau_{xy}) = f^4(\boldsymbol{\sigma}) = {} & A_1\sigma_x^4 + A_2\sigma_x^3\sigma_y + A_3\sigma_x^2\sigma_y^2 + A_4\sigma_x\sigma_y^3 + A_5\sigma_y^4 \\ & + A_6\sigma_x^2\tau_{xy}^2 + A_7\sigma_x\sigma_y\tau_{xy}^2 + A_8\sigma_y^2\tau_{xy}^2 + A_9\tau_{xy}^4,\end{aligned} \tag{3.1}$$

where $(A_1, A_2, ..., A_9)$ are nine polynomial coefficients (material constants). To facilitate its parameter identification from independent experimental inputs and to study various cases

of reduced plastic anisotropy, reformulation in terms of intrinsic variables (principal stresses σ_1 and σ_2 and loading angle θ) is preferred [65, 75, 76]

$$\phi_g(\sigma_1,\sigma_2,\theta) = F(\theta)\sigma_1^4 + G(\theta)\sigma_1^3\sigma_2 + H(\theta)\sigma_1^2\sigma_2^2 + G(\theta+\frac{\pi}{2})\sigma_1\sigma_2^3 + F(\theta+\frac{\pi}{2})\sigma_2^4, \tag{3.2}$$

where $F(\theta), G(\theta)$ and $H(\theta)$ are in the Fourier cosine series form

$$\begin{aligned} F(\theta) &= F_0 + F_1\cos2\theta + F_2\cos4\theta + F_3\cos6\theta + F_4\cos8\theta, \\ G(\theta) &= G_0 + G_1\cos2\theta + G_2\cos4\theta - 2F_3\cos6\theta - 4F_4\cos8\theta, \\ H(\theta) &= H_0 - 2(F_2+G_2)\cos4\theta + 6F_4\cos8\theta, \end{aligned} \tag{3.3}$$

and the nine unique Fourier coefficients $(F_0, F_1, F_2, F_3, F_4, G_0, G_1, G_2, H_0)$ are given by Tong [72, 76] in terms of linear relationships of the nine polynomial coefficients $(A_1, A_2, ..., A_9)$ in $\Phi_g(\sigma_x, \sigma_y, \tau_{xy})$ of Eq.(3.1).

3.2.2 The Fourth-order Yld2000-2d

As discussed by Barlat et al. [40], the original Yld2000-2d and several of its variants are equivalent with a total of up to eight independent material constants. Two particularly popular forms of fourth-order Yld2000-2d yield function are considered: the original form by Barlat's group [20, 40] and one of its compact variants by Aretz [41]. The original Yld2000-2d has the following form in terms of its eight material constants $(\alpha_1, \alpha_2, ..., \alpha_8)$

$$\begin{aligned} 2\Phi_{2k}^{(\alpha)}(\boldsymbol{\sigma}) = 2f^4(\boldsymbol{\sigma}) = \{&(\frac{2\alpha_3-2\alpha_4+4\alpha_5-\alpha_6}{6})\sigma_x - (\frac{\alpha_3-4\alpha_4+2\alpha_5-2\alpha_6}{6})\sigma_y \\ &+ \sqrt{[(\frac{2\alpha_3-2\alpha_4-4\alpha_5+\alpha_6}{6})\sigma_x - (\frac{\alpha_3-4\alpha_4-2\alpha_5+2\alpha_6}{6})\sigma_y]^2 + (\alpha_8\tau_{xy})^2}\ \}^4 \\ &+ \{(\frac{2\alpha_3-2\alpha_4+4\alpha_5-\alpha_6}{6})\sigma_x - (\frac{\alpha_3-4\alpha_4+2\alpha_5-2\alpha_6}{6})\sigma_y \\ &- \sqrt{[(\frac{2\alpha_3-2\alpha_4-4\alpha_5+\alpha_6}{6})\sigma_x - (\frac{\alpha_3-4\alpha_4-2\alpha_5+2\alpha_6}{6})\sigma_y]^2 + (\alpha_8\tau_{xy})^2}\ \}^4 \\ &+ \{2\sqrt{[(\frac{2\alpha_1+\alpha_2}{6})\sigma_x - (\frac{\alpha_1+2\alpha_2}{6})\sigma_y]^2 + (\alpha_7\tau_{xy})^2}\ \}^4. \end{aligned} \tag{3.4}$$

One of its variants is given by Aretz [41] as

$$
\begin{aligned}
2\Phi_{2k}^{(\beta)}(\boldsymbol{\sigma}) = 2f^4(\boldsymbol{\sigma}) = &\{\frac{\beta_8\sigma_x+\beta_1\sigma_y}{2}+\sqrt{(\frac{\beta_2\sigma_x-\beta_3\sigma_y}{2})^2+(\beta_4\tau_{xy})^2}\ \}^4 \\
&+\{\frac{\beta_8\sigma_x+\beta_1\sigma_y}{2}-\sqrt{(\frac{\beta_2\sigma_x-\beta_3\sigma_y}{2})^2+(\beta_4\tau_{xy})^2}\ \}^4 \\
&+\{2\sqrt{(\frac{\beta_5\sigma_x-\beta_6\sigma_y}{2})^2+(\beta_7\tau_{xy})^2}\ \}^4,
\end{aligned}
\tag{3.5}
$$

where $(\beta_1, \beta_2, .., \beta_8)$ are its eight material constants and they are shown by Barlat et al. [40] to be related to $(\alpha_1, \alpha_2, .., \alpha_8)$ as

$$
\begin{aligned}
&\beta_1 = \frac{-\alpha_3+4\alpha_4-2\alpha_5+2\alpha_6}{3}, \quad \beta_2 = \frac{-2\alpha_3+2\alpha_4+4\alpha_5-\alpha_6}{3}, \\
&\beta_3 = \frac{-\alpha_3+4\alpha_4+2\alpha_5-2\alpha_6}{3}, \quad \beta_8 = \frac{2\alpha_3-2\alpha_4+4\alpha_5-\alpha_6}{3}, \\
&\beta_5 = \frac{2\alpha_1+\alpha_2}{3}, \quad \beta_6 = \frac{2\alpha_2+\alpha_1}{3}, \quad \beta_4 = \alpha_8, \quad \beta_7 = \alpha_7.
\end{aligned}
\tag{3.6}
$$

Both fourth-order yield functions $2\Phi_{2k}^{(\alpha)}(\boldsymbol{\sigma})$ and $2\Phi_{2k}^{(\beta)}(\boldsymbol{\sigma})$ can be expanded out into the same polynomial of Eq.(3.1) with their nine coefficients being given as (here $\tilde{A}$ and $\bar{A}$ are used to indicate that they are computed from functions of $(\alpha_1, \alpha_2, .., \alpha_8)$ and $(\beta_1, \beta_2, .., \beta_8)$,

respectively)

$$
\begin{aligned}
\tilde{A}_1 &= \frac{4\alpha_1^2\alpha_2^2}{27} + \frac{16\alpha_1^3\alpha_2}{81} + \frac{8\alpha_1^4}{81} + \frac{4\alpha_1\alpha_2^3}{81} + \frac{\alpha_2^4}{162} + \frac{16\alpha_3^2\alpha_4^2}{27} \\
&\quad - \frac{32\alpha_3^3\alpha_4}{81} + \frac{8\alpha_3^4}{81} - \frac{32\alpha_3\alpha_4^3}{81} + \frac{8\alpha_4^4}{81} + \frac{16\alpha_5^2\alpha_6^2}{27} \\
&\quad - \frac{128\alpha_5^3\alpha_6}{81} + \frac{128\alpha_5^4}{81} - \frac{8\alpha_5\alpha_6^3}{81} + \frac{\alpha_6^4}{162}, \\
\tilde{A}_2 &= -\frac{20\alpha_1^2\alpha_2^2}{27} - \frac{56\alpha_1^3\alpha_2}{81} - \frac{16\alpha_1^4}{81} - \frac{26\alpha_1\alpha_2^3}{81} - \frac{4\alpha_2^4}{81} - \frac{80\alpha_3^2\alpha_4^2}{27} + \frac{112\alpha_3^3\alpha_4}{81} \\
&\quad - \frac{16\alpha_3^4}{81} + \frac{208\alpha_3\alpha_4^3}{81} - \frac{64\alpha_4^4}{81} - \frac{80\alpha_5^2\alpha_6^2}{27} + \frac{448\alpha_5^3\alpha_6}{81} - \frac{256\alpha_5^4}{81} + \frac{52\alpha_5\alpha_6^3}{81} - \frac{4\alpha_6^4}{81}, \\
\tilde{A}_3 &= \frac{11\alpha_1^2\alpha_2^2}{9} + \frac{20\alpha_1^3\alpha_2}{27} + \frac{4\alpha_1^4}{27} + \frac{20\alpha_1\alpha_2^3}{27} + \frac{4\alpha_2^4}{27} + \frac{44\alpha_3^2\alpha_4^2}{9} - \frac{40\alpha_3^3\alpha_4}{27} + \frac{4\alpha_3^4}{27} \\
&\quad - \frac{160\alpha_3\alpha_4^3}{27} + \frac{64\alpha_4^4}{27} + \frac{44\alpha_5^2\alpha_6^2}{9} - \frac{160\alpha_5^3\alpha_6}{27} + \frac{64\alpha_5^4}{27} - \frac{40\alpha_5\alpha_6^3}{27} + \frac{4\alpha_6^4}{27}, \\
\tilde{A}_4 &= -\frac{20\alpha_1^2\alpha_2^2}{27} - \frac{26\alpha_1^3\alpha_2}{81} - \frac{4\alpha_1^4}{81} - \frac{56\alpha_1\alpha_2^3}{81} - \frac{16\alpha_2^4}{81} - \frac{80\alpha_3^2\alpha_4^2}{27} + \frac{52\alpha_3^3\alpha_4}{81} \\
&\quad - \frac{4\alpha_3^4}{81} + \frac{448\alpha_3\alpha_4^3}{81} - \frac{256\alpha_4^4}{81} - \frac{80\alpha_5^2\alpha_6^2}{27} + \frac{208\alpha_5^3\alpha_6}{81} - \frac{64\alpha_5^4}{81} + \frac{112\alpha_5\alpha_6^3}{81} - \frac{16\alpha_6^4}{81}, \\
\tilde{A}_5 &= \frac{4\alpha_1^2\alpha_2^2}{27} + \frac{4\alpha_1^3\alpha_2}{81} + \frac{\alpha_1^4}{162} + \frac{16\alpha_1\alpha_2^3}{81} + \frac{8\alpha_2^4}{81} + \frac{16\alpha_3^2\alpha_4^2}{27} - \frac{8\alpha_3^3\alpha_4}{81} + \frac{\alpha_3^4}{162} \\
&\quad - \frac{128\alpha_3\alpha_4^3}{81} + \frac{128\alpha_4^4}{81} + \frac{16\alpha_5^2\alpha_6^2}{27} - \frac{32\alpha_5^3\alpha_6}{81} + \frac{8\alpha_5^4}{81} - \frac{32\alpha_5\alpha_6^3}{81} + \frac{8\alpha_6^4}{81}, \\
\tilde{A}_6 &= \frac{16\alpha_1^2\alpha_7^2}{9} + \frac{16}{9}\alpha_1\alpha_2\alpha_7^2 + \frac{4\alpha_2^2\alpha_7^2}{9} + \frac{8\alpha_3^2\alpha_8^2}{9} - \frac{16}{9}\alpha_3\alpha_4\alpha_8^2 + \frac{16}{9}\alpha_3\alpha_5\alpha_8^2 \\
&\quad - \frac{4}{9}\alpha_3\alpha_6\alpha_8^2 + \frac{8\alpha_4^2\alpha_8^2}{9} - \frac{16}{9}\alpha_4\alpha_5\alpha_8^2 + \frac{4}{9}\alpha_4\alpha_6\alpha_8^2 + \frac{32\alpha_5^2\alpha_8^2}{9} - \frac{16}{9}\alpha_5\alpha_6\alpha_8^2 + \frac{2\alpha_6^2\alpha_8^2}{9}, \\
\tilde{A}_7 &= -\frac{16}{9}\alpha_1^2\alpha_7^2 - \frac{40}{9}\alpha_1\alpha_2\alpha_7^2 - \frac{16\alpha_2^2\alpha_7^2}{9} - \frac{8\alpha_3^2\alpha_8^2}{9} + \frac{40}{9}\alpha_3\alpha_4\alpha_8^2 - \frac{16}{9}\alpha_3\alpha_5\alpha_8^2 \\
&\quad + \frac{10}{9}\alpha_3\alpha_6\alpha_8^2 - \frac{32\alpha_4^2\alpha_8^2}{9} + \frac{40}{9}\alpha_4\alpha_5\alpha_8^2 - \frac{16}{9}\alpha_4\alpha_6\alpha_8^2 - \frac{32\alpha_5^2\alpha_8^2}{9} + \frac{40}{9}\alpha_5\alpha_6\alpha_8^2 - \frac{8\alpha_6^2\alpha_8^2}{9}, \\
\tilde{A}_8 &= \frac{4\alpha_1^2\alpha_7^2}{9} + \frac{16}{9}\alpha_1\alpha_2\alpha_7^2 + \frac{16\alpha_2^2\alpha_7^2}{9} + \frac{2\alpha_3^2\alpha_8^2}{9} - \frac{16}{9}\alpha_3\alpha_4\alpha_8^2 + \frac{4}{9}\alpha_3\alpha_5\alpha_8^2 - \frac{4}{9}\alpha_3\alpha_6\alpha_8^2 \\
&\quad + \frac{32\alpha_4^2\alpha_8^2}{9} - \frac{16}{9}\alpha_4\alpha_5\alpha_8^2 + \frac{16}{9}\alpha_4\alpha_6\alpha_8^2 + \frac{8\alpha_5^2\alpha_8^2}{9} - \frac{16}{9}\alpha_5\alpha_6\alpha_8^2 + \frac{8\alpha_6^2\alpha_8^2}{9}, \\
\tilde{A}_9 &= 8\alpha_7^4 + \alpha_8^4.
\end{aligned}
\tag{3.7}
$$

$$
\begin{aligned}
\bar{A}_1 &= \frac{\beta_2^4}{16} + \frac{\beta_5^4}{2} + \frac{3\beta_2^2\beta_8^2}{8} + \frac{\beta_8^4}{16}, \quad \bar{A}_5 = \frac{\beta_1^4}{16} + \frac{3\beta_1^2\beta_3^2}{8} + \frac{\beta_3^4}{16} + \frac{\beta_6^4}{2}, \\
\bar{A}_2 &= -\frac{\beta_2^3\beta_3}{4} - 2\beta_5^3\beta_6 + \frac{3\beta_1\beta_2^2\beta_8}{4} - \frac{3\beta_2\beta_3\beta_8^2}{4} + \frac{\beta_1\beta_8^3}{4}, \\
\bar{A}_3 &= \frac{3\beta_1^2\beta_2^2}{8} + \frac{3\beta_2^2\beta_3^2}{8} + 3\beta_5^2\beta_6^2 - \frac{3\beta_1\beta_2\beta_3\beta_8}{2} + \frac{3\beta_1^2\beta_8^2}{8} + \frac{3\beta_3^2\beta_8^2}{8}, \\
\bar{A}_4 &= -\frac{3\beta_1^2\beta_2\beta_3}{4} - \frac{\beta_2\beta_3^3}{4} - 2\beta_5\beta_6^3 + \frac{\beta_1^3\beta_8}{4} + \frac{3\beta_1\beta_3^2\beta_8}{4}, \\
\bar{A}_6 &= \frac{\beta_2^2\beta_4^2}{2} + 4\beta_5^2\beta_7^2 + \frac{3\beta_4^2\beta_8^2}{2}, \quad \bar{A}_7 = -\beta_2\beta_3\beta_4^2 - 8\beta_5\beta_6\beta_7^2 + 3\beta_1\beta_4^2\beta_8, \\
\bar{A}_8 &= \frac{3\beta_1^2\beta_4^2}{2} + \frac{\beta_3^2\beta_4^2}{2} + 4\beta_6^2\beta_7^2, \quad \bar{A}_9 = \beta_4^4 + 8\beta_7^4.
\end{aligned}
\tag{3.8}
$$

The above results are identical to those given by Soare and Barlat [69] and by Uppaluri and Helm [74] respectively. It is noted that $(A_1, A_2, ..., A_9)$ = (1, -2, 3, -2, 1, 6, -6, 6, 9) when $(\alpha_1, \alpha_2, ..., \alpha_8)$=$(\beta_1, \beta_2, ..., \beta_8)$ = (1, 1, 1, 1, 1, 1, 1, 1), corresponding to the squared von Mises yield function in plane stress.

Clearly, unlike the parameter identification of nine coefficients $(A_1, A_2, ..., A_9)$ or their Fourier coefficients $(F_0, F_1, F_2, F_3, F_4, G_0, G_1, G_2, H_0)$ where only linear equations are involved [36,72,77], the determination of eight constants, either $(\alpha_1, \alpha_2, ..., \alpha_8)$ or $(\beta_1, \beta_2, ..., \beta_8)$, requires the solution of a set of fourth-order equations. However, once the real-valued either $(\alpha_1, \alpha_2, ..., \alpha_8)$ or $(\beta_1, \beta_2, ..., \beta_8)$ are successfully obtained numerically via parameter identification, the positivity and convexity of Yld2000-2d is also simultaneously certified [20]. An additional step of convexity certification is required to carry out either algebraically or numerically for an as-calibrated Gotoh's fourth-order polynomial yield function [66,67,71,74,78].

3.3 Fourth-order Yield Functions of Reduced Plastic Anisotropy

Fourth-order Yld2000-2d yield functions have only up to eight material constants, so they are only a subset of all possible convex fourth-order polynomials (which include up to nine independent polynomial coefficients). That is, with respect to the complete fourth-order yield function, a fourth-order Yld2000-2d models a sheet metal with *reduced plastic anisotropy* as discussed by Tong [72]. To make a more direct and meaningful comparison between Gotoh's yield functions and Yld2000-2d functions, both polynomial coefficients $(A_1, A_2, ..., A_9)$ and the material constants $(\alpha_1, \alpha_2, ..., \alpha_8)$ or $(\beta_1, \beta_2, ..., \beta_8)$ shall be calibrated from the same

types and numbers (up to eight) of experimental inputs.

Typical experimental inputs for sheet metal plasticity modeling include yield stresses σ_θ and plastic strain ratios R_θ under uniaxial tension at various loading angles θ plus yield stress σ_b and plastic strain ratio R_b under equal biaxial tension [20, 34, 36, 66, 72, 77]. By common practice, the yield stress σ_0 (along the rolling direction of the sheet metal) is used as its equivalent flow strength $\sigma_f = \sigma_0$, so $A_1 = 1$ holds for the polynomial yield function in this study. Due to the equivalency of the original and compact forms of Yld2000-2d given in Eq.(3.4) and Eq.(3.5), much simpler results relating $(A_1, A_2, ..., A_9)$ and $(\beta_1, \beta_2, ..., \beta_8)$ will mostly be used from now on. Calibration of various fourth-order yield functions of the two formulations will be described in details with only three, five, seven or eight independent experimental inputs in the following. First three cases of reduced plastic anisotropy have previously been studied by Tong [72] for Gotoh's yield function only.

3.3.1 In-plane Isotropic Yield Functions with Three Inputs $(\sigma_0, \sigma_b, R_0)$

This is the simplest case when the sheet metal has in-plane isotropy with $\sigma_\theta = \sigma_0$ and $R_\theta = R_0$. One can show that Gotoh's yield function will have three independent polynomial coefficients (A_1, A_2, A_3) and six dependent ones $(A_4, ..., A_9)$ [72, 76]. In terms of the two principal stresses, the in-plane isotropic Gotoh's yield function of Eq.(3.2) becomes (i.e., non-zero Fourier coefficients are only $F_0 = A_1$, $G_0 = A_2$ and $H_0 = A_3$)

$$\phi_{gio}(\sigma_1, \sigma_2) = A_1\sigma_1^4 + A_2\sigma_1^3\sigma_2 + A_3\sigma_1^2\sigma_2^2 + A_2\sigma_1\sigma_2^3 + A_1\sigma_2^4, \tag{3.9}$$

where

$$\begin{aligned}
&A_5 = A_1 = 1, \quad A_4 = A_2 = -\frac{4R_0}{1+R_0}, \quad A_3 = \frac{6R_0 - 2}{1+R_0} + (\frac{\sigma_0}{\sigma_b})^4, \\
&A_6 = A_8 = 4A_1 - A_2 = \frac{4 + 8R_0}{1+R_0}, \\
&A_7 = 4A_1 + 2A_2 - 2A_3 = \frac{8 - 16R_0}{1+R_0} - 2(\frac{\sigma_0}{\sigma_b})^4, \\
&A_9 = 2A_1 - 2A_2 + A_3 = \frac{16R_0}{1+R_0} + (\frac{\sigma_0}{\sigma_b})^4.
\end{aligned} \tag{3.10}$$

One can show that a planarly isotropic fourth-order Yld2000-2d has only three indepen-

dent material constants $(\beta_1, \beta_2, \beta_5)$ because

$$\beta_8 = \beta_1, \quad \beta_3 = \beta_2, \quad \beta_4^2 = \beta_2^2, \quad \beta_6 = \beta_5, \quad \beta_7^2 = \beta_5^2. \tag{3.11}$$

The relationship between polynomial coefficients $(A_1, A_2, ..., A_9)$ and material constants $(\beta_1, \beta_2, ..., \beta_8)$ per Eq.(3.8) is thus simplified as

$$\begin{aligned} A_1 &= \frac{\beta_1^4}{16} + \frac{3\beta_1^2\beta_2^2}{8} + \frac{\beta_2^4}{16} + \frac{\beta_5^4}{2}, \quad A_2 = \frac{\beta_1^4}{4} - \frac{\beta_2^4}{4} - 2\beta_5^4, \\ A_3 &= \frac{3\beta_1^4}{8} - \frac{3\beta_1^2\beta_2^2}{4} + \frac{3\beta_2^4}{8} + 3\beta_5^4. \end{aligned} \tag{3.12}$$

In fact, one can obtain the algebraic expressions of $(\beta_1, \beta_2, \beta_5)$ in terms of (A_1, A_2, A_5) from Eq.(3.12) as

$$\begin{aligned} \beta_1^2 &= \sqrt{2A_1 + 2A_2 + A_3}, \quad \beta_2^2 = \frac{6A_1 - A_3}{3\sqrt{2A_1 + 2A_2 + A_3}}, \\ \beta_5^4 &= \frac{12A_1A_3 + 2A_3^2 - 9A_2^2}{18(2A_1 + 2A_2 + A_3)}. \end{aligned} \tag{3.13}$$

The condition for the Yld2000-2d yield function to be positive and convex is to ensure that all $(\beta_1, \beta_2, \beta_5)$ are real-valued or in terms of (A_1, A_2, A_5) as

$$2A_1 + 2A_2 + A_3 \geq 0, \quad 6A_1 - A_3 \geq 0, \quad 12A_1A_3 + 2A_3^2 - 9A_2^2 \geq 0. \tag{3.14}$$

Recall that the necessary and sufficient condition for an in-plane isotropic Gotoh's yield function to be positive and convex has just recently been reported by Tong [67] as (this is a special case of Eq.(3.18) below with $A_5 = A_1$ and $A_4 = A_2$ due to in-plane isotropy)

$$\begin{aligned} &6A_1 + A_3 \geq 0, \quad 24A_1A_3 + 36A_1^2 - 9A_2^2 - A_3^2 \geq 0, \\ &72A_1^2A_3 + 9A_2^2A_3 - 2A_3^3 - 54A_1A_2^2 \geq 0. \end{aligned} \tag{3.15}$$

It turns out that these two convexity conditions given by Eq.(3.14) and Eq.(3.15) are equivalent, noting

$$(6A_1 - A_3)(12A_1A_3 + 2A_3^2 - 9A_2^2) = 72A_1^2A_3 + 9A_2^2A_3 - 2A_3^3 - 54A_1A_2^2. \tag{3.16}$$

The convex domain (the intersection among all three individual domains) of each yield function defined by the inequalities per Eq.(3.14) or Eq.(3.15) is graphically shown in Fig.3.1 over the mechanical property space (η_0, b), where the plastic thinning ratio $\eta_0 = 1/(1+R_0) \in (0,2)$ with $R_0 > -0.5$ and the stress ratio $b = \sigma_0/\sigma_b \in (0,2)$ [67, 71, 78]. That is, in-plane isotropic fourth-order Gotoh's and Yld2000-2d yield functions are shown algebraically to be identical in terms of the number of independent polynomial coefficients and material constants and the size of their convex domains (η_0, b) are the same.

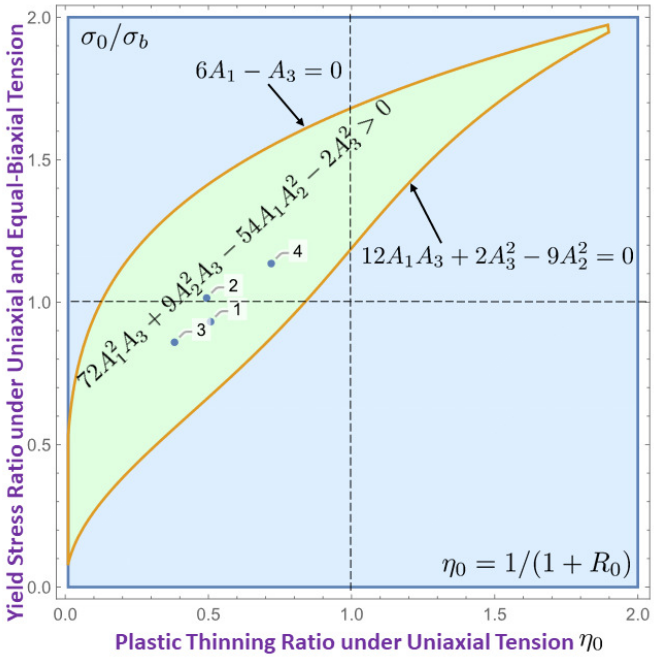

Figure 3.1: Convex domains of in-plane isotropic Gotoh's and Yld2000-2d yield functions.

3.3.2 Yield Functions Based on On-axis Five Inputs $(\sigma_0, \sigma_{90}, \sigma_b, R_0, R_{90})$

When only yield stresses and plastic strain ratios under on-axis loading ($\theta = 0^o$ or $\theta = 90^o$) are made available, one may assume $F_2 = F_3 = F_4 = G_2 = 0$ in Eq.(3.3) so all nine polynomial coefficients of Gotoh's yield function may still be obtained [72, 76]. That

is, the five *independent* on-axis coefficients $(A_1, A_2, A_3, A_4, A_5)$ and four *dependent* off-axis coefficients (A_6, A_7, A_8, A_9) are now given as

$$
\begin{aligned}
&A_1 = 1,\ A_2 = -\frac{4R_0}{1+R_0},\ A_3 = \frac{3R_0-1}{1+R_0} + \frac{3R_{90}-1}{1+R_{90}}(\frac{\sigma_0}{\sigma_{90}})^4 + (\frac{\sigma_0}{\sigma_b})^4,\\
&A_4 = -\frac{4R_{90}}{1+R_{90}}(\frac{\sigma_0}{\sigma_{90}})^4,\ \ A_5 = (\frac{\sigma_0}{\sigma_{90}})^4,\\
&A_6 = 3A_1 - A_2 + A_5 = \frac{3+7R_0}{1+R_0} + (\frac{\sigma_0}{\sigma_{90}})^4,\\
&A_7 = 2A_1 + A_2 - 2A_3 + A_4 + 2A_5 = \frac{4-8R_0}{1+R_0} + \frac{4-8R_{90}}{1+R_{90}}(\frac{\sigma_0}{\sigma_{90}})^4 - 2(\frac{\sigma_0}{\sigma_b})^4,\\
&A_8 = A_1 - A_4 + 3A_5 = 1 + \frac{3+7R_{90}}{1+R_{90}}(\frac{\sigma_0}{\sigma_{90}})^4,\\
&A_9 = A_1 - A_2 + A_3 - A_4 + A_5 = \frac{8R_0}{1+R_0} + \frac{8R_{90}}{1+R_{90}}(\frac{\sigma_0}{\sigma_{90}})^4 + (\frac{\sigma_0}{\sigma_b})^4.
\end{aligned}
\tag{3.17}
$$

The convexity of Gotoh's yield function requires an additional certification step. One should first verify the following necessary and sufficient conditions on $(A_1, ..., A_5)$ for a convex Gotoh's function $\Phi_g(\sigma_x, \sigma_y, 0)$ [67, 78]

$$
\begin{aligned}
&\Psi_1 = 3A_1 + A_3 + 3A_5 \geq 0,\\
&\Psi_2 = 24A_1A_3 + 72A_1A_5 + 24A_3A_5 - 9A_2^2 - 2A_3^2 - 9A_4^2 \geq 0,\\
&\Psi_3 = 72A_1A_3A_5 + 9A_2A_3A_4 - 2A_3^3 - 27A_1A_4^2 - 27A_2^2A_5 \geq 0,
\end{aligned}
\tag{3.18}
$$

and then the sufficient condition on the entire set of $(A_1, ..., A_9)$ by requiring the following 9-by-9 matrix to be positive semidefinite

$$\begin{pmatrix} 12A_1 & 3A_2 & 0 & 3A_2 & 2A_3 & 0 & 0 & 0 & 2A_6 \\ 3A_2 & 2A_3 & 0 & 2A_3 & 3A_4 & 0 & 0 & 0 & A_7 \\ 0 & 0 & 2A_6 & 0 & 0 & A_7 & 2A_6 & A_7 & 0 \\ 3A_2 & 2A_3 & 0 & 2A_3 & 3A_4 & 0 & 0 & 0 & A_7 \\ 2A_3 & 3A_4 & 0 & 3A_4 & 12A_5 & 0 & 0 & 0 & 2A_8 \\ 0 & 0 & A_7 & 0 & 0 & 2A_8 & A_7 & 2A_8 & 0 \\ 0 & 0 & 2A_6 & 0 & 0 & A_7 & 2A_6 & A_7 & 0 \\ 0 & 0 & A_7 & 0 & 0 & 2A_8 & A_7 & 2A_8 & 0 \\ 2A_6 & A_7 & 0 & A_7 & 2A_8 & 0 & 0 & 0 & 12A_9 \end{pmatrix} \geq 0. \tag{3.19}$$

When it fails, one may ultimately check the positivity of three leading principal minors of Hessian matrix of $\Phi_g(\sigma_x, \sigma_y, \tau_{xy})$ via a numerical minimization method [71,72,79]. The same convexity certification step shall also be applicable to the following two cases using either seven or eight independent inputs.

For the case of only five inputs, three additional conditions have to be introduced for Yld2000-2d yield function, so its eight material constants $(\beta_1...\beta_8)$ may be determined. There are a total of six material constants $(\beta_1, \beta_2, \beta_3, \beta_5, \beta_6, \beta_8)$ of the fourth order Yld2000-2d that are related to the independent five polynomial coefficients $(A_1, A_2, A_3, A_4, A_5)$ per Eq.(3.8). One may simply set $\beta_8 = \beta_1$ to remove one redundant material constant, the remaining five of them are independent and may be determined. Unlike the case of in-plane isotropy above, one could not obtain in general explicit algebraic relationships of $(\beta_1, \beta_2, \beta_3, \beta_5, \beta_6)$ in terms of known $(A_1, A_2, A_3, A_4, A_5)$. Numerical solutions of a set of five fourth-order equations are required instead, namely

$$\begin{aligned} &\bar{A}_1(\beta_2, \beta_5, \beta_8) = A_1, \ \bar{A}_2(\beta_1, \beta_2, \beta_3, \beta_5, \beta_6, \beta_8) = A_2, \ \bar{A}_5(\beta_1, \beta_3, \beta_6) = A_5, \\ &\bar{A}_3(\beta_1, \beta_2, \beta_3, \beta_5, \beta_6, \beta_8) = A_3, \quad \bar{A}_4(\beta_1, \beta_2, \beta_3, \beta_5, \beta_6, \beta_8) = A_4, \end{aligned} \tag{3.20}$$

where $(A_1, A_2, A_3, A_4, A_5)$ are known polynomial coefficients given in Eq.(3.17) and $(\bar{A}_1, \bar{A}_2, \bar{A}_3,$

$\bar{A}_4, \bar{A}_5$) are the five four-order functions of $(\beta_1, \beta_2, \beta_3, \beta_5, \beta_6)$ as given in Eq.(3.8), noting $\beta_8 = \beta_1$ here. There are numerous possible choices for determining the two other dependent material constants (β_4, β_7), among them are

$$\begin{aligned}
&\text{case (a)} : \beta_4 = \beta_7 = 1, \\
&\text{case (b)} : \bar{A}_6(\beta_4, \beta_7) = A_6, \quad \bar{A}_7(\beta_4, \beta_7) = A_7, \\
&\text{case (c)} : \bar{F}_3(\beta_4, \beta_7) = F_3 = 0, \quad \bar{F}_4(\beta_4, \beta_7) = F_4 = 0, \\
&\text{case (d)} : \text{minimize} \quad \delta_1(\beta_4, \beta_7),
\end{aligned} \tag{3.21}$$

where the objective function of the least-square minimization is given as

$$\delta_1(\beta_4, \beta_7) = \sum_{k=6}^{9} [\bar{A}_k(\beta_4, \beta_7) - A_k]^2, \tag{3.22}$$

(A_6, A_7, A_8, A_9) are the known dependent polynomial coefficients given in Eq.(3.17) and $(\bar{A}_6, \bar{A}_7, \bar{A}_8, \bar{A}_9)$ are four four-order functions of the dependent material constant (β_4, β_7) as given in Eq.$(3.8)_6$ to Eq.$(3.8)_9$, noting that other six material constants have already been first determined above. In the case (c) above, the Fourier coefficients $\bar{F}_3$ and $\bar{F}_4$ are given in terms of $(\bar{A}_1, ..., \bar{A}_9)$ of Eq.(3.8) while F_3 and F_4 are given in terms of $(A_1, ..., A_9)$ of Eq.(3.17).

If one does not set $\beta_8 = \beta_1$ as a prior, then a total of eight nonlinear equations have to be solved simultaneously for obtaining $(\beta_1, ..., \beta_8)$, that is, the five fourth-order equations of Eq.(3.20) and plus the following set of three nonlinear equations

$$\begin{aligned}
\text{case (e)} : \bar{A}_6(\beta_2, \beta_4, \beta_5, \beta_7, \beta_8) = A_6, \quad \bar{A}_7(\beta_1, ..., \beta_8) = A_7, \\
\bar{A}_8(\beta_1, \beta_3, \beta_4, \beta_6, \beta_7) = A_8,
\end{aligned} \tag{3.23}$$

Alternatively, with five on-axis material constants $(\beta_1, \beta_2, \beta_3, \beta_5, \beta_6)$ being constrained per Eq.(3.20), the least-square minimization may be used to find the optimal $(\beta_4, \beta_7, \beta_8)$

with the following objective functions

$$\begin{aligned}\text{case (f)}: \text{minimize} \quad & \bar{F}_2^2(\beta_4,\beta_7,\beta_8)+\bar{F}_3^2(\beta_4,\beta_7,\beta_8)\\ & +\bar{F}_4^2(\beta_4,\beta_7,\beta_8)++\bar{G}_4^2(\beta_4,\beta_7,\beta_8),\\ \text{case (g)}: \text{minimize} \quad & \delta_2(\beta_4,\beta_7,\beta_8),\end{aligned} \tag{3.24}$$

where

$$\delta_2(\beta_4,\beta_7,\beta_8)=\sum_{k=6}^{9}[\bar{A}_k(\beta_4,\beta_7,\beta_8)-A_k]^2. \tag{3.25}$$

Finally, one may simply use the least-square minimization for determining the entire set of eight material constants with an objective function of either δ_{3a} or δ_{3b} (as cases h1 for first eight and h2 for all nine polynomial coefficients, respectively)

$$\begin{aligned}\delta_{3a}(\beta_1,...,\beta_8)&=\sum_{k=2}^{8}[\bar{A}_k(\beta_1,...,\beta_8)-A_k]^2, \quad \bar{A}_1(\beta_2,\beta_5,\beta_8)=A_1,\\ \delta_{3b}(\beta_1,...,\beta_8)&=\sum_{k=2}^{9}[\bar{A}_k(\beta_1,...,\beta_8)-A_k]^2, \quad \bar{A}_1(\beta_2,\beta_5,\beta_8)=A_1.\end{aligned} \tag{3.26}$$

3.3.3 Yield Functions Based on Standard Eight Inputs for Yld2000-2d

Eight experimental inputs consisting of four yield stresses and four plastic strain ratios $(\sigma_0,\sigma_{45},\sigma_{90},\sigma_b,R_0,R_{45},R_{90},R_b)$ are most commonly used for parameter identification of Yld2000-2d [20,41,70]. As pointed out in earlier studies on Gotoh's fourth-order polynomial yield function [72,77], seven of them are independent. Accordingly, these seven inputs (excluding the redundant R_b) lead to only six determinant polynomial coefficients $(A_1,...,A_5,A_9)$ plus a restrictive condition on the remaining three off-axis coefficients (A_6,A_7,A_8) [36,66,72,74,80]

$$\begin{aligned}&A_1=1,\ A_3=\frac{3R_0-1}{1+R_0}+\frac{3R_{90}-1}{1+R_{90}}\left(\frac{\sigma_0}{\sigma_{90}}\right)^4+\left(\frac{\sigma_0}{\sigma_b}\right)^4,\\ &A_2=-\frac{4R_0}{1+R_0},\ A_4=-\frac{4R_{90}}{1+R_{90}}\left(\frac{\sigma_0}{\sigma_{90}}\right)^4,\ \ A_5=\left(\frac{\sigma_0}{\sigma_{90}}\right)^4,\\ &A_9=\frac{16R_{45}}{1+R_{45}}\left(\frac{\sigma_0}{\sigma_{45}}\right)^4+A_1+A_2+A_3+A_4+A_5,\\ &A_6+A_7+A_8=\frac{16}{1+R_{45}}\left(\frac{\sigma_0}{\sigma_{45}}\right)^4-2(A_1+A_2+A_3+A_4+A_5).\end{aligned} \tag{3.27}$$

When the plastic strain ratio R_b under equal biaxial tension is used instead of σ_b and $R_b \neq 1$, only the material constant A_3 will be affected and it is computed as [72]

$$A_3 = \frac{-2R_0 - 2R_b + 4R_0R_b}{(1+R_0)(-1+R_b)} + \frac{2 - 4R_{90} + 2R_{90}R_b}{(1+R_{90})(-1+R_b)}(\frac{\sigma_0}{\sigma_{90}})^4. \tag{3.28}$$

If both σ_b and R_b are included in parameter identification, one can simply use the average of these two A_3 values from Eq.(3.27)$_2$ and Eq.(3.28).

Due to lack of two required off-axis uniaxial tensile test measurements for the sheet metal under consideration, one may assume that its uniaxial yielding and plastic flow behavior has a reduced degree of planar anisotropy by setting its two higher-order Fourier coefficients F_3 and F_4 in Eq.(3.3) to be zero. So the remaining three off-axis coefficients (A_6, A_7, A_8) are [72]

$$\begin{aligned} A_6 &= \frac{1+5R_0}{1+R_0} + 4(\frac{\sigma_0}{\sigma_{45}})^4 - (\frac{\sigma_0}{\sigma_{90}})^4, \\ A_7 &= -\frac{4R_0}{1+R_0} + \frac{8-8R_{45}}{1+R_{45}}(\frac{\sigma_0}{\sigma_{45}})^4 - \frac{4R_{90}}{1+R_{90}}(\frac{\sigma_0}{\sigma_{90}})^4 - 2(\frac{\sigma_0}{\sigma_b})^4, \\ A_8 &= -1 + 4(\frac{\sigma_0}{\sigma_{45}})^4 + \frac{1+5R_{90}}{1+R_{90}}(\frac{\sigma_0}{\sigma_{90}})^4. \end{aligned} \tag{3.29}$$

There are two options in parameter identification of a fourth-order Yld2000-2d using the standard eight inputs. The first one is to set $\beta_8 = \beta_1$, so its seven remaining materials constants $(\beta_1, \beta_2, ..., \beta_7)$ can be obtained by numerical solution of seven fourth-order equations: solving first for $(\beta_1, \beta_2, \beta_3, \beta_5, \beta_6)$ of Eq.(3.20) and then the following two equations for β_4 and β_7

$$\begin{aligned} &\bar{A}_9(\beta_4, \beta_7) = A_9, \\ &\bar{A}_6(\beta_4, \beta_7) + \bar{A}_7(\beta_4, \beta_7) + \bar{A}_8(\beta_4, \beta_7) = A_6 + A_7 + A_8, \end{aligned} \tag{3.30}$$

where A_9 and $A_6 + A_7 + A_8$ are known polynomial coefficients given in Eq.(3.27) and $(\bar{A}_6, \bar{A}_7, \bar{A}_8, \bar{A}_9)$ are four-order functions of (β_4, β_7) as given in Eq.(3.8).

The second option is not to set $\beta_8 = \beta_1$ but use three additional equations along with the five ones of Eq.(3.20) for numerically determining the eight material constants $(\beta_1, \beta_2, ..., \beta_8)$

$$\begin{aligned} &\bar{A}_6(\beta_1, ..., \beta_8) + \bar{A}_7(\beta_1, ..., \beta_8) + \bar{A}_8(\beta_1, ..., \beta_8) = A_6 + A_7 + A_8, \\ &\bar{A}_7(\beta_1, .., \beta_8) = A_7, \quad \bar{A}_9(\beta_1, .., \beta_8) = A_9. \end{aligned} \tag{3.31}$$

3.3.4 Yield Functions Based on Independent Eight Inputs

One can in fact add one more experimental input such as σ_θ or R_θ from another off-axis tension test (with $\theta \neq 0^o, 45^o, 90^o$) to realize the full modeling capabilities of the fourth-order Yld2000-2d with eight independent material constants. For Gotoh's polynomial yield function, in addition to set the Fourier coefficient $F_4 = 0$, one has an extra equation based on the experimental σ_θ to make up the two needed linear equations, namely

$$\begin{aligned}
&A_1 - A_2 + A_3 - A_4 + A_5 - A_6 + A_7 - A_8 + A_9 = 0, \\
&\frac{1}{128}(35A_1 + 5A_2 + 3A_3 + 5A_4 + 35A_5 + 5A_6 + 3A_7 + 5A_8 + 3A_9) \\
&+ \frac{1}{32}(14A_1 + A_2 - A_4 - 14A_5 + A_6 - A_8)\cos 2\theta \\
&+ \frac{1}{32}(7A_1 - A_2 - A_3 - A_4 + 7A_5 - A_6 - A_7 - A_8 - A_9)\cos 4\theta \\
&+ \frac{1}{32}(2A_1 - A_2 + A_4 - 2A_5 - A_6 + A_8)\cos 6\theta = (\frac{\sigma_0}{\sigma_\theta})^4.
\end{aligned} \tag{3.32}$$

If an extra R_θ is used instead, a similar but more lengthy equation in terms of linear combinations of nine polynomial coefficients can be used to substitute the above mentioned second equation. One may consult the results given elsewhere for its detailed derivation [72].

Without presetting $\beta_8 = \beta_1$, one may simply use the following eight nonlinear equations for simultaneously solving all eight material constants for Yld2000-2d (noting β_8 appears in $\bar{A}_1, \bar{A}_2, \bar{A}_3, \bar{A}_4, \bar{A}_6$ and $\bar{A}_7$ per Eq.(3.8))

$$\begin{aligned}
&\bar{A}_1(\beta_2, \beta_5, \beta_8) = A_1, \quad \bar{A}_2(\beta_1, \beta_2, \beta_3, \beta_5, \beta_6, \beta_8) = A_2, \\
&\bar{A}_3(\beta_1, \beta_2, \beta_3, \beta_5, \beta_6, \beta_8) = A_3, \quad \bar{A}_4(\beta_1, \beta_2, \beta_3, \beta_5, \beta_6, \beta_8) = A_4, \\
&\bar{A}_5(\beta_1, \beta_3, \beta_6) = A_5, \quad \bar{A}_8(\beta_1, \beta_3, \beta_4, \beta_6, \beta_7) = A_8, \quad \bar{A}_9(\beta_4, \beta_7) = A_9, \\
&\bar{A}_6(\beta_2, \beta_4, \beta_5, \beta_7, \beta_8) + \bar{A}_7(\beta_1, \beta_1, \beta_3, \beta_4, \beta_5, \beta_6, \beta_7, \beta_8) = A_6 + A_7,
\end{aligned} \tag{3.33}$$

where the nine polynomial coefficients $(A_1, ..., A_9)$ are obtained from Eq.(3.27) and Eq.(3.32).

3.4 Modeling Results on Selected Sheet Metals

We now apply Gotoh's and Yld2000-2d fourth-order yield functions of reduced plastic anisotropy for modeling selected sheet metals using the same three, five, seven or eight exper-

imental inputs in their parameter identification as detailed in the previous section. To make the comparative evaluations more explicit and relevant for a typical application, four selected sheet metals (2 FCC and 2 BCC) with eleven experimental inputs ($\sigma_0, \sigma_{225}, \sigma_{45}, \sigma_{675}, \sigma_{90}, \sigma_b$, $R_0, R_{225}, R_{45}, R_{675}, R_{90}$) are included in this study [36, 70, 81], see Table 3.1. R-values at the plastic strain of 1% are used for the two sheet metals reported by Aamaishi et al. [81]. These types and numbers of experimental inputs were first used by Gotoh [36] for parameter identification. Numerical results for calibrated material parameters are reported up to six significant digits in this study.

Table 3.1: Four selected sheet metals with their eleven experimental inputs

Metal No.	1	2	3	4
Material	Cu-1/4H[a]	DP780 Steel	Mild Steel	AA6XXX
σ_f/σ_0	1	1	1	1
σ_{225}/σ_0	0.973393	1.065	1.0268	1.1091
σ_{45}/σ_0	0.944059	1.07	1.0102	0.8359
σ_{675}/σ_0	0.955903	1.060	1.0230	0.8471
σ_{90}/σ_0	0.954847	1.00	1.0332	0.9439
σ_b/σ_0	1.0316	1.02	1.1794[b]	0.7960[b]
R_0	0.818182	0.93	1.63	0.72
R_{225}	0.928552	0.91	1.49	0.42
R_{45}	1.1101	0.99	1.51	0.21
R_{675}	0.930079	1.155	1.66	0.37
R_{90}	0.842266	1.19	1.83	0.42
σ_{ave}/σ_0	0.960741	1.035	1.0134	0.9039
R_{ave}	0.970161	1.025	1.62	0.39
Source	[36]	[70]	[81]	[81]

(a) Based on reported $(A_1, ..., A_9)$; (b) Based on Hill's 1948p yield function [79].

3.4.1 Yield Functions Based on Three Experimental Inputs

Using (σ_{ave}, R_{ave}) in place of (σ_0, R_0) as given for the four selected sheets #1–#4 in Table 1, both the polynomial coefficients $(A_1, ..., A_9)$ of Gotoh's yield function and material constants $(\beta_1, ..., \beta_8)$ of Yld2000-2d ($M = 4$) are obtained using Eq.(3.10) and Eq.(3.13). Their results are listed in Table 3.2. For completeness and due to its more popular use in the literature, corresponding results on material constants $(\alpha_1, ..., \alpha_8)$ of Yld2000-2d via linear

equations of Eq.(3.6) are also given in Table 3.2. Obviously, all calibrated Gotoh's yield functions of the four sheet metals are convex as shown in Fig.3.1.

A total of all eight sets of real-valued material constants $(\beta_1, ..., \beta_8)$ are presented for sheet metal #1 in Table 3.2 to illustrate the non-uniqueness of solutions of nonlinear Eq.(3.13) based on the known (A_1, A_2, A_3). Those eight variants of Yld2000-2d for this sheet metal are completely equivalent to its Gotoh's fourth-order yield functions with identical polynomial coefficients as listed in Table 3.2. By some tacit convention, most authors have reported only one set of mostly positively-valued material constants for Yld2000-2d yield functions in the literature. Accordingly, only one out of eight sets of real-valued material constants $(\beta_1, ..., \beta_8)$ are listed for other three sheet metals in Table 3.2. We will follow such a practice whenever possible in the rest of the paper as well.

Biaxial tensile yield surfaces $\phi_{gio}(\sigma_1, \sigma_2) = \Phi_g(\sigma_x, \sigma_y, 0) = \sigma_f^4$ of Eq.(3.9) along with its plastic flow directions are shown in Fig.3.2(a) and Fig.3.2(b) respectively for these four representative sheet metals. Here, the direction of the axial stress vector (σ_x, σ_y) is defined by the angle $\alpha = \tan^{-1}(\sigma_y/\sigma_x)$ and the plastic flow direction of the axial plastic strain increment vector $(\dot{\varepsilon}_x^p, \dot{\varepsilon}_y^p)$ is defined by the angle $\beta = \tan^{-1}(\dot{\varepsilon}_y^p/\dot{\varepsilon}_x^p)$, see the insert of Fig.3.2(b) for illustration. It is seen that a four-order yield function is capable of modeling a wide range of biaxial yield surface shapes.

3.4.2 Yield Functions Based on Five Experimental Inputs

The parameters of calibrated Gotoh's and Yld2000-2d yield functions based on five on-axis experimental inputs $(\sigma_0, \sigma_{90}, \sigma_b, R_0, R_{90})$ of Table 3.1 are listed in Table 3.3 for the selected four sheet metals. The first set of $(A_2, ..., A_9)$ for each metal in Table 3.3 were computed directly from Eq.(3.17) with $A_1 = 1$ for all cases due to setting $\sigma_f = \sigma_0$. All calibrated Gotoh's yield functions of the four sheet metals listed in Table 3.3 were found to be strictly positive and convex as per the sufficient condition of Eq.(3.19).

For sheet metal #1, eight material constants $(\beta_1, ..., \beta_8)$ of Yld2000-2d in all nine cases from (a) to (h1) and (h2) were computed per the procedure described in Section 3.3.2 and their values are also listed in Table 3.3. Results from cases (e) and (h1) of Yld2000-2d are found to be completely identical : the least square minimization of δ_{3a} of Eq.(3.26) and

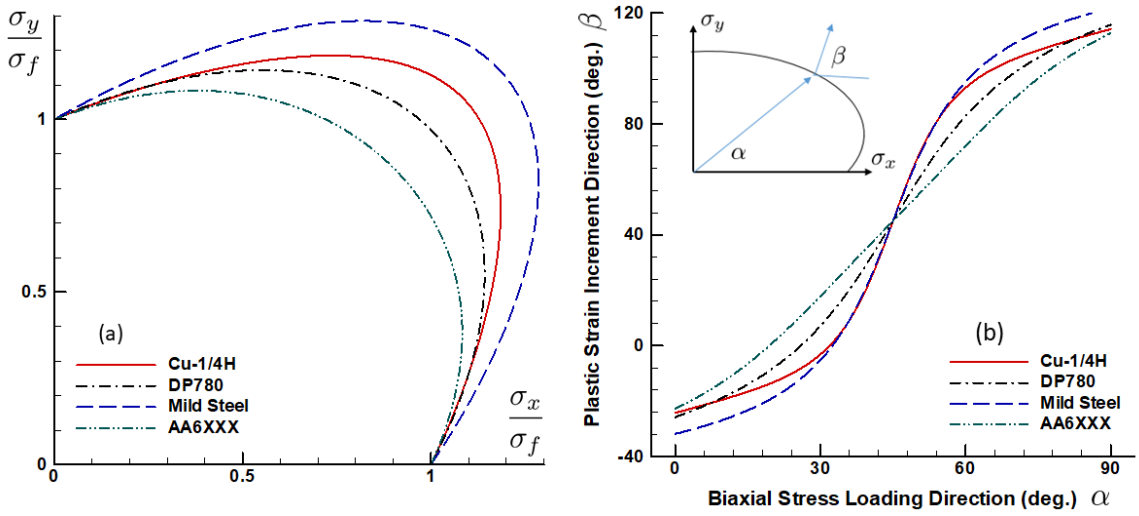

Figure 3.2: Biaxial tensile yield surfaces (a) and plastic flow directions (b) of four sheet metals with in-plane isotropy.

the solution of eight nonlinear equations of Eq.(3.20) and Eq.(3.23) are equivalent for convex yield functions (i.e. the minimized $\delta_{3a} = 0$)[1]. For other three sheet metals, two representative cases (c) and (e) of calibrated fourth-order Yld2000-2d yield functions are listed in Table 3.3. For each Yld2000-2d yield function, both the corresponding material constants $(\alpha_1, ..., \alpha_8)$ based on Eq.(3.6) and their polynomial coefficients $(\bar{A}_2, ..., \bar{A}_9)$ per Eq.(3.8) are also listed in Table 3.3. The latter results are shown immediately following those of Gotoh's yield function in the table for direct comparison. The value of a polynomial coefficient from a Yld2000-2d yield function is left to be blank if it is identical to that of Gotoh's yield function. For sheet metal #1, only values of (β_4, β_7) and (α_7, α_8) are given in Table 3.3 for cases (b)-(d) of Yld2000-2d as their other six material constants are identical to those of case (a).

Predicted biaxial tensile yield surfaces based on Gotoh's polynomial yield function $\Phi_g(\sigma_x, \sigma_y, 0) = \sigma_f^4$ of Eq.(3.1) are shown in Fig.3.3 for the four sheet metals. Their experimental yield stresses $(\sigma_0, \sigma_{90}, \sigma_b)$ are shown as open circles in the figure. Biaxial tensile yield surfaces given by cases (a) to (h1) of Yld2000-2d are not shown separately as they have the

[1] In the case of a calibrated set of $(A_1, ..., A_8)$ leading to a non-convex fourth-order function, a solution of real-valued material constants from these eight nonlinear equations would be impossible.

Table 3.2: List of yield function parameters for four sheet metals with three inputs

Material	A_2	A_3	A_4	A_5	A_6	A_7	A_8	A_9
Cu-1/4H	-1.80000	2.35228	-1.80000	1.00000	5.80000	-4.30456	5.80000	7.95228
DP780	-1.92746	2.91506	-1.92746	1.00000	5.92746	-5.68503	5.92746	8.76998
Mild Steel	-2.47909	3.50328	-2.47909	1.00000	6.47909	-7.96473	6.47909	10.4615
AA6XXX	-1.67442	3.01160	-1.67442	1.00000	5.67442	-5.37203	5.67442	8.36043
	β_1	β_2	β_3	β_4	β_5	β_6	β_7	β_8
Cu-1/4H	0.93131	1.18401	1.18401	1.18401	±0.93010	±0.93010	±0.93010	0.93131
	0.93131	-1.18401	-1.18401	-1.18401	±0.93010	±0.93010	±0.93010	0.93131
	-0.93131	1.18401	1.18401	1.18401	±0.93010	±0.93010	±0.93010	-0.93131
	-0.93131	-1.18401	-1.18401	-1.18401	±0.93010	±0.93010	±0.93010	-0.93131
DP780	1.01471	0.99936	0.99936	0.99936	±0.99281	±0.99281	±0.99281	1.01471
Mild Steel	0.85925	1.06171	1.06171	1.06171	±1.03530	±1.03530	±1.03530	0.85925
AA6XXX	1.13555	0.87893	0.87893	0.87893	±0.99253	±0.99253	±0.99253	1.13555
	α_1	α_2	α_3	α_4	α_5	α_6	α_7	α_8
Cu-1/4H	± 0.93010	±0.93010	0.80496	0.99449	0.99449	0.80496	±0.93010	1.18401
	± 0.93010	±0.93010	1.98897	0.40248	0.40248	1.98897	±0.93010	-1.18401
	± 0.93010	±0.93010	-1.98897	-0.40248	-0.40248	-1.98897	±0.93010	1.18401
	± 0.93010	±0.93010	-0.80496	-0.99449	-0.99449	-0.80496	±0.93010	-1.18401
DP780	0.99281	0.99281	1.02238	1.01087	1.01087	1.02238	0.99281	0.99936
Mild Steel	1.03530	1.03530	0.75802	0.90987	0.90987	0.75802	1.03530	1.06171
AA6XXX	0.99253	0.99253	1.26387	1.07140	1.07140	1.26387	0.99253	0.87893

identical polynomial coefficients as $(A_1, ..., A_5)$ of their Gotoh's yield function. The biaxial tensile yield surface given by case (h2) of Yld2000-2d is however shown in Fig.3.3 for sheet metal #1 as its polynomial coefficients $(\bar{A}_2, \bar{A}_3, \bar{A}_4, \bar{A}_5)$ are slightly different, see Table 3.3.

The directional dependence of yield stresses and plastic strain ratios under uniaxial tension as predicted by Gotoh's and some selected Yld2000-2d fourth-order yield functions of Table 3.3 are shown in Fig.3.4(a)-Fig.3.7(a) for these four sheet metals, respectively. Also shown in those four figures are the experimental results of uniaxial yield stresses (open squares) and plastic strain ratios (closed circles) as given in Table 3.1. As only on-axis experimental inputs $(\sigma_0, \sigma_{90}, R_0, R_{90})$ are used in their parameter identification, the predicted off-axis yield stresses and plastic strain ratios are usually not good. Results from cases (c) and (e) of Yld2000-2d are similar but not identical to those of Gotoh's polynomial yield functions with coefficients given per Eq.(3.17).

3.4.3 Yield Functions Based on Seven Experimental Inputs

Using seven experimental inputs $(\sigma_0, \sigma_{45}, \sigma_{90}, \sigma_b, R_0, R_{45}, R_{90})$ listed in Table 3.1, polynomial coefficients of Gotoh's yield function were computed directly from Eq.(3.27) and

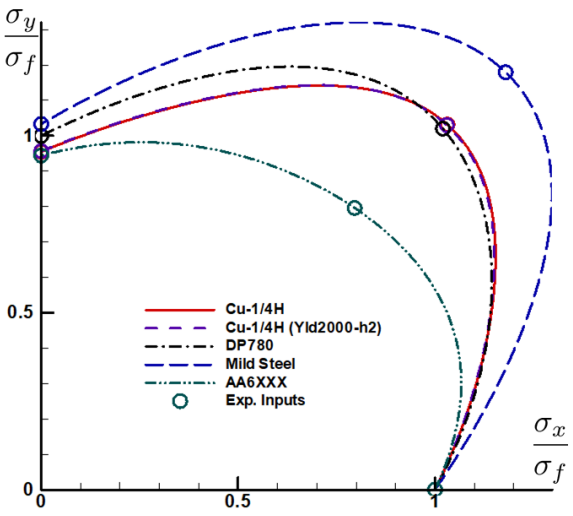

Figure 3.3: Biaxial tensile yield surfaces of four sheet metals calibrated with $(\sigma_0, \sigma_{90}, \sigma_b, R_0, R_{90})$.

Eq.(3.29). Results for the four sheet metals are listed in Table 3.4. Because the use of two additional inputs (σ_{45}, R_{45}), only the off-axis polynomial coefficients (A_6, A_7, A_8, A_9) in Table 3.4 are different from those in Table 3.3. Again, all calibrated Gotoh's yield functions of the four sheet metals listed in Table 3.4 were verified to be strictly positive and convex as per the sufficient condition of Eq.(3.19).

Material parameters $(\beta_1, ..., \beta_8)$ of Yld2000-2d were obtained for the selected four sheet metals using Eq.(3.20) first and then Eq.(3.30) for case (a) assuming $\beta_8 = \beta_1$ and Eq.(3.31) for case (b), respectively. Results including corresponding $(\alpha_1, ..., \alpha_8)$ and $(\bar{A}_2, ..., \bar{A}_9)$ are listed in Table 3.4 as well. Besides the six polynomial coefficients $(\bar{A}_1, ..., \bar{A}_5, \bar{A}_9)$ of both cases of Yld2000-2d are identical to those of Gotoh's yield function, $\bar{A}_7$ of case (b) Yld2000-2d is the same value of that of Gotoh's yield function.

The directional dependence of yield stresses and plastic strain ratios under uniaxial tension as predicted by Gotoh's and two Yld2000-2d fourth-order yield functions of Table 3.4 are shown in Fig.3.4(b)-Fig.3.7(b) for these four sheet metals, respectively. As two off-axis inputs (σ_{45}, R_{45}) are included in their parameter identification, the predicted off-axis yield stresses and plastic strain ratios are thus much improved. Results on σ_θ and R_θ from case (a)

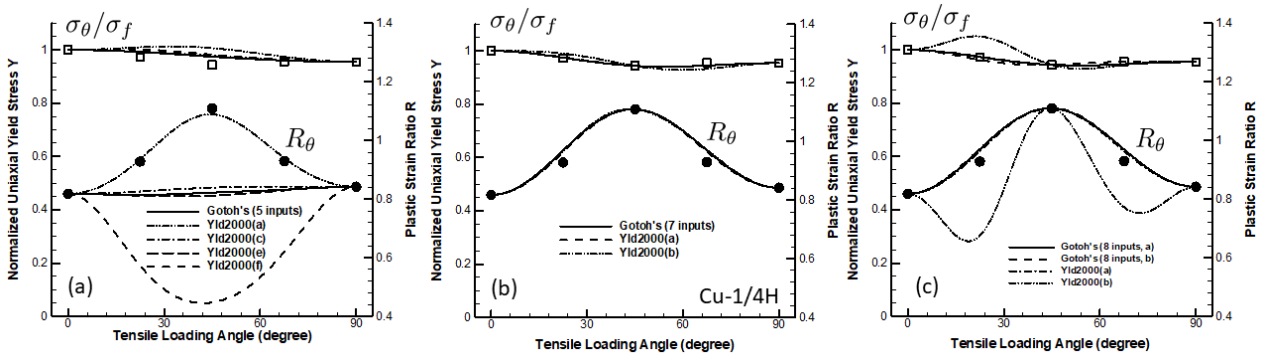

Figure 3.4: Directional dependence of uniaxial yield stresses and R-values of Cu-1/4H sheet predicted by various yield functions calibrated with: (a) $(\sigma_0, \sigma_{90}, \sigma_b, R_0, R_{90})$; (b) an addition of (σ_{45}, R_{45}) to (a); (c) an addition of either $\sigma_{22.5}$ or $\sigma_{67.5}$ to (b).

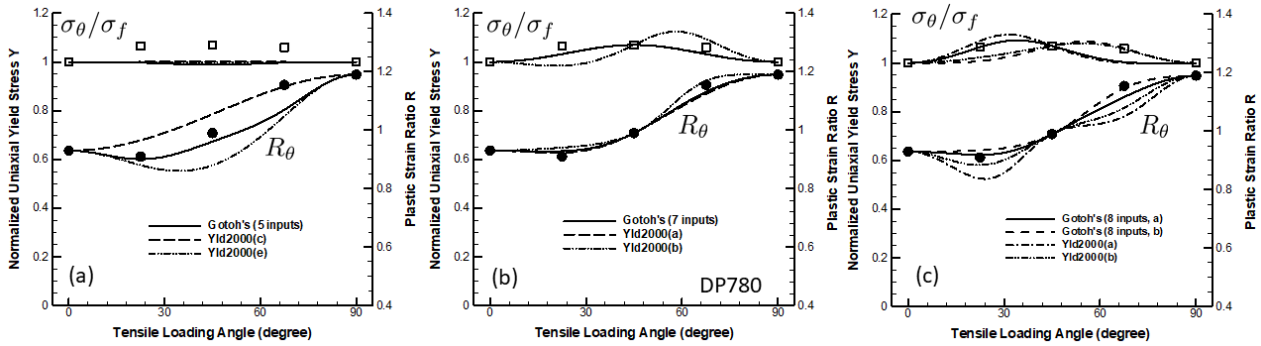

Figure 3.5: Directional dependence of uniaxial yield stresses and R-values of DP780 steel sheet predicted by various yield functions calibrated with: (a) $(\sigma_0, \sigma_{90}, \sigma_b, R_0, R_{90})$; (b) an addition of (σ_{45}, R_{45}) to (a); (c) an addition of either $\sigma_{22.5}$ or $\sigma_{67.5}$ to (b).

of Yld2000-2d are very close if not identical to those of Gotoh's polynomial yield functions for these four sheet metals. On the other hand, the predicted σ_θ and R_θ from case (b) of Yld2000-2d can be quite different especially for sheet metal #2 (DP780) shown in Fig.3.5(b) and for sheet metal #4 (AA6XXX) shown in Fig.3.7(b), respectively.

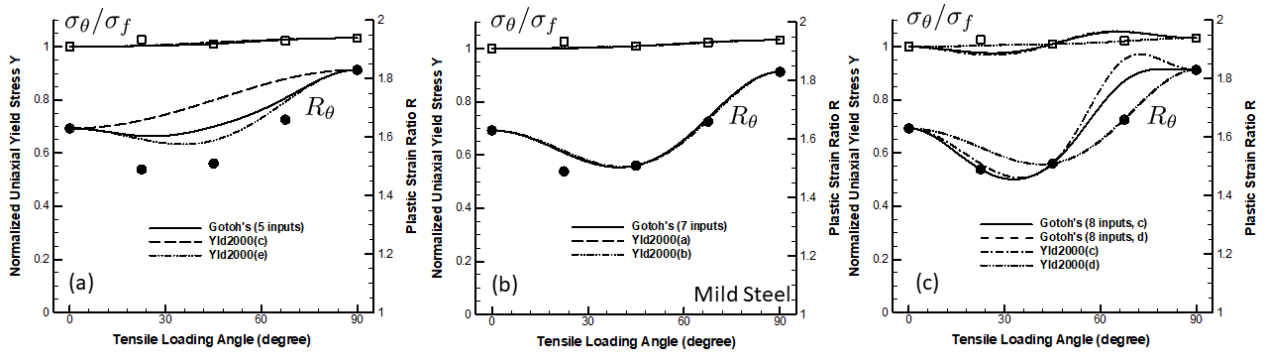

Figure 3.6: Directional dependence of uniaxial yield stresses and R-values of mild steel sheet predicted by various yield functions calibrated with: (a) $(\sigma_0, \sigma_{90}, \sigma_b, R_0, R_{90})$; (b) an addition of (σ_{45}, R_{45}) to (a); (c) an addition of either $R_{22.5}$ or $R_{67.5}$ to (b).

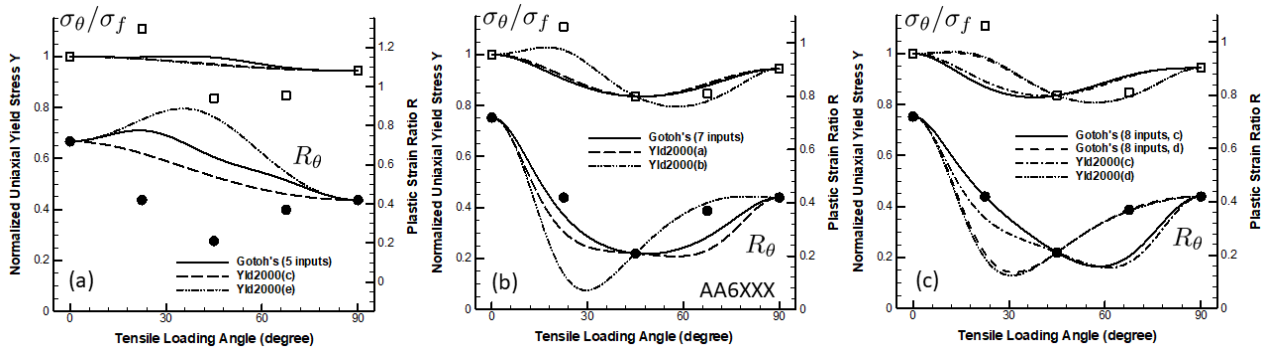

Figure 3.7: Directional dependence of uniaxial yield stresses and R-values of AA6XXX sheet predicted by various yield functions calibrated with: (a) $(\sigma_0, \sigma_{90}, \sigma_b, R_0, R_{90})$; (b) an addition of (σ_{45}, R_{45}) to (a); (c) an addition of either $R_{22.5}$ or $R_{67.5}$ to (b).

3.4.4 Yield Functions Based on Eight Independent Experimental Inputs

To realize the full modeling capabilities of a fourth-order Yld2000-2d yield function, one additional off-axis experimental input σ_θ or R_θ may be added for parameter identification. For Gotoh's polynomial yield function, the natural default choice of reduced anisotropy is to set the Fourier coefficient $F_4 = 0$, so the total number of independent coefficients is reduced from nine to eight [72]. In this study, four specific cases of adding one more off-axis input from Table 3.1 were considered: (a) σ_{225}; (b) σ_{675}; (c) R_{225}; and (d) R_{675}. For an illustrative

purpose, only results of cases (a) and (b) for sheet metals #1 (Cu-1/4H) and #2 (DP780) and results of cases (c) and (d) for sheet metals #3 (mild steel) and #4 (AA6XXX) are given in Table 3.5, respectively. In comparison with polynomial coefficients of Gotoh's yield function given in Table 3.4, only two off-axis polynomial coefficients A_6 and A_8 are different. The sufficient convexity condition Eq.(3.19) was used to verify that all calibrated Gotoh's yield functions of the four sheet metals listed in Table 3.5 are strictly positive and convex.

Using eight nonlinear equations of Eq.(3.33), material constants $(\beta_1, ..., \beta_8)$ of Yld2000-2d were subsequently obtained based on the polynomial coefficients of cases (a) to (d) of Gotoh's yield function listed in Table 3.5. Results including corresponding $(\alpha_1, ..., \alpha_8)$ and $(\bar{A}_2, ..., \bar{A}_9)$ are listed in Table 3.5 as well. Only two polynomial coefficients $\bar{A}_6$ and $\bar{A}_7$ from Yld2000-2d are different from those of corresponding Gotoh's yield function.

The directional dependence of yield stresses and plastic strain ratios under uniaxial tension as predicted by a pair of Gotoh's and Yld2000-2d fourth-order yield functions of Table 3.5 are shown in Fig.3.4(c)-Fig.3.7(c) for these four sheet metals, respectively. When an extra off-axis input σ_θ or R_θ is included in their parameter identification, the predicted off-axis yield stresses or plastic strain ratios are further enhanced. Results on σ_θ from cases (a) and (b) or on R_θ from cases (c) and (d) of Yld2000-2d follow more closely in general to those of corresponding Gotoh's polynomial yield functions for these four sheet metals. However, significant differences may remain in predicted R_θ for cases (a) and (b) and in predicted σ_θ for cases (c) and (d) between those two formulations of fourth-order yield functions.

3.5 Discussion and Conclusions

3.5.1 Fourth-order Yld2000-2d Is A Subset of Gotoh's Yield Functions

For the purpose of mathematical modeling of anisotropic plasticity of a sheet metal in plane stress, one may broadly classify homogeneous fourth-order polynomials of Eq.(3.1) into convex and non-convex types. Only convex ones are deemed to be used as valid Gotoh's yield functions. As shown in Fig.3.8, convex fourth-order homogeneous polynomials can be further classified as full or various reduced Gotoh's yield functions with nine or less independent polynomial coefficients as detailed by Tong [72].

The question about possible maximum number of independent material constants in a

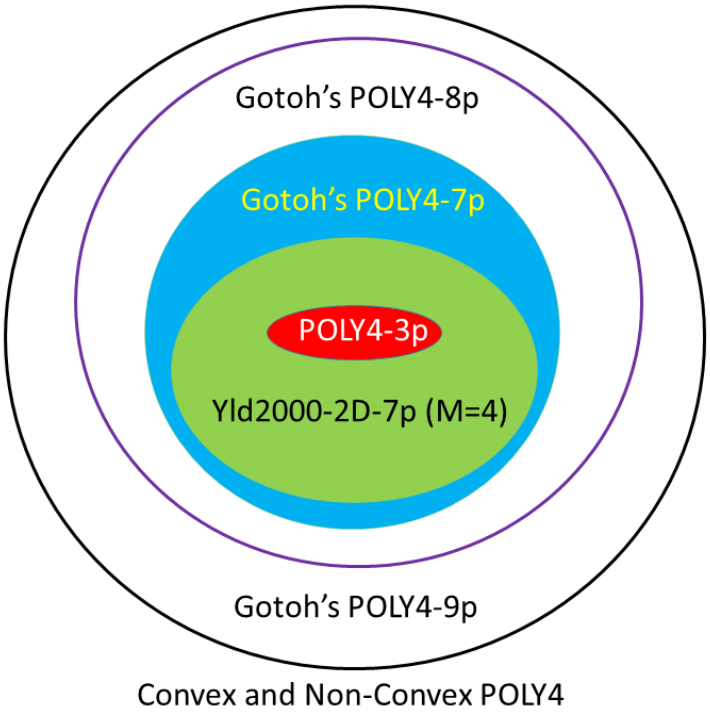

Figure 3.8: Schematic of full and various reduced Gotoh's yield functions with 9, 8, 7 and 3 independent polynomial coefficients. Fourth-order Yld2000-2d using standard inputs is only a subset of Gotoh's yield functions with 7 independent parameters.

3D orthotropic yield function Yld2004-18p was investigated in a recent study by Boogaard et al. [82] and it is found that inter-dependencies among its 18 material constants exist and two specific combinations of those material constants do not contribute to the value of yield function. Consequently, the number of independent material constants is 16 instead of 18 for 3D Yld2004. For the plane stress version of Yld2004, the number of independent material constants reduces from 14 to 12 as well. In the current common practice, a set of four yield stresses $(\sigma_0, \sigma_{45}, \sigma_{90}, \sigma_b)$ and four plastic strain ratios $(R_0, R_{45}, R_{90}, R_b)$ has been widely used as the standard inputs for calibrating a non-quadratic Yld2000-2d yield function with a stress exponent of $M > 2$ [40]. This has been assumed to be the case even when $M = 4$ [70]. However, these inputs do not constitute eight unique or independent inputs for a fourth-order yield function [72, 76, 77]. Standard fourth-order Yld2000-2d is thus only a subset of Gotoh's yield functions with seven independent polynomial coefficients (POLY4-7p). On the

other hand, it is shown in this study that fourth-order Yld2000-2d with eight independent material constants can still be obtained if one additional off-axis experimental input σ_θ or R_θ is used to replace R_b for its parameter identification. Nevertheless, the resulting Yld2000-2d is still a subset of Gotoh's yield functions with eight independent polynomial coefficients (POLY4-8p).

It is found that when modeling a sheet metal with in-plane isotropy, both Gotoh's and Yld2000-2d fourth-order yield functions are completely equivalent with three independent parameters (A_1, A_2, A_3) or $(\beta_1, \beta_2, \beta_5)$. The necessary and sufficient conditions as per Eq.(3.15) for a convex fourth-order polynomial of Eq.(3.9) would automatically ensure the existence of real-valued $(\beta_1, \beta_2, \beta_5)$ per Eq.(3.13) and thus a successful calibration of Yld2000-2d[2].

The fourth-order Yld2000-2d has another peculiar feature, that is, it has one *redundant* material constant in modeling a sheet metal under biaxial stress (i.e., $\tau_{xy} = 0$). The five polynomial coefficients $(\bar{A}_1, ..., \bar{A}_5)$ of Yld2000-2d are related to six material constants $(\beta_1, \beta_2, \beta_3, \beta_5, \beta_6, \beta_8)$ per Eq.(3.8). It can be shown that the necessary and sufficient conditions of Eq.(3.18) for a convex fourth-order polynomial $\Phi_g(\sigma_x, \sigma_y, 0)$ of Eq.(3.1) are met automatically if material constants $(\beta_1, \beta_2, \beta_3, \beta_5, \beta_6, \beta_8)$ are real-valued. Here, we show that for a biaxial fourth-order Yld2000-2d function ($\tau_{xy} = 0$), the requirement of *real-valued* material constants $(\beta_1, \beta_2, \beta_3, \beta_5, \beta_6, \beta_8)$ is not only a sufficient but also necessary convexity condition. That is, the polynomial coefficients $(\bar{A}_1, ..., \bar{A}_5)$ given in Eq.(3.8) in terms of $(\beta_1, \beta_2, \beta_3, \beta_5, \beta_6, \beta_8)$ meet the necessary and sufficient convexity conditions of Eq.(3.18). By some lengthy algebraic manipulations, one can show that each term as a polynomial in $(\bar{A}_1, ..., \bar{A}_5)$ can be factored as a sum of squares (SOS) in $(\beta_1, \beta_2, \beta_3, \beta_5, \beta_6, \beta_8)$ and thus to be non-negative, namely

$$\begin{aligned} &\frac{16}{3}(3\bar{A}_1 + \bar{A}_3 + 3\bar{A}_5) = 2(\beta_1\beta_2 - \beta_3\beta_8)^2 + 2(\beta_2\beta_3 - \beta_1\beta_8)^2 \\ &+ \beta_1^4 + \beta_2^4 + 6\beta_1^2\beta_3^2 + \beta_3^4 + 8\beta_5^4 + 16\beta_5^2\beta_6^2 + 8\beta_6^4 + 6\beta_2^2\beta_8^2 + \beta_8^4 \geq 0, \end{aligned} \tag{3.34}$$

[2]The requirement for real-valued material constants $(\alpha_1, ..., \alpha_8)$ or $(\beta_1, ..., \beta_8)$ upon the parameter identification of Yld2000-2d is only a sufficient condition for Yld2000-2d to be convex. Mathematically, it is not a necessary condition in general per the algebraic results of Eq.(3.13): i.e., an imaginary-valued β_5 is also acceptable here.

$$24\bar{A}_1\bar{A}_3 + 72\bar{A}_1\bar{A}_5 + 24\bar{A}_3\bar{A}_5 - 9\bar{A}_2^2 - 2\bar{A}_3^2 - 9\bar{A}_4^2 = \\ 3(8\bar{A}_1\bar{A}_3 - 3\bar{A}_2^2) + 3(8\bar{A}_3\bar{A}_5 - 3\bar{A}_4^2) + 2(36\bar{A}_1\bar{A}_5 - \bar{A}_3^2) \geq 0, \tag{3.35}$$

$$\frac{32}{27}(72\bar{A}_1\bar{A}_3\bar{A}_5 + 9\bar{A}_2\bar{A}_3\bar{A}_4 - 2\bar{A}_3^3 - 27\bar{A}_1\bar{A}_4^2 - 27\bar{A}_2^2\bar{A}_5) = (\beta_1\beta_2 + \beta_3\beta_8)^2 \\ (\beta_1\beta_5 + \beta_3\beta_5 - \beta_2\beta_6 + \beta_6\beta_8)^2(\beta_1\beta_5 - \beta_3\beta_5 + \beta_2\beta_6 + \beta_6\beta_8)^2 \geq 0, \tag{3.36}$$

where

$$\frac{16}{3}(8\bar{A}_1\bar{A}_3 - 3\bar{A}_2^2) = 8(\beta_3\beta_5^2\beta_8 - 2\beta_2\beta_5\beta_6\beta_8 - \beta_1\beta_2\beta_5^2)^2 \\ + 8(\beta_5\beta_6\beta_8^2 - \beta_2\beta_3\beta_5^2 + \beta_2^2\beta_5\beta_6 + \beta_1\beta_5^2\beta_8)^2 \\ + (-\beta_1\beta_2^3 + \beta_3\beta_8^3 - \beta_2^2\beta_3\beta_8 + \beta_1\beta_2\beta_8^2)^2 \geq 0, \tag{3.37}$$

$$\frac{16}{3}(8\bar{A}_3\bar{A}_5 - 3\bar{A}_4^2) = 8(-\beta_3\beta_6^2\beta_8 - 2\beta_1\beta_3\beta_5\beta_6 + \beta_1\beta_2\beta_6^2)^2 \\ + 8(-\beta_3^2\beta_5\beta_6 + \beta_2\beta_3\beta_6^2 - \beta_1\beta_6^2\beta_8 - \beta_1^2\beta_5\beta_6)^2 \\ + (-\beta_1^3\beta_2 + \beta_3^3\beta_8 + \beta_1\beta_2\beta_3^2 - \beta_1^2\beta_3\beta_8)^2 \geq 0, \tag{3.38}$$

$$\frac{16}{9}(36\bar{A}_1\bar{A}_5 - \bar{A}_3^2) = 8(\beta_2\beta_6^2\beta_8 + \beta_1\beta_3\beta_5^2)^2 \\ + 2(\beta_1^2\beta_5^2 + \beta_3^2\beta_5^2 - \beta_6^2\beta_8^2 - \beta_2^2\beta_6^2)^2 \\ + (-\beta_2\beta_3^2\beta_8 - \beta_1\beta_3\beta_8^2 - \beta_1\beta_2^2\beta_3 - \beta_1^2\beta_2\beta_8)^2 \geq 0. \tag{3.39}$$

On the other hand, it is not known at present if real-valued material constants $(\beta_1, \beta_2, \beta_3, \beta_5, \beta_6, \beta_8)$ can always be obtained using Eq.(3.20) if $(A_1, ..., A_5)$ satisfy the necessary and sufficient conditions of Eq.(3.18). Empirically, from the results obtained in this study with or without assuming $\beta_8 = \beta_1$, the answer seems to be affirmative. If it can be proved rigorously, then one can conclude that both Yld2000-2d and Gotoh's yield function may also be equivalent under biaxial stress.

3.5.2 On the Parameter Identification of Fourth-order Yld2000-2d

As the focus in this study is to compare the two formulations of fourth-order yield functions, parameter identification of material constants $(\beta_1, ..., \beta_8)$ of Yld2000-2d has been carried out almost exclusively by matching its corresponding polynomial coefficients $(\bar{A}_1, ..., \bar{A}_9)$ given by Eq.(3.8) with the polynomial coefficients $(A_1, ..., A_9)$ of Gotoh's yield function, which

are computed directly using linear algebraic relations based on three to eight experimental inputs. Polynomial coefficient matching has also been used by Sener et al. [73] and Uppaluri and Helm [74] for their parameter identification of the fourth-order yield function.

Three different approaches have been used for their polynomial coefficient matching of four sheet metals in this study: 1) a solution of up to eight nonlinear equations such as given by Eq.(3.33), 2) the least square minimization of differences between $(\bar{A}_1, ..., \bar{A}_9)$ and $(A_1, ..., A_9)$ such as given by either $\delta_{3a}(\beta_1, ...\beta_8)$ or $\delta_{3b}(\beta_1, ...\beta_8)$ of Eq.(3.26) with $\bar{A}_1 = A_1$, and 3) a mix or combination of previous two methods given by Eq.(3.20) and Eq.(3.22) for $\beta_8 = \beta_1$ or Eq.(3.25) without pre-imposing $\beta_8 = \beta_1$. Obviously, one can only match exactly at most eight polynomial coefficients of Yld2000-2d with those of Gotoh's yield function in general.

The least square minimization has recently been used by Uppaluri and Helm [74] to obtain eight material constants $(\beta_1, ..., \beta_8)$ of fourth-order Yld2000-2d using the following objective function[3]

$$\begin{aligned}\delta_{ud}(\beta_1, ...\beta_8) = &\sum_{k=1}^{5}[\bar{A}_k(\beta_1, ..., \beta_8) - A_k]^2 + [\bar{A}_9(\beta_1, ..., \beta_8) - A_9]^2 \\ &+ [\bar{A}_6(\beta_1, ..., \beta_8) + \bar{A}_7(\beta_1, ..., \beta_8) + \bar{A}_8(\beta_1, ..., \beta_8) - A_6 - A_7 - A_8]^2.\end{aligned} \tag{3.40}$$

It is observed that their objective function $\delta_{ud}(\beta_1, ...\beta_8)$ is a sum of only seven squared differences. In comparison, the objective functions $\delta_{3a}(\beta_1, ...\beta_8)$ or $\delta_{3b}(\beta_1, ...\beta_8)$ of Eq.(3.26) used in this study have a sum of either eight or nine squared differences (including the difference $\bar{A}_1 - A_1 = 0$ per the constraint condition!). Mathematically, they lead to under-, fully-, and over-constrained least square minimization problems where unique solutions of eight material constants $(\beta_1, ..., \beta_8)$ can only be obtained from the latter two cases (without counting the multiple equivalent variants due to nonlinear nature of problems). We have since verified numerically that indeed the results on eight material constants $(\beta_1, ..., \beta_8)$ of fourth-order Yld2000-2d given by Uppaluri and Helm [74] in their Table 3 for the six sheet metals is only one of *infinite* many possible solutions due to the under-constrained least

[3]It is called as an inverse approach by Uppaluri and Helm [74] and the objective function here is based on their Eq.(23) and Eq.(24) in Section 3.2 of their paper. It is note that their $(a_1, .., a_8)$ are the same as $(\beta_1, ..., \beta_8)$ used in this study.

square minimization: all solutions based on their objective function δ_{ud} will have the same $(\bar{A}_1, ..., \bar{A}_5, \bar{A}_6 + \bar{A}_7 + \bar{A}_8, \bar{A}_9)$ but individual values of $(\bar{A}_6, \bar{A}_7, \bar{A}_8)$ are not all the same.

Parameter identification of Yld2000-2d yield function has been more commonly based on either the Newton-Raphson numerical solution of eight nonlinear equations [20] or least square minimization of the objective function in terms of a sum of squared differences between predicted and measured yield stresses and plastic strain ratios [41]. If only the standard eight experimental inputs $(\sigma_0, \sigma_{45}, \sigma_{90}, \sigma_b, R_0, R_{45}, R_{90}, R_b)$ are used for such a least-square parameter identification of fourth-order Yld2000-2d, one would also have non-unique solutions as the problem is also under-constrained (i.e., σ_b and R_b are not two independent inputs here). This is an intrinsic non-uniqueness problem, different from the numerical non-unique solutions of nonlinear equations or the least-square minimization [73, 83].

3.5.3 On the Convexification of Non-convex Fourth-order Polynomials

It is well-known that the sufficient condition for a Yld2000-2d function to be convex is that all of its eight material constants are real-valued [20]. This essential mathematical attribute underscores the vast popularity of Yld2000-2d and other similarly formulated yield functions in advanced sheet metal forming analyses and simulations since 2000s [40,41,68,70]. On the other hand, the convexity of any polynomial yield function has to be certified upon calibration [65,66]. It is noted that the convexity of the vast majority of all calibrated Gotoh's yield functions initially appeared in the literature is simply assumed or implied but not rigorously certified [78], including those calibrated yield functions presented in the original work by Gotoh [36]. Nevertheless, it is shown that the certification of convexity of a calibrated Gotoh's yield function can be easily done either algebraically or numerically [67, 71, 79]. It turns out that almost all of reported Gotoh's yield functions for various FCC, BCC and HCP polycrystalline sheet metals in the literature are verified to be indeed convex by the new convexity certification.

Occasionally, the fourth-order polynomial function of Eq.(3.1) upon parameter identification is found to be actually non-convex. For example, Uppaluri and Helm [74] recently reported two non-convex fourth-order polynomials using the seven experimental inputs $(\sigma_0, \sigma_{45}, \sigma_{90}, \sigma_b, R_0, R_{45}, R_{90})$ for their parameter identification of one AA6016-T4 sheet and

one steel sheet (both were previously modeled by Tong and Alharbi [71]). A convexification adjustment of either polynomial coefficients or experimental inputs is thus needed before using them as valid Gotoh's yield functions in sheet metal forming analyses [71, 77]. By assuming that experimental inputs σ_{45} and R_{45} are more reliable, Uppaluri and Helm [74] reduced σ_b from measured $1.0069\sigma_0$ and $1.0\sigma_0$ to $0.99\sigma_0$ and $0.9\sigma_0$ for those two sheet metals respectively to obtain their convex fourth-order polynomial yield functions. The rationale for making such an adjustment is the new upper and lower bounds on the equal-biaxial tensile yield stress σ_b (equivalent to Eq.(18) presented by Uppaluri and Helm [74])

$$2(1+R_{45})(\frac{\sigma_{45}}{2})^4 \leq \sigma_b^4 \leq 2(1+R_{45})(9R_{45}+3\sqrt{9R_{45}^2+2R_{45}+1}+1)(\frac{\sigma_{45}}{2})^4 \tag{3.41}$$

While such an adjustment works out well for the two sheet metals under consideration, it is noted that the above bounds were derived from a *necessary* convexity condition originally given by Soare et al. [66]. For example, even with the newly adjusted σ_b as $0.99\sigma_0$ and $0.9\sigma_0$ for AA6016-T4 and steel sheets, the resulting fourth-order polynomial function would be still non-convex if the experimental input R_{90} happened to be 1.1 for AA6016-T4 and 0.8 for steel, respectively. That is, satisfying the new upper and lower bounds on the equal-biaxial tensile yield stress σ_b per Eq.(3.41) does not always lead in general to a convex fourth-order polynomial function. It is noted that the second case considered by Uppaluri and Helm [74] is a steel sheet very close to in-plane isotropy ($\sigma_{45} = 0.8\sigma_0$ instead of $\sigma_{45} = \sigma_0$). The necessary and sufficient convex condition in terms of σ_b, $R_0(= R_{45})$ and $\sigma_0(= \sigma_{45})$ per Eq.$(3.15)_3$ has been given by Tong [67] already for the case of in-plane isotropy. One can show that the upper and lower bound condition Eq.(3.41) with $R_{45} = R_0 = R_\theta$ is equivalent to Eq.$(3.15)_3$. That is, it is also a sufficient convex condition in this special case.

A better alternative convexification method for a non-convex Gotoh's polynomial function with reduced plastic anisotropy may be the use of fourth-order Yld2000-2d yield function. That is, depending on the number of independent experimental inputs used for parameter identification of $(A_1, ..., A_9)$, one can use the least-square minimization of the objective function given in Eq.(3.41) with $\beta_8 = \beta_1$ or the ones given in Eq.(3.26) to find the convex approximation in terms of $(\bar{A}_1, ..., \bar{A}_9)$ of a non-convex fourth-order polynomial function. For

the case of seven experimental inputs $(\sigma_0, \sigma_{45}, \sigma_{90}, \sigma_b, R_0, R_{45}, R_{90})$, this adjustment method was successfully applied to both AA6016-T4 and steel sheet metals [71, 74] using the least square minimization of $\delta_{ud}(\beta_1, ...\beta_7, \beta_8 = \beta_1)$ and the results are given in Table 3.6. It is noted that the added condition $\beta_8 = \beta_1$ make the resulting fourth-order Yld2000-2d unique. Original experimental inputs from Uppaluri and Helm [74] and the predicted yield stresses and plastic strain ratios by the convex Yld2000-2d fourth-order functions are listed in the table for comparison. Similarly, polynomial coefficients of two versions of convex Gotoh's yield functions are also listed for direct comparison. The minimum of the objective function δ_{ud} was found to be 0.000929 for AA6016-T4 and 0.102437 for steel, respectively. The much larger adjustment one has to make for the steel sheet indicates that a higher order non-quadratic yield function such as a sixth-order one may be better suited for modeling the steel sheet [84].

3.5.4 Conclusions

1. For an in-plane isotropic sheet metal, the fourth-order yield functions by Gotoh's polynomial and Yld2000-2d formulations are shown to be identical as their three independent material parameters are algebraically related and their convex domains are the same.

2. Fourth-order Yld2000-2d may fully match the capability of Gotoh's yield function for any on-axis biaxial loading $(\sigma_x, \sigma_y, \tau_{xy} = 0)$.

3. Fourth-order Yld2000-2d is not unique if the standard set of eight experimental inputs from three uniaxial tension tests and one equal biaxial tension test are used for its parameter identification.

4. A unique fourth-order Yld2000-2d may still be obtained if one additional condition or an extra experimental input from a second off-axis tension test is available for its calibration.

5. When five, seven or eight independent inputs are used for parameter identification of Gotoh's yield function with reduced plastic anisotropy, Yld2000-2d may be made to closely approximate each of the calibrated Gotoh's yield functions.

6. Yld2000-2d formulation may be used as an effective convexification method of a calibrated but non-convex fourth-order polynomial function with reduced plastic anisotropy.

7. It is advisable to always report the corresponding unique set of nine polynomial co-

efficients of four-order Yld2000-2d as its parameter identification generates many equivalent variations of its eight material constants.

Table 3.3: List of yield function parameters for four sheet metals with five inputs

Material	A_2	A_3	A_4	A_5	A_6	A_7	A_8	A_9
Cu-1/4H	-1.80000	2.68000	-2.20000	1.20300	6.00300	-4.85020	6.80900	8.88300
yld2000(a)					5.41996	-6.01335	6.28055	9.00000
(b)							6.79725	8.77003
(c)					5.97992	-5.00016	6.78592	
(d)					6.03254	-4.87513	6.83079	8.85768
(e)								8.78039
(f)					5.54571	-2.03119	6.58806	6.19634
(g)					6.03144	-4.87511	6.83205	8.85759
(h1)								8.78039
(h2)	-1.78297	2.66537	-2.18924	1.19569	6.01752	-4.86412	6.81972	8.87014
DP780	-1.92746	3.02482	-2.17352	1.00000	5.92746	-5.41246	6.17352	9.12580
yld2000(c)					5.92215	-6.16125	6.16820	
(e)								8.43346
Mild Steel	-2.47909	3.38817	-2.26980	0.87753	6.35662	-7.48720	5.90239	10.0146
yld2000(c)					6.35121	-7.78099	5.89698	
(e)								9.74124
AA6XXX	-1.67442	3.39540	-1.49045	1.25978	5.93420	-7.29297	6.26980	8.82005
yld2000(c)					5.92698	-5.45054	6.26258	
(e)								10.8530

	β_1	β_2	β_3	β_4	β_5	β_6	β_7	β_8
Cu-1/4H(a)	0.96935	1.16963	1.17065	1.00000	0.91193	1.02297	1.00000	0.96935
(b)				1.18408			0.96034	
(c)				1.17014			0.96745	
(d)				1.18692			0.96275	
(e)	1.01273	1.18815	1.16585	1.18727	0.93123	0.99951	0.95995	0.92562
(f)	1.08095	1.21327	1.15331	1.34031	0.96166	0.95977	0.78053	0.85501
(g)	0.97709	1.17307	1.16996	1.18738	0.91537	1.01889	0.96264	0.96161
(h1)	1.01275	1.18815	1.16585	1.18727	0.93124	0.99950	0.95995	0.92560
(h2)	1.24082	1.25119	1.09426	1.18925	1.02889	0.85452	0.96264	0.68193
DP780(c)	0.97767	1.05810	0.97364	1.01587	0.98110	1.02269	1.00189	0.97767
(e)	1.00790	1.07340	0.96884	1.08090	0.99078	1.01124	0.96952	0.94453
Mild Steel(c)	0.84776	1.02465	1.00851	1.01658	1.05348	1.00322	1.02835	0.84776
(e)	0.82608	1.01970	1.01562	1.05113	1.04741	1.00887	1.01588	0.86966
AA6XXX(c)	1.24685	0.76039	0.93774	0.84907	0.99545	1.02306	1.00926	1.24685
(e)	1.24673	0.76035	0.93782	0.72473	0.99542	1.02309	1.07231	1.24695

	α_1	α_2	α_3	α_4	α_5	α_6	α_7	α_8
Cu-1/4H(a)	0.80089	1.13401	0.86972	1.01993	1.01917	0.86819	1.00000	1.00000
(b)							0.96034	1.18408
(c)							0.96745	1.17014
(d)							0.96275	1.18692
(e)	0.86295	1.06779	0.82676	1.02366	1.01861	0.90377	0.95995	1.18727
(f)	0.96355	0.95788	0.75887	1.02757	1.01605	0.96178	0.78053	1.34031
(g)	0.81185	1.12241	0.86207	1.02066	1.01912	0.87447	0.96264	1.18738
(h1)	0.86298	1.06776	0.82675	1.02366	1.01860	0.90378	0.95995	1.18727
(h2)	1.20326	0.68015	0.59828	1.02523	1.00320	1.11312	0.96264	1.18925
DP780(c)	0.93951	1.06428	0.89523	0.95555	1.01889	1.02192	1.00189	1.01587
(e)	0.97032	1.03170	0.85950	0.95615	1.01873	1.04803	0.96952	1.08090
Mild Steel(c)	1.10374	0.95296	0.75125	0.88391	0.89602	0.77546	1.02835	1.01658
(e)	1.08595	0.97033	0.77081	0.88334	0.89730	0.75514	1.01588	1.05113
AA6XXX(c)	0.96784	1.05067	1.57876	1.21391	1.08090	1.31273	1.00926	0.84907
(e)	0.96775	1.05076	1.57888	1.21393	1.08088	1.31256	1.07231	0.72473

Table 3.4: List of yield function parameters for four sheet metals with seven inputs

Material	A_2	A_3	A_4	A_5	A_6	A_7	A_8	A_9
Cu-1/4H	-1.80000	2.68000	-2.20000	1.20300	6.63275	-6.29150	7.43875	11.4800
yld2000(a)					6.51322	-6.18961	7.45639	
(b)					5.84595		8.22555	
DP780	-1.92746	3.02482	-2.17352	1.00000	4.97904	-5.91800	5.22510	6.99634
yld2000(a)					4.94134	-5.83162	5.17643	
(b)					7.05928		3.14486	
Mild Steel	-2.47909	3.38817	-2.26980	0.87753	6.44243	-7.34336	5.98821	9.75941
yld2000(a)					6.42895	-7.32826	5.98660	
(b)					6.35691		6.07373	
AA6XXX	-1.67442	3.39540	-1.49045	1.25978	9.60763	2.55279	9.94323	8.17801
yld2000(a)					8.45210	4.71660	8.93495	
(b)					3.21979		16.3311	
	β_1	β_2	β_3	β_4	β_5	β_6	β_7	β_8
Cu-1/4H(a)	0.96935	1.16963	1.17065	1.17063	0.91193	1.02297	1.04669	0.96935
(b)	0.92399	1.99825	0.94950	1.69440	0.20458	1.13096	0.79759	0.04187
DP780(a)	0.97767	1.05810	0.97364	0.86361	0.98110	1.02269	0.94722	0.97767
(b)	0.51263	0.27589	1.80508	1.14711	1.13527	0.38558	0.90069	-1.19678
Mild Steel(a)	0.84776	1.02465	1.00851	1.08504	1.05348	1.00322	1.01147	0.84776
(b)	1.02712	1.06151	0.94265	1.08355	1.09819	0.94990	1.01170	0.65598
AA6XXX(a)	1.24685	0.76039	0.93774	1.53801	0.99545	1.02306	0.75377	1.24685
(b)	1.93079	1.11102	0.44239	1.67395	1.14400	0.69281	0.44939	0.32103
	α_1	α_2	α_3	α_4	α_5	α_6	α_7	α_8
Cu-1/4H(a)	0.80089	1.13401	0.86972	1.01993	1.01917	0.86819	1.04669	1.17063
(b)	-0.72180	2.05733	-1.01963	0.44765	1.01368	0.99455	0.79759	1.69440
DP780(a)	0.93951	1.06428	0.89521	0.95554	1.01889	1.02191	0.94722	0.86361
(b)	1.88496	-0.36411	-0.31381	0.79069	-0.78356	-1.75290	0.90069	1.14711
Mild Steel(a)	1.10374	0.95296	0.75125	0.88391	0.89602	0.77547	1.01147	1.08504
(b)	1.24648	0.80160	0.57935	0.88351	0.87986	0.94322	1.01170	1.08355
AA6XXX(a)	0.96785	1.05067	1.57876	1.21391	1.08090	1.31273	0.75377	1.53801
(b)	1.59520	0.24162	0.39660	0.98909	1.08812	2.20443	0.44939	1.67395

Table 3.5: List of yield function parameters for four sheet metals with eight inputs

Material	A_2	A_3	A_4	A_5	A_6	A_7	A_8	A_9
Cu-1/4H (a)	-1.80000	2.68000	-2.20000	1.20300	6.69445	-6.29150	7.37705	11.4800
yld2000(a)					6.57802	-6.17508		
Cu-1/4H (b)					7.24705	*-6.29150*	6.82445	*11.4800*
yld2000(b)					2.69595	-1.74040		
DP780 (a)	-1.92746	3.02482	-2.17352	1.00000	3.80101	-5.91800	6.40313	6.99634
yld2000(a)					2.85479	-4.97178		
DP780 (b)					5.98997	*-5.91800*	4.21417	*6.99634*
yld2000(b)					5.23802	-5.16606		
Mild Steel (c)	-2.47909	3.38817	-2.26980	0.87753	7.59858	-7.34336	4.83206	9.75941
yld2000(c)					8.02247	-7.76724		
Mild Steel (d)					6.29484	*-7.34336*	6.13580	*9.75941*
yld2000(d)					6.32091	-7.36942		
AA6XXX (c)	-1.67442	3.39540	-1.49045	1.25978	12.4349	2.55279	7.11598	8.17801
yld2000(c)					10.2872	4.70052		
AA6XXX (d)					4.94852	*2.55279*	14.6023	*8.17801*
yld2000(d)					4.60942	2.89190		
	β_1	β_2	β_3	β_4	β_5	β_6	β_7	β_8
Cu-1/4H(a)	1.07735	1.21208	1.15413	1.17609	0.96006	0.96195	1.04573	0.85879
(b)	0.90949	1.93091	1.33558	1.15509	-0.07019	0.95047	1.04935	0.30565
DP780(a)	1.06590	1.95323	0.55868	1.09853	0.36783	1.11768	0.91223	-0.23788
(b)	1.62650	1.25321	0.70075	0.83831	1.13900	0.58943	0.94951	0.08553
Mild Steel(c)	0.29837	0.77846	1.86448	1.55646	1.06243	0.32672	0.83508	-1.06735
(d)	1.12342	1.07833	0.90179	1.08399	1.11789	0.91584	1.01163	0.54425
AA6XXX(c)	0.92964	0.67824	1.11609	1.58808	0.89572	1.09255	0.69039	1.47024
(d)	1.84450	1.03923	0.52331	1.60889	1.13063	0.77704	0.65557	0.51106
	α_1	α_2	α_3	α_4	α_5	α_6	α_7	α_8
Cu-1/4H(a)	0.95817	0.96384	0.76245	1.02742	1.01624	0.95866	1.04573	1.17609
(b)	-1.09086	1.97114	-0.50273	0.71622	1.01176	0.69220	1.04935	1.15509
DP780(a)	-0.38201	1.86752	-1.37882	0.26452	0.98448	1.36489	0.91223	1.09853
(b)	1.68857	0.03986	-0.00405	0.87171	0.90081	1.59512	0.94951	0.83831
Mild Steel(c)	1.79813	-0.40898	-0.76438	0.61997	-0.53597	-1.71056	0.83508	1.55646
(d)	1.31994	0.71379	0.47853	0.87909	0.86670	1.03292	1.01163	1.08399
AA6XXX(c)	0.69889	1.28938	1.81487	1.22087	1.02763	0.88779	0.69039	1.58808
(d)	1.48422	0.42345	0.65574	1.05186	1.10544	2.09634	0.65557	1.60889

Table 3.6: Experimental inputs and model parameters for two additional sheet metals

Material	σ_0/σ_f	σ_{45}/σ_f	σ_{90}/σ_f	σ_b/σ_f	R_0	R_{45}	R_{90}	R_b
AA60616-T4[a]	1	0.9514	0.9375	1.0069	0.76	0.26	0.61	-
(from Yld2000)	1	0.9507	0.9351	0.9919	0.7471	0.2544	0.5929	1.4492
Steel[a]	1	0.8	1	1	0.38	0.38	0.38	-
(from Yld2000)	1	0.79676	0.96616	0.88417	0.30315	0.34313	0.25973	1.18664
	A_2	A_3	A_4	A_5	A_6	A_7	A_8	A_9
AA60616-T4[b]	-1.72727	2.36751	-1.96191	1.29454	6.31484	0.09962	7.13856	5.00255
$(\sigma_b = 0.99\sigma_0)^a$	-1.7273	2.4357	-1.9619	1.2945	6.2899	-0.0264	7.1532	5.0707
$(R_{90} = 1.1)^b$	-1.72727	3.18612	-2.71237	1.29454	6.31484	-0.78714	7.88901	5.07070
(from Yld2000)	-1.71049	2.38308	-1.94746	1.30796	4.90882	3.45305	5.18880	5.00573
Steel[b]	-1.10145	1.20290	-1.10145	1.00000	10.8671	4.57201	10.8671	11.7563
$(\sigma_b = 0.9\sigma_0)^a$	-1.1014	1.7271	-1.1014	1.0000	9.6014	6.0549	9.6014	12.2805
$(R_{90} = 0.8)^b$	-1.10145	2.40338	-1.77778	1.00000	10.8671	2.84737	11.5434	12.2805
(from Yld2000)	-0.93051	1.36564	-0.94647	1.14764	8.71745	8.60077	8.96779	11.7788
	β_1	β_2	β_3	β_4	β_5	β_6	β_7	β_8
AA60616-T4	1.00427	1.16493	1.26730	1.49577	0.88597	0.98766	0.04370	1.00427
Steel	1.12968	1.11838	1.18176	1.85257	0.79712	0.84558	0.02300	1.12968
	α_1	α_2	α_3	α_4	α_5	α_6	α_7	α_8
AA60616-T4	0.78429	1.08934	0.97512	1.09562	1.01884	0.82157	0.04370	1.49577
Steel	0.74866	0.89404	1.16702	1.15854	1.11101	1.07195	0.02300	1.85257

(a) From Table 2 of [74]; (b) Non-convex fourth-order polynomial functions.

Chapter 4

ON THE QUADRATIC YIELD CRITERION FOR FCC STAINLESS STEEL 304L SINGLE CRYSTALS

4.1 Introduction

It is well known that plasticity of metal crystals takes place at ambient conditions primarily due to collective motion of dislocations on certain crystallographic planes [30–32, 42, 85]. For engineering applications, the discrete nature of dislocation line segments and their discontinuous motions are not explicitly treated. Instead, plastic deformation of a single crystal due to such crystallographic slips has been treated as smooth (continuous) and homogeneous *simple shear* deformations occurring on activated slip systems [43, 44, 86]. That is, as a continuum element under homogeneous stress and plastic strain rate, a single crystal is assumed to flow uniformly through its crystallographic lattice. The elastic deformation of the lattice is often negligible for metals, the lattice is assumed to only undergoes rigid body rotation in most of investigations for simplicity.

There are two broadly different approaches in developing and formulating a phenomenological continuum plasticity theory for such single crystals: the macroscopic one and the micromechanical one. A macroscopic theory simply treats the single crystal as an anisotropic solid and models its plasticity following the classical mathematical theory of anisotropic plasticity [34–36], while a micromechanical theory of continuum crystal plasticity invokes explicitly the crystallographic slips as the physical mechanisms and processes that control yielding and dictate plastic flow in a single crystal [32, 85].

Both rate-independent and rate-dependent theories of (micromechanical) crystal plasticity have been well developed and widely used [87–89] while the mathematical anisotropic plasticity theory of single crystals has only occasionally been considered, mostly in the so-called continuum mechanics of textured polycrystals (CMTP) that aims to model the

texture-induced plastic anisotropy in polycrystals [90,91]. In CMTP, a macroscopic plastic potential (yield stress function) is used to approximate or curve-fit the micromechanically derived yield or flow surface of a single crystal. Most often the plastic potentials for cubic crystals are assumed to be of particular kinds of cubic symmetry [92,93].

In this study, we investigate the anisotropic hardening effects of crystallographic slips in crystal plasticity on the formulation of a macroscopic plastic potential of FCC cubic crystals and examine in some details the condition assumed for the plastic potential with some particular cubic symmetry types in the existing literature. To make the micro-to-macro transition mathematically rigorous, we consider only a class of multi-mechanism or multi-surface crystal plasticity models based on smooth and continuous plastic potentials [94–97]. As an initial effort focusing on FCC crystals, only quadratic plastic potentials will be considered in both crystal and macroscopic plasticity.

The continuum modeling of crystallographic slips is first discussed in Section 4.2, two formulations of quadratic plastic potentials for an FCC crystal per its cubic axes are detailed in Section 4.3. Sachs and Taylor polycrystal plastic potentials are presented in Section 4.4, parameter identifications of a quadratic macroscopic texture-induced plastic potential for FCC crystals are then described in Section 4.5. Modeling example applied to tensile tests on plastic SS304L single crystals with different loading directions is given, and some possible implications on continuum mechanics of textured polycrystals are discussed.

4.2 Continuum Modeling of Crystallographic Slips

A multi-slip model of the crystal plasticity is introduced [97]. In classical continuum plasticity, a stress-based plastic potential $\overline{\tau}_s(\boldsymbol{\sigma})$ is used to compute the plastic strain rate tensor $\dot{\varepsilon}^p$ via a flow rule

$$\dot{\varepsilon}^p = \dot{\overline{\gamma}}^p \frac{\partial \overline{\tau}_s}{\partial \boldsymbol{\sigma}}, \tag{4.1}$$

where the equivalent plastic strain rate $\dot{\overline{\gamma}}^p$ is given by a flow or yield condition

$$\begin{aligned} \overline{\tau}_s(\boldsymbol{\sigma}) &= \tau_f(\overline{\gamma}^p), \\ \overline{\tau}_s(\boldsymbol{\sigma}) &= \tau_{vf}(\overline{\gamma}^p, \dot{\overline{\gamma}}^p), \end{aligned} \tag{4.2}$$

where $\tau_f(\overline{\gamma}^p)$ is the equivalent plastic flow strength of a rate-independent material that is a function of only equivalent plastic strain $\overline{\gamma}^p$, and $\tau_{vf}(\overline{\gamma}^p, \dot{\overline{\gamma}}^p)$ is the equivalent viscoplastic flow strength of a rate-dependent material that is a function of both equivalent plastic strain rate $\dot{\overline{\gamma}}^p$ and equivalent plastic strain $\overline{\gamma}^p$. Additional internal state variables besides the isotropic hardening variable $\overline{\gamma}^p$ may also be incorporated to account for anisotropic hardening of the material.

To model crystallographic slips in crystal plasticity theory, the stress-based plastic slip potential is given in terms of *independent* resolved shear stresses

$$\tau^{(\alpha)} = \boldsymbol{\sigma}\boldsymbol{m}^{(\alpha)} \cdot \boldsymbol{s}^{(\alpha)}, \tag{4.3}$$

where $\boldsymbol{\sigma}$ is the applied Cauchy stress on all N possible slip systems $(\boldsymbol{m}^{(\alpha)}, \boldsymbol{s}^{(\alpha)})$ of a single crystal as $\overline{\tau}_s(\tau^{(1)}, \ldots, \tau^{(N)})$. Here, $\boldsymbol{m}^{(\alpha)}$ and $\boldsymbol{s}^{(\alpha)}$ are the normal vector and slip direction of α^{th} slip system where α =1,...,N. Individual crystallographic slip rate can thus be obtained via a slip rule

$$\dot{\tau}^{(\alpha)} = \dot{\overline{\gamma}}^p \frac{\partial \overline{\tau}_s}{\partial \tau^{(\alpha)}}. \tag{4.4}$$

Limited to the classical Schmid law, the crystallographic slip rate on each slip system is solely dependent on its resolved shear stress and a power-law is commonly assumed

$$\dot{\tau}^{(\alpha)} = \dot{\overline{\gamma}}^p \mathsf{sgn}(\tau^{(\alpha)}) |\frac{\tau^{(\alpha)}}{\tau_0^{(\alpha)}}|^{b-1}, \tag{4.5}$$

where the power exponent $b > 1$ and $\tau_0^{(\alpha)} > 0$ is the slip resistance of each system. Consequently, the slip rule and power-law above lead to the specific slip potential as (noting yield condition $\bar{\tau}_s = \tau_f$ or the flow condition $\bar{\tau}_s = \tau_{vf}$)

$$\overline{\tau}_s^b = \phi_b(\tau^{(1)}, \ldots \tau^{(N)}) = w_1|\tau^{(1)}|^b + w_2|\tau^{(2)}|^b + \ldots + w_N|\tau^{(N)}|^b = \sum_{\alpha=1}^{N} w_\alpha |\tau^{(\alpha)}|^b, \tag{4.6}$$

where $w_\alpha = (\frac{\tau_f}{\tau_0^{(\alpha)}})^{b-1} \geqslant 0$ or $w_\alpha = (\frac{\tau_{vf}}{\tau_0^{(\alpha)}})^{b-1} \geqslant 0$ is the slip system weight coefficient of the slip potential. One can verify that the power-law of Eq.(4.5) can indeed be obtained from the slip rule of Eq.(4.4) using the slip potential of Eq.(4.6).

In summary, a continuum plasticity model of crystallographic slips of a single crystal prescribes simply a slip potential $\phi_b(\tau^{(1)}, \ldots \tau^{(N)})$ in the form of a weighted sum of individual resolved shear stresses of b^{th} order ($b > 1$). The required inputs for the model include N -pairs of slip system vectors $(\boldsymbol{m}^{(\alpha)}, \boldsymbol{s}^{(\alpha)})$, the overall flow strength of the crystal τ_f (rate-independent cases) or τ_{vf} (rate-dependent cases), and the slip resistance $\tau_0^{(\alpha)}$ (or *alternatively* and *equivalently* the slip system weights w_α) of all N slip systems. Evolution laws on those *initial* inputs due to plastic spin and slip hardening upon subsequent plastic deformation of the crystal [97] are omitted for brevity as they are outside the main interest in the current study.

4.3 Quadratic Plastic Potentials of FCC Single Crystals

Following the classical anisotropic plasticity theory [34,35], one considers a continuum material element of a rolled sheet metal under an applied Cauchy stress $\boldsymbol{\sigma} = (\sigma_x, \sigma_y, \sigma_z, \tau_{xy}, \tau_{yz}, \tau_{zx})$, where the Cartesian coordinate xyz-axes are chosen by convention to be the rolling (RD), transverse (TD) and normal (ND) directions of the sheet metal. A plastic potential (also as a yield stress function) is used to describe pressure insensitive yielding, incompressible plastic flow, and centro-symmetric tension and compression respsonses (i.e., Bauchinger effects due to the load reversal is not considered here). Consequently, the plastic potential will be a homogeneous function of only five independent stress components such as $\boldsymbol{\sigma}_d = (\sigma_x - \sigma_z, \sigma_y - \sigma_z, \tau_{xy}, \tau_{yz}, \tau_{zx})$. The yield stress function in a general quadratic theory of macroscopic anisotropic plasticity is a homogeneous polynomial of second order in the following form (setting $\sigma_z = 0$ for simplicity)

$$\begin{aligned}
\Phi_2(\boldsymbol{\sigma}_d) &= f^2(\boldsymbol{\sigma}) \\
&= A_1\sigma_x^2 + A_2\sigma_x\sigma_y + A_3\sigma_y^2 + A_4\tau_{xy}^2 + A_5\tau_{yz}^2 + A_6\tau_{zx}^2 \\
&+ A_7\sigma_x\tau_{xy} + A_8\sigma_y\tau_{xy} + A_9\tau_{yz}\tau_{zx} + A_{10}\sigma_x\tau_{yz} + A_{11}\sigma_y\tau_{yz} \\
&+ A_{12}\tau_{xy}\tau_{yz} + A_{13}\sigma_x\tau_{zx} + A_{14}\sigma_y\tau_{zx} + A_{15}\tau_{xy}\tau_{zx},
\end{aligned} \tag{4.7}$$

where $(A_1, ..., A_{15})$ are the 15 independent polynomial coefficients (material constants) of the yield stress function (YLD), and $f(\boldsymbol{\sigma}_d) = \sigma_f$ defines the yield condition (surface) where σ_f is the current equivalent flow strength of the material. In this section, the anisotropic quadratic

yield functions for FCC single crystal with different plastic anisotropy will be presented.

4.3.1 Two Formulations of Plastic Potential for an FCC Single Crystal

When being applied to cubic single crystals (the *xyz*-axes coincide with the *123*-axes), their quadratic plastic potential of Eq.(4.7) may be rewritten with respect to their cubic *123*-axes as (setting $\sigma_{33} = 0$ for simplicity as well)

$$\begin{aligned}\Phi_2(\boldsymbol{\sigma}_d^*) = {} & a_1\sigma_{11}^2 + a_2\sigma_{11}\sigma_{22} + a_3\sigma_{22}^2 + a_4\tau_{12}^2 + a_5\tau_{23}^2 + a_6\tau_{31}^2 \\ & + a_7\sigma_{11}\tau_{12} + a_8\sigma_{22}\tau_{12} + a_9\tau_{23}\tau_{31} + a_{10}\sigma_{11}\tau_{23} + a_{11}\sigma_{22}\tau_{23} \\ & + a_{12}\tau_{12}\tau_{23} + a_{13}\sigma_{11}\tau_{31} + a_{14}\sigma_{22}\tau_{31} + a_{15}\tau_{12}\tau_{31},\end{aligned} \tag{4.8}$$

where $(a_1, ..., a_{15})$ are the corresponding 15 material constants, and the applied Cauchy stress and its reduced form are now given in terms of *123*-components as $\boldsymbol{\sigma}^* = (\sigma_{11}, \sigma_{22}, \sigma_{33}, \tau_{12}, \tau_{23}, \tau_{31})$ and $\boldsymbol{\sigma}_d^* = (\sigma_{11} - \sigma_{33}, \sigma_{22} - \sigma_{33}, \tau_{12}, \tau_{23}, \tau_{31})$.

On the other hand, the quadratic plastic potential of an FCC single crystal may be directly associated with its crystallographic slips in a micromechanical multi-surface plasticity theory as a weighted sum of squared independent resolved shear stresses shown in Eq.(4.6) with $b = 2$

$$\begin{aligned}\Phi_{2fcc}(\tau^{(1)}, \ldots, \tau^{(12)}) = {} & w_1|\tau^{(1)}|^2 + w_2|\tau^{(2)}|^2 + w_3|\tau^{(3)}|^2 + w_4|\tau^{(4)}|^2 \\ & + w_5|\tau^{(5)}|^2 + w_6|\tau^{(6)}|^2 + w_7|\tau^{(7)}|^2 + w_8|\tau^{(8)}|^2 \\ & + w_9|\tau^{(9)}|^2 + w_{10}|\tau^{(10)}|^2 + w_{11}|\tau^{(11)}|^2 + w_{12}|\tau^{(12)}|^2,\end{aligned} \tag{4.9}$$

where $(\tau^{(1)}, ..., \tau^{(12)})$ are resolved shear stresses, $(w_1, ..., w_{12})$ are non-negative weights related to the relative slip resistance of twelve slip systems in the FCC crystal, and $\sqrt{\phi_{2fcc}} = \tau_f$ defines the slip condition of the single crystal.

4.3.2 Relationships between Polynomial Coefficients and Slip System Weights

As the individual resolved shear stress on α^{th} slip system of the FCC crystal can be directly computed via $\tau^{(\alpha)} = \boldsymbol{\sigma}^* \mathbf{m}^{(\alpha)} \cdot \mathbf{s}^{(\alpha)}$, the quadratic yield stress function of an FCC

single crystal ϕ_{2fcc} of Eq.(4.9) are given explicitly in terms of Cauchy stress components as

$$\begin{aligned}\Phi_{2fcc}(\tau^{(1)},\ldots,\tau^{(12)}) &= \sum_{\alpha=1}^{12} w_\alpha |\tau^{(\alpha)}|^2 \\ &= \sum_{\alpha=1}^{12} w_\alpha |\boldsymbol{\sigma}^* \boldsymbol{m}^{(\alpha)} \cdot \boldsymbol{s}^{(\alpha)}|^2 = \Phi_{2fcc}(\boldsymbol{\sigma}^*),\end{aligned} \tag{4.10}$$

where $(\mathbf{m}^{(\alpha)}, \mathbf{s}^{(\alpha)})$ are the unit slip plane normal and slip direction of the twelve slip systems as shown in Table 4.1 (including the corresponding resolved shear stresses). The names for incremental slips are similar but slightly different from those originally used by Bishop and Hill [85].

Table 4.1: Slip systems in FCC crystals

number α	incremental slip	normal $\mathbf{m}^{(\alpha)}$	direction $\mathbf{s}^{(\alpha)}$	resolved shear stress $\sqrt{6}\tau^{(\alpha)}$
1	$\dot{\gamma}_{a1}$		$[01\bar{1}]$	$\sigma_{22}-\sigma_{33}+\tau_{12}-\tau_{31}$
2	$\dot{\gamma}_{a2}$	(111)	$[\bar{1}01]$	$\sigma_{33}-\sigma_{11}-\tau_{12}+\tau_{23}$
3	$\dot{\gamma}_{a3}$		$[1\bar{1}0]$	$\sigma_{11}-\sigma_{22}+\tau_{13}-\tau_{23}$
4	$\dot{\gamma}_{b1}$		$[0\bar{1}\bar{1}]$	$\sigma_{22}-\sigma_{33}+\tau_{12}+\tau_{31}$
5	$\dot{\gamma}_{b2}$	$(\bar{1}\bar{1}1)$	$[101]$	$\sigma_{33}-\sigma_{11}-\tau_{12}-\tau_{23}$
6	$\dot{\gamma}_{b3}$		$[\bar{1}10]$	$\sigma_{11}-\sigma_{22}-\tau_{13}+\tau_{23}$
7	$\dot{\gamma}_{c1}$		$[01\bar{1}]$	$\sigma_{22}-\sigma_{33}-\tau_{12}+\tau_{13}$
8	$\dot{\gamma}_{c2}$	$(\bar{1}11)$	$[101]$	$\sigma_{33}-\sigma_{11}+\tau_{12}+\tau_{23}$
9	$\dot{\gamma}_{c3}$		$[\bar{1}\bar{1}0]$	$\sigma_{11}-\sigma_{22}-\tau_{13}-\tau_{23}$
10	$\dot{\gamma}_{d1}$		$[0\bar{1}\bar{1}]$	$\sigma_{22}-\sigma_{33}-\tau_{12}-\tau_{13}$
11	$\dot{\gamma}_{d2}$	$(1\bar{1}1)$	$[\bar{1}01]$	$\sigma_{33}-\sigma_{11}+\tau_{12}-\tau_{23}$
12	$\dot{\gamma}_{d3}$		$[110]$	$\sigma_{11}-\sigma_{22}+\tau_{13}+\tau_{23}$

Obviously, macroscopic and microscopic plastic potentials $\phi_2(\boldsymbol{\sigma}^*)$ and $\phi_{2fcc}(\boldsymbol{\sigma}^*)$ are regarded to be equivalent here. By comparing directly the individual second-order Cauchy stress terms in both potentials ϕ_2 in Eq.(4.8) and ϕ_{2fcc} in Eq.(4.10), one has the fifteen

polynomial coefficients $(a_1, ..., a_{15})$ in terms of twelves slip system weights $(w_1, ..., w_{12})$ as

$$
\begin{aligned}
a_1 &= a_5 = \frac{w_2 + w_3 + w_5 + w_6 + w_8 + w_9 + w_{11} + w_{12}}{6}, \\
a_2 &= -\frac{w_3 + w_6 + w_9 + w_{12}}{3}, \quad a_7 = \frac{w_2 + w_5 - w_8 - w_{11}}{3}, \\
a_3 &= a_6 = \frac{w_1 + w_3 + w_4 + w_6 + w_7 + w_9 + w_{10} + w_{12}}{6}, \\
a_4 &= a_1 + a_2 + a_3 = \frac{w_1 + w_2 + w_4 + w_5 + +w_7 + w_8 + w_{10} + w_{11}}{6}, \\
a_8 &= \frac{w_1 + w_4 - w_7 + w_{10}}{3}, \quad a_9 = -\frac{w_3 + w_6 - w_9 - w_{12}}{3}, \\
a_{10} &= -\frac{w_2 + w_3 - w_5 - w_6 + w_8 + w_9 - w_{11} - w_{12}}{3}, \\
a_{11} &= \frac{w_3 - w_6 + w_9 - w_{12}}{3}, \quad a_{12} = -\frac{w_2 - w_5 - w_8 + w_{11}}{3}, \\
a_{13} &= \frac{w_3 - w_6 - w_9 + w_{12}}{3}, \quad a_{15} = -\frac{w_1 - w_4 + w_7 - w_{10}}{3}, \\
a_{14} &= -\frac{w_1 + w_3 - w_4 - w_6 - w_7 - w_9 + w_{10} + w_{12}}{3}.
\end{aligned}
\tag{4.11}
$$

That is, only up to twelve polynomial coefficients $(a_1, a_2, a_3, a_7, ..., a_{15})$ are independent in the quadratic plastic potential of an FCC crystal as $a_4 = a_1 + a_2 + a_3$, $a_5 = a_1$, and $a_6 = a_3$.

4.3.3 FCC Crystals with Reduced Plastic Anisotropy

The number of *independent* polynomial coefficients of $\phi_2(\boldsymbol{\sigma}^*)$ and slip system weight coefficient of quadratic plastic potential $\phi_{2fcc}(\boldsymbol{\sigma}^*)$ may be further reduced if plastic anisotropy of FCC crystals is of a lesser degree (i.e., having a higher order of symmetry).

For the case of monoclinic anisotropy with its symmetric plane defined by 3-axis, six polynomial coefficients $(a_{10}, ..., a_{15})$ associated with linear Cauchy stresses terms of only either τ_{23} or τ_{31} shall be zero. For the case of orthotropic anisotropy with its symmetric axes defined by the cubic 123-axes, three polynomial coefficients (a_7, a_8, a_9) associated with the remaining linear Cauchy stresses terms of either τ_{12} or τ_{23} shall be zero. Three additional cases of further reduced plastic anisotropy can also be considered: in-plane axially isotropy with $a_3 = a_1$, in-plane isotropy with $a_2 = 0$, and finally the cubic anisotropy with $a_2 = -a_1$. By using the twelve linear relationships between the polynomial coefficients and crystallographic slip system weights given in Eq.(4.11), it turns out that the reduce plastic anisotropy leads to various conditions imposed on the crystallographic slip system weights. The results

are summarized in the following five cases of reduced plastic anisotropy

$$
\begin{aligned}
&1)\ \underline{\text{monoclinic anisotropy}}\ (\text{six material constants}):\\
&\phi_{2m} = a_1\sigma_{11}^2 + a_2\sigma_{11}\sigma_{22} + a_3\sigma_{22}^2 + (a_1+a_2+a_3)\tau_{12}^2 + a_1\tau_{23}^2 + a_3\tau_{31}^2\\
&\qquad + a_7\sigma_{11}\tau_{12} + a_8\sigma_{22}\tau_{12} + a_9\tau_{23}\tau_{31},\\
&w_1 = w_4,\ \ w_2 = w_5,\ \ w_3 = w_6,\ \ w_7 = w_{10},\ \ w_8 = w_{11},\ \ w_9 = w_{12}.\\
&2)\ \underline{\text{orthotropic anisotropy}}\ (\text{three material constants}):\\
&\phi_{2o} = a_1\sigma_{11}^2 + a_2\sigma_{11}\sigma_{22} + a_3\sigma_{22}^2 + (a_1+a_2+a_3)\tau_{12}^2 + a_1\tau_{23}^2 + a_3\tau_{31}^2,\\
&w_1 = w_4 = w_7 = w_{10},\ \ w_2 = w_5 = w_8 = w_{11},\ \ w_3 = w_6 = w_9 = w_{12}.\\
&3)\ \underline{\text{in-plane axial isotropy}}\ (\text{two material constants}):\\
&\phi_{2ia} = a_1\sigma_{11}^2 + a_2\sigma_{11}\sigma_{22} + a_1\sigma_{22}^2 + (2a_1+a_2)\tau_{12}^2 + a_1\tau_{23}^2 + a_1\tau_{31}^2,\\
&w_1 = w_4 = w_7 = w_{10} = w_2 = w_5 = w_8 = w_{11},\ \ w_3 = w_6 = w_9 = w_{12}.\\
&4)\ \underline{\text{in-plane isotropy}}\ (\text{one material constant}):\\
&\phi_{2ip} = a_1(\sigma_{11}^2 + \sigma_{22}^2 + 2\tau_{12}^2 + \tau_{23}^2 + \tau_{31}^2),\\
&w_1 = w_4 = w_7 = w_{10} = w_2 = w_5 = w_8 = w_{11},\ w_3 = w_6 = w_9 = w_{12} = 0.\\
&5)\ \underline{\text{cubic anisotropy}}\ (\text{one material constant}):\\
&\phi_{2c} = a_1(\sigma_{11}^2 - \sigma_{11}\sigma_{22} + \sigma_{22}^2 + \tau_{12}^2 + \tau_{23}^2 + \tau_{31}^2),\\
&w_1 = w_4 = w_7 = w_{10} = w_2 = w_5 = w_8 = w_{11} = w_3 = w_6 = w_9 = w_{12}.
\end{aligned}
\tag{4.12}
$$

4.3.4 Texture Component of Orthotropic FCC Metals

Next we consider the quadratic plastic potential $\phi_2(\boldsymbol{\sigma}_d)$ of some disoriented FCC single crystals as representative texture components commonly found in a rolled and/or annealed polycrystal sheet [92, 98, 99]. Per convention, an ideal texture component (or a disoriented crystal) is specified in terms of Miller indices for both ND and RD (z-axis and x-axis) of a polycrystalline sheet metal as $\{hkl\}\langle uvw\rangle$. Limited only to the case of orthotropic polycrystal sheets with xyz-axes, each texture component consists in general a quartet or four variants of $(hkl)[uvw]$, $(\bar{h}\bar{k}\bar{l})[uvw]$, $(hkl)[\bar{u}\bar{v}\bar{w}]$, and $(\bar{h}\bar{k}\bar{l})[\bar{u}\bar{v}\bar{w}]$. The quadratic plastic potential $\phi_2(\boldsymbol{\sigma}_d)$ of one disoriented FCC crystal is a sum of quadratic plastic potentials

$\phi_{2fcc}(\boldsymbol{\sigma}_d^*)$ of its four variants

$$\begin{aligned}\Phi_{2o}(\boldsymbol{\sigma}_d) &= \frac{1}{4}[\Phi_{2fcc}^{(i)}(\boldsymbol{\sigma}_d^*) + \Phi_{2fcc}^{(ii)}(\boldsymbol{\sigma}_d^*) + \Phi_{2fcc}^{(iii)}(\boldsymbol{\sigma}_d^*) + \Phi_{2fcc}^{(iv)}(\boldsymbol{\sigma}_d^*)] \\ &= A_1\sigma_x^2 + A_2\sigma_x\sigma_y + A_3\sigma_y^2 + A_4\tau_{xy}^2 + A_5\tau_{yz}^2 + A_6\tau_{zx}^2,\end{aligned} \tag{4.13}$$

where $\boldsymbol{\sigma}^* = \mathbf{Q}\boldsymbol{\sigma}\mathbf{Q}^T$, $\mathbf{Q} = (\mathbf{e}'_{RD}, \mathbf{e}'_{TD}, \mathbf{e}'_{ND})$ is the coordinate transformation matrix given in terms of unit vectors (in the column form) of RD, TD and ND axes of the polycrystal sheet metal expressed in the *123*-axes of a cubic single crystal. That is

$$\mathbf{e}'_{RD} = \frac{(u,v,w)^T}{\sqrt{u^2+v^2+w^2}}, \quad \mathbf{e}'_{ND} = \frac{(h,k,l)^T}{\sqrt{h^2+k^2+l^2}}, \quad \mathbf{e}'_{TD} = \mathbf{e}'_{ND} \times \mathbf{e}'_{RD}. \tag{4.14}$$

Besides Miller indices, there is another form called Euler angles (ϕ_1, Φ, ϕ_2) to indicate the representation of an disorientate crystal, which presents the rotating angles transferred from the specimen coordinate system to the crystallographic coordinate system [100–102]. In the following, the Euler angle in Bunge convention is employed to define texture data of a single crystal. That is, ϕ_1 is the rotated angle about the ND axis of the specimen coordinate system ,Φ is the angle rotating about new RD axis of the rotated coordinate system, and ϕ_2 tells the rotation of the ND axis of the crystallographic coordinate system. The relationships between Miller indices and Euler angles in Bunge convention are

$$\begin{aligned}\cos\Phi &= \frac{l}{\sqrt{h^2+k^2+l^2}}, \quad \cos\phi_2 = \frac{k}{\sqrt{h^2+k^2}}, \\ \cos\phi_1 &= \frac{w}{\sqrt{u^2+v^2+w^2}}\frac{\sqrt{h^2+k^2}}{\sqrt{h^2+k^2+l^2}},\end{aligned} \tag{4.15}$$

where $\phi_1 \in [0, 2\pi]$,$\Phi \in [0, \pi]$, and $\phi_2 \in [0, 2\pi]$. The rotation matrix expressed by three Bunge Euler angles from the coordinate system of specimen to the coordinate system of crystal is shown

$$\mathbf{Q} = \begin{bmatrix} \cos\phi_2 & \sin\phi_2 & 0 \\ -\sin\phi_2 & \cos\phi_2 & 0 \\ 0 & 0 & 1 \end{bmatrix} \begin{bmatrix} 1 & 0 & 0 \\ 0 & \cos\Phi & \sin\Phi \\ 0 & -\sin\Phi & \cos\Phi \end{bmatrix} \begin{bmatrix} \cos\phi_1 & \sin\phi_1 & 0 \\ -\sin\phi_1 & \cos\phi_1 & 0 \\ 0 & 0 & 1 \end{bmatrix}. \tag{4.16}$$

4.3.5 Generation of Grain Orientations in Polycrystals

Besides the Miller index for ideal texture components, the Rodriguez crystal orientation angles (θ, ψ, ω) may be used to define the arbitrary orientation of a single crystal in the polycrystal reference frame. The Rodriguez formula for the rotated cubic axes in Fig.4.1 are expressed in terms of the crystal orientation angles (θ, ψ, ω) via

$$d_1 = \sin\theta\cos\psi, \quad d_2 = \sin\theta\sin\psi, \quad d_3 = \cos\theta, \quad c = \cos\omega, \quad s = \sin\omega, \tag{4.17}$$

and the coordinate transformation matrix will then be given by Bunge [103]

$$\mathbf{Q} = \begin{pmatrix} (1-d_1^2)c + d_1^2 & d_1d_2(1-c) + d_3s & d_1d_3(1-c) - d_2s \\ d_1d_2(1-c) - d_3s & (1-d_2^2)c + d_2^2 & d_2d_3(1-c) + d_1s \\ d_1d_3(1-c) + d_2s & d_2d_3(1-c) - d_1s & (1-d_3^2)c + d_3^2 \end{pmatrix}. \tag{4.18}$$

To ensure the strict plastic orthotropy, the four orthotropic variants for each orientation of a single crystal should be included in the calculations.

4.4 Sachs and Taylor Quadratic Plastic Potentials of Polycrystals

4.4.1 Dual Quadratic Plastic Potentials for FCC Single and Polycrystals

Under strict convexity and normality conditions in associated plasticity [104, 105], it is shown that quadratic yield stress function $\Phi_2(\boldsymbol{\sigma}_d)$ and plastic strain rate function $\Psi_2(\dot{\boldsymbol{\varepsilon}}_d)$ are constitutive dual plastic potentials, where (per plastic incompressibility)

$$\begin{aligned} \Psi_2(\dot{\boldsymbol{\varepsilon}}_d) = & q^2(\dot{\boldsymbol{\varepsilon}}_d) = B_1\dot{\varepsilon}_x^2 + B_2\dot{\varepsilon}_x\dot{\varepsilon}_y + B_3\dot{\varepsilon}_y^2 + B_4\dot{\gamma}_{xy}^2 + B_5\dot{\gamma}_{yz}^2 + B_6\dot{\gamma}_{zx}^2 \\ & + B_7\dot{\varepsilon}_x\dot{\gamma}_{xy} + B_8\dot{\varepsilon}_y\dot{\gamma}_{xy} + B_9\dot{\gamma}_{yz}\dot{\gamma}_{zx} + B_{10}\dot{\varepsilon}_x\dot{\gamma}_{yz} + B_{11}\dot{\varepsilon}_y\dot{\gamma}_{yz} \\ & + B_{12}\dot{\gamma}_{xy}\dot{\gamma}_{yz} + B_{13}\dot{\varepsilon}_x\dot{\gamma}_{zx} + B_{14}\dot{\varepsilon}_y\dot{\gamma}_{zx} + B_{15}\dot{\gamma}_{xy}\dot{\gamma}_{zx}, \end{aligned} \tag{4.19}$$

where $(B_1, ..., B_{15})$ are the 15 independent polynomial coefficients (material constants) of quadratic strain rate function (SRP), $\dot{\boldsymbol{\varepsilon}}_d = (\dot{\varepsilon}_x, \dot{\varepsilon}_y, \dot{\gamma}_{xy}, \dot{\gamma}_{yz}, \dot{\gamma}_{zx})$ and $q(\dot{\boldsymbol{\varepsilon}}_d) = \dot{\bar{\varepsilon}}^p$ defines the plastic flow condition (surface) at a fixed equivalent plastic strain rate per plastic work rate equivalency: $f(\boldsymbol{\sigma}_d)q(\dot{\boldsymbol{\varepsilon}}_d) = \sigma_f\dot{\bar{\varepsilon}}^p = \boldsymbol{\sigma}_d : \dot{\boldsymbol{\varepsilon}}_d$. There is a simple relationship between these two

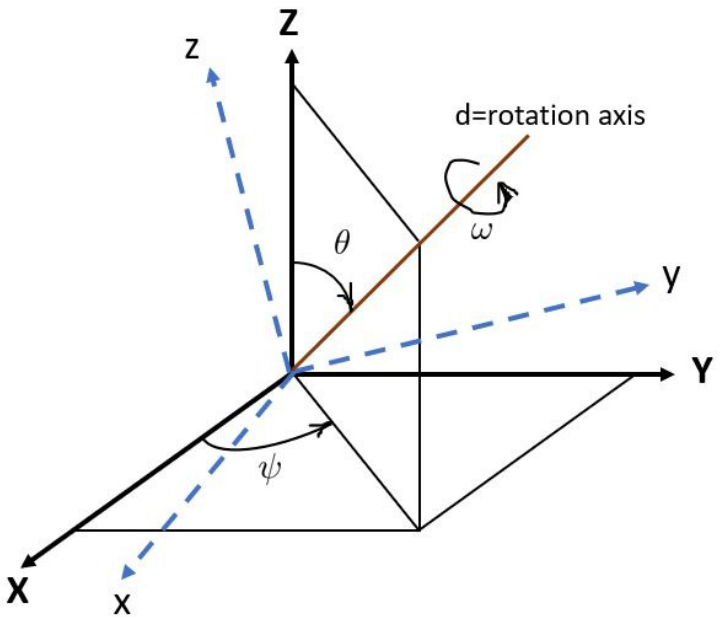

Figure 4.1: Rotation axes and Rodriguez angles.

sets of polynomial coefficients from the constitutive duality, namely

$$\begin{pmatrix} 2B_1 & B_2 & B_7 & B_{10} & B_{13} \\ B_2 & 2B_3 & B_8 & B_{11} & B_{14} \\ B_7 & B_8 & 2B_4 & B_{12} & B_9 \\ B_{10} & B_{11} & B_{12} & 2B_5 & B_{15} \\ B_{13} & B_{14} & B_9 & B_{15} & 2B_6 \end{pmatrix} = \begin{pmatrix} 2A_1 & A_2 & A_7 & A_{10} & A_{13} \\ A_2 & 2A_3 & A_8 & A_{11} & A_{14} \\ A_7 & A_8 & 2A_4 & A_{12} & A_9 \\ A_{10} & A_{11} & A_{12} & 2A_5 & A_{15} \\ A_{13} & A_{14} & A_9 & A_{15} & 2A_6 \end{pmatrix}^{-1} . \tag{4.20}$$

For the case of orthotropic sheet metal, one has the following algebraic relationships

(k=4,5,6)

$$A_1 = \frac{4B_3}{4B_1B_3 - B_2^2}, \quad A_2 = \frac{-4B_2}{4B_1B_3 - B_2^2}, \quad A_3 = \frac{4B_1}{4B_1B_3 - B_2^2}, \quad A_k = \frac{1}{B_k},$$
$$B_1 = \frac{4A_3}{4A_1A_3 - A_2^2}, \quad B_2 = \frac{-4A_2}{4A_1A_3 - A_2^2}, \quad B_3 = \frac{4A_1}{4A_1A_3 - A_2^2}, \quad B_k = \frac{1}{A_k}. \tag{4.21}$$

It is noted that both $4A_1A_3 - A_2^2 > 0$ and $4B_1B_3 - B_2^2 > 0$ per strict convexity requirements on $\Phi_2(\boldsymbol{\sigma}_d)$ and $\Psi_2(\dot{\boldsymbol{\varepsilon}}_d)$, respectively.

4.4.2 Calculations of Quadratic Plastic Potentials of Polycrystals

The quadratic yield functions will be derived for an orthotropic polycrystal by taking average of the quadratic yield functions of its K constituent single crystals following the classical Sachs iso-stress and Taylor iso-strain polycrystal modeling approaches [92], namely

$$\bar{\Phi}_{2o}^{S}(\boldsymbol{\sigma}_d) = \sum_{k=1}^{K} V^{(k)} \Phi_{2o}^{(k)}(\boldsymbol{\sigma}_d), \quad \text{or} \quad \bar{A}_i = \sum_{k=1}^{K} V^{(k)} A_i^{(k)}, \quad i = 1, 2, ..., 6, \tag{4.22}$$

$$\bar{\Psi}_{2o}^{T}(\dot{\boldsymbol{\varepsilon}}_d) = \sum_{k=1}^{K} V^{(k)} \Psi_{2o}^{(k)}(\dot{\boldsymbol{\varepsilon}}_d), \quad \text{or} \quad \bar{B}_i = \sum_{k=1}^{K} V^{(k)} B_i^{(k)}, \quad i = 1, 2, ..., 6, \tag{4.23}$$

where $V^{(k)}$ is the volume fraction of individual texture components or single crystals (i.e. $V^{(k)} = 1/K$), $\Phi_{2o}^{(k)}(\boldsymbol{\sigma}_d)$ is the quadratic yield stress function given by Eq.(4.13) for each orthotropic quartet of single crystals and $\Psi_{2o}^{(k)}(\dot{\boldsymbol{\varepsilon}}_d)$ is its dual plastic strain-rate function. It is noted that polynomial coefficients $(A_1, ..., A_6)$ of the Sachs quadratic yield stress function $\bar{\Phi}_{2o}^{S}(\boldsymbol{\sigma}_d)$ remain still linear combinations of slip system weights while polynomial coefficients $(B_1, ..., B_6)$ of the Taylor quadratic strain-rate function $\Psi_{2o}^{(k)}(\dot{\boldsymbol{\varepsilon}}_d)$ depends in a nonlienar manner with slip system weights per Eq.(4.20).

4.4.3 Quadratic Plastic Potentials of Randomly Textured Polycrystals

In this section, the Sachs model for random polycrystals is considered to check and verify the polynomial coefficients of a polycrystal generated by MATLAB code matching with the von Mises yield function coefficients.

As the polycrystal consists of randomly oriented single crystals, we need to generate random orientation distribution. However, random values of the Euler angles ϕ_1, Ψ and ϕ_2 will not give the random orientation distribution. In our computation, the random orientation distribution of K-crystals obtained from a MATALB texture analysis toolbox MTEX (https://mtex-toolbox.github.io/) was used. Euler angles (ϕ_1, Ψ, ϕ_2) can be converted to the Rodriguez angles (θ, ψ, ω) by

$$\omega = 2\cos^{-1}\left(\cos\frac{\Psi}{2}\cos\frac{\phi_1+\phi_2}{2}\right),\ \theta = \sin^{-1}\left(\frac{\sin\frac{\Psi}{2}}{\sin\frac{\omega}{2}}\right),\ \psi = \frac{1}{2}\left(\phi_1-\phi_2\right). \tag{4.24}$$

The polycrystal yield function of randomly oriented grains was obtained by averaging yield functions of single crystals. The most general anisotropic condition was considered first: cubic plastic anisotropy with all slip system weights equal to 1. It is supposed that each grain is modeled by the general quadratic yield function ϕ_2 of Eq.(4.8) with its 15 coefficients being given in terms of 12 distinct crystallographic slip system weights per Eq.(4.11). From the resulting averaged yield function, it was confirmed that $3\bar{A}_1 \approx 3\bar{A}_2 \approx 3\bar{A}_3 \approx \bar{A}_4 \approx \bar{A}_5 \approx \bar{A}_6$, and

$$\frac{\bar{A}_4}{3\bar{A}_1} \approx \frac{1.2\sum_{\alpha=1}^{12} w_\alpha}{(3)(0.4)\sum_{\alpha=1}^{12} w_\alpha} \approx 1. \tag{4.25}$$

Referring to Eq.(4.25) and $\frac{A_4}{3A_1} = 1$ for the most general symmetry condition, we can deduce that $\frac{A_4}{3A_1} = 1$ for all other higher symmetry conditions in Section 4.3.3, including monoclinic, orthotropic, cubic, etc. The variation of $\frac{\bar{A}_4}{3\bar{A}_1}$ with the number of grains is displayed in Fig.4.2. The value varies when the number of grain is less than 1000, and it approaches to 1 as the number of grains K increases up to 10,000. It will be shown that, if the orientation distribution of the single crystals are uniform or random, the resultant polycrystal yield function will approach to the von Mises yield function for all types of single crystal yield functions considered.

4.5 Calibration of Quadratic Plastic Potential for SS304L Single Crystals

To model the polycrystalline SS304L thin foils, material texture can be measured via different methods, but slip system weights are usually not accessible directly from experiments. Therefore, there is no experimental data on the individual slip strength as well as

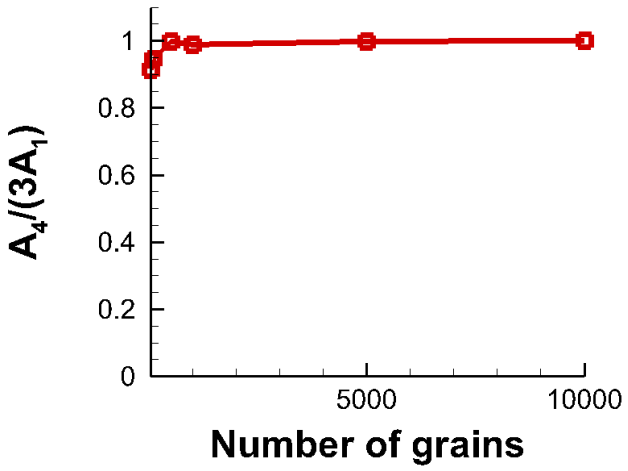

Figure 4.2: Variation of $\frac{\bar{A}_4}{3\bar{A}_1}$ with respect to the number of grains of a random polycrystals.

the rate-dependence and hardening behaviors of crystals provided at present. So, the calibration of quadratic plastic potentials for FCC single crystals comes down to parameter identification of 12 slip system weights per crystal when no experimental data is provided. Uniaxial tensile tests with different loading direction (RD and TD) are easily conducted on the polycrystalline SS304L thin foils at quai-static conditions. Consequently, a simplified rate-independent version of the crystal plasticity model presented in the previous section was used for modeling. The resulting model will be similar to the texture-based FCC single crystal plasticity model proposed by researchers for rolled sheets [92,98,99]. That is, the slip strength of crystal is represented by an isotropic slip hardening model, while an analytical stress function such as a quadratic polynomial with cubic or orthotropic plastic anisotropy in the local crystallographic axes is assumed to be the slip potential for multi-slips in each FCC single crystal. When modeling the plastic deformation of a polycrystalline SS304L foil at the individual grain level explicitly, each grain is assigned with known crystal orientation and its own slip potential as well as isotropic hardening law. The parameters of the isotropic

hardening of slip resistance or strength are to be estimated in order to match the stress-strain response measured from the actual tests.

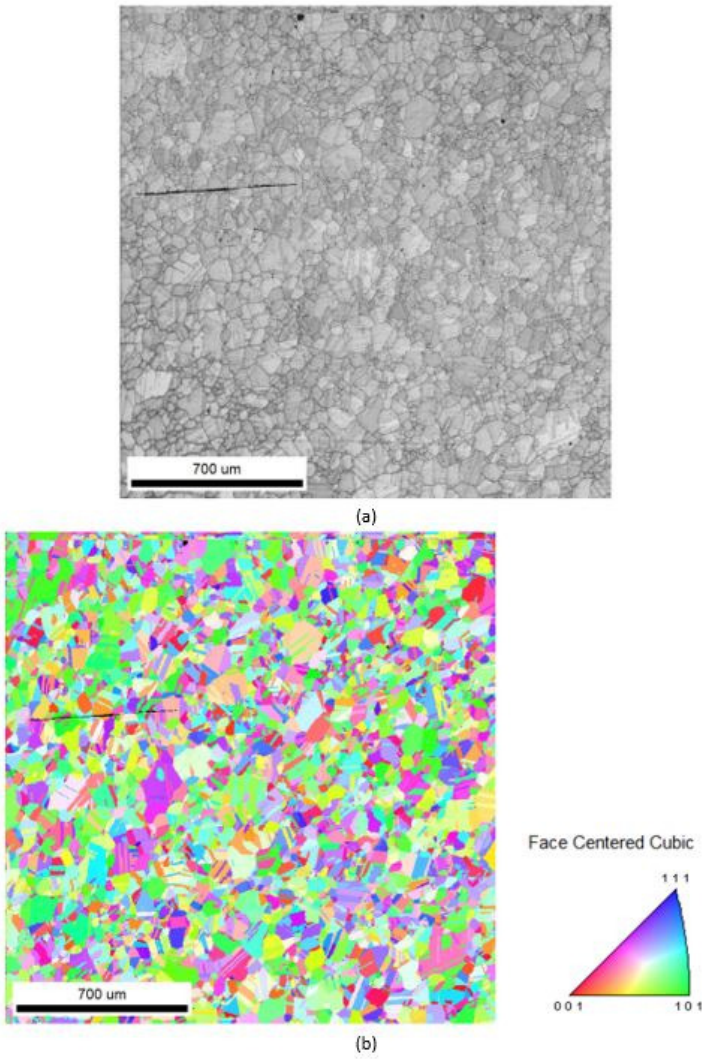

Figure 4.3: Two-dimensional cross-section micrographs of as-received SS304L: (a) image quality map and (b) color coded orientation map.

4.5.1 Grain Orientations of an SS304L Polycrystal

In the study of polycrystalline or polycrystalline material, electron backscatter diffraction (EBSD) has become a quantitative method to measure crystal orientations from a crystalline sample [106]. EBSD is a scanning electron microscope-based technique to characterize the microstructural-crystallography of the material. The ultra-thin stainless steel 304L (SS304L) is an austenitic low-carbon stainless steel, which is one of the popular materials studied for possible applications for PEM fuel cell manufacturing [12]. The microstructure examination of SS304L foil sheet was carried out by EBSD Analytical Inc. Fig.4.3 shows cross-section micrographs of as-received SS304L foil with the sample size are 2000 μm by 2000 μm and step is 2 μm. Using this technique, two-dimensional grain structure and its relevant grain information of as-received material were obtained, such as the crystal orientation, aspect ratio, etc.

For further analyzing and reconstructing of the experimental texture data, MTEX is employed [107]. The grain-based EBSD database of SS304L has been imported in MTEX in order to reconstruct the microstructure. The characteristics of such grain-based texture data consisting of the pole figures are shown in Fig.4.4. The orientation of each grain is obtained as the Euler angles in Bunge convention (ϕ_1, Φ, and ϕ_2). The distribution of these three Bunge Euler angles from the EBSD database are displayed in Fig.4.5 and Fig.4.6. For this set of EBSD data, the range of Euler angles is $0 - 2\pi$ for ϕ_1, $0 - \frac{2}{3}\pi$ for Φ and $0 - 2\pi$ for ϕ_2 respectively.

4.5.2 Single Crystals with Cubic Plastic Anisotropy

As discussed in Section 4.3.3 and previous study [92], all twelves slip system weights $(w_1, ..., w_{12})$ of single crystal with cubic plastic anisotropy for crystals are identical and equal to 1, shown in Eq.$(4.12)_{(5)}$. The polynomial coefficients of quadratic yield stress function and its dual strain rate potential per single crystal based on EBSD can be calculated via Eq.(4.11), Eq.$(4.12)_{(5)}$, Eq.(4.13), Eq.(4.16) and Eq.(4.21). If we assumed that every single crystal has the same volume fraction, the polynomial coefficients of yield functions for a

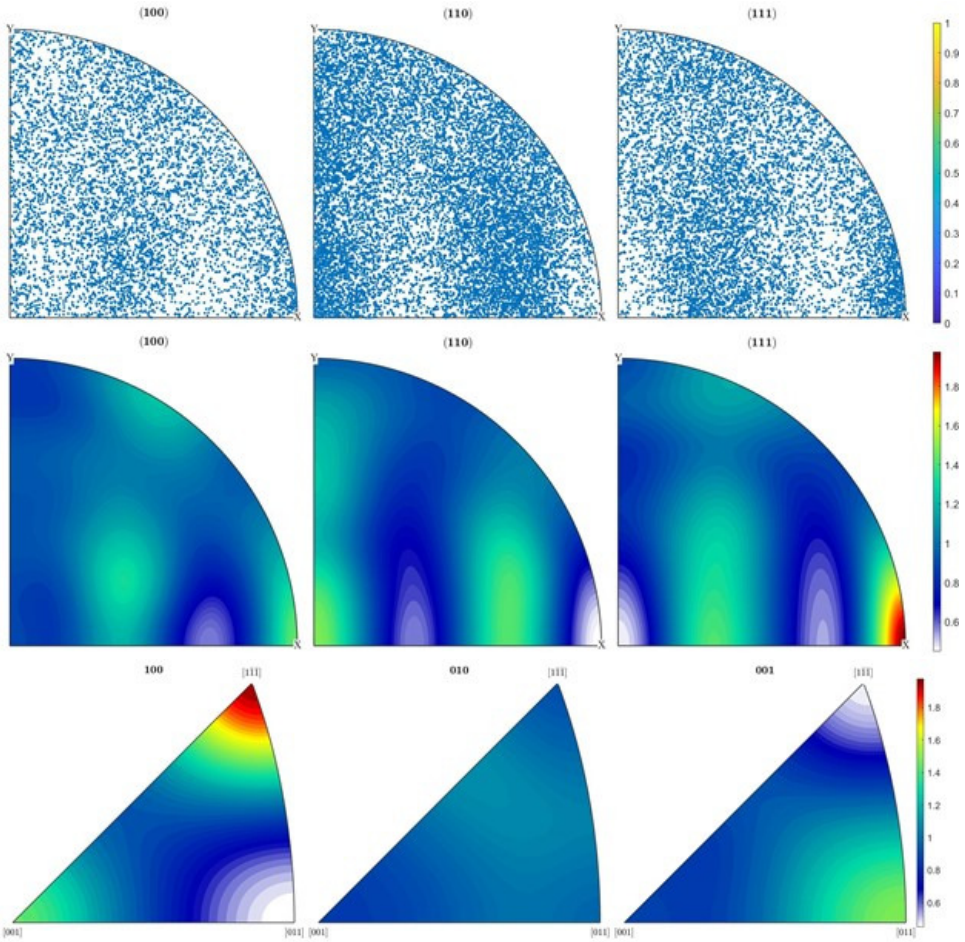

Figure 4.4: Pole figures of the reconstructed grain-based texture data (EBSD) : (a) top : pole figure of raw data point, each blue point represents a measurement position of a grain; (b) middle : pole figure after smoothing (recalculated pole figure in MTEX); (c) bottom : inverse pole figure after smoothing (recalculated inverse pole figure in MTEX).

cubic polycrystal are

$$\begin{aligned} \bar{A}_1 &= 0.78755, \quad \bar{A}_2 = -0.77541, \quad \bar{A}_3 = 0.78719, \\ \bar{A}_4 &= 2.44918, \quad \bar{A}_5 = 2.40204, \quad \bar{A}_6 = 2.40059, \end{aligned} \tag{4.26}$$

$$\begin{aligned} \bar{B}_1 &= 1.91082, \quad \bar{B}_2 = 1.81414, \quad \bar{B}_3 = 1.85587, \\ \bar{B}_4 &= 0.44635, \quad \bar{B}_5 = 0.45148, \quad \bar{B}_6 = 0.45727. \end{aligned} \tag{4.27}$$

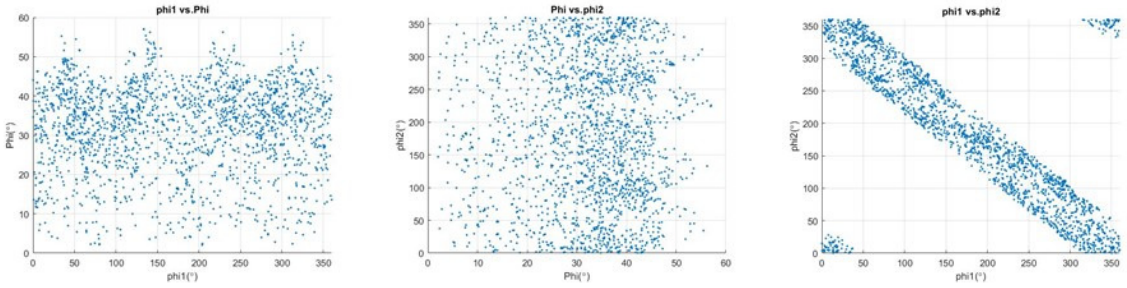

Figure 4.5: The Euler angle distribution based on EBSD provided by EBSD Analytical Inc.: (a) left : ϕ_1 vs. Φ; (b) middle : Φ vs. ϕ_2; (c) right : ϕ_1 vs. ϕ_2.

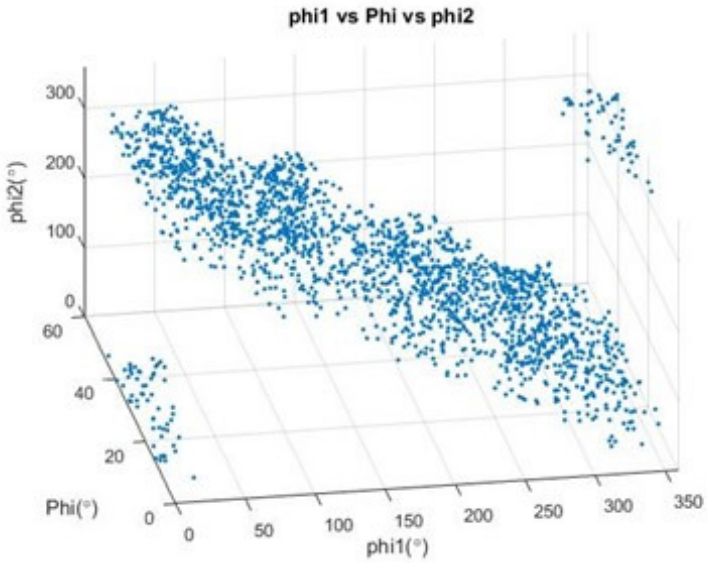

Figure 4.6: 3D View of the Euler angle distribution.

The predicted R-values for polycrystal of this case (Case #1) is $R_0 = 0.96962$ and $R_{90} = 0.97049$ for Sachs model, and $R_0 = 0.95601$ and $R_{90} = 0.90368$ for Taylor model.

4.5.3 Parameter Identification from the Sachs and Taylor Polycrystal Models

As cubic plastic anisotropy has been studied, the study for polycrystals with orthotropic plastic anisotropy becomes more complicated since the associated slip system weights are increased from one (w_1) to three (w_1, w_2 and w_3). It is difficult to determine the slip system

weight values without any experimental information. Therefore, three plastic strain ratios (R_0, R_{45}, R_{90}) are made available in addition to one stress from three uniaxial tensile tests, one can use the associated flow rule to determine the polynomial coefficients (A_1, A_2, A_3, A_4) of quadratic yield stress function per single crystal as (where $\sigma_f = \sigma_0$ is assumed, $A_1 = 1$ holds)

$$A_1 = 1, \quad A_2 = -\frac{2R_0}{1+R_0}, \quad A_3 = \frac{1+R_{90}}{1+R_0}\frac{R_0}{R_{90}}, \quad A_4 = \frac{R_0+R_{90}}{1+R_0}\frac{1+2R_{45}}{R_{90}}. \tag{4.28}$$

It is noted that plastic strain ratios can only be used to determine three out of four polynomial coefficients. Based on texture information from EBSD of SS304L, the expressions for polynomial coefficients of yield stress function and its dual strain rate potential per crystal are calculated via Eq.(4.11), Eq.$(4.12)_{(3)}$, Eq.(4.13), Eq.(4.16) and Eq.(4.21). Unlike cubic anisotropic case (here $w_1 = 1$), three slip system weights are determined by experimental plastic strain ratios. As discussed in Section 4.4, Sachs polycrystal plasticity assumes the local stress in each single crystal grain is the same as the stress acting on a polycrystalline continuum element [108, 109]. If the volume fraction of each crystal is equal, the quadratic yield stress function for an orthotropic polycrystal is derived and shown in Eq.(4.22). Eq.(4.28) is still valid for polycrystals by replacing A with $\bar{A}$ of Eq.(4.22), as

$$\bar{A}_1 = 1, \quad \bar{A}_2 = -\frac{2R_0}{1+R_0}, \quad \bar{A}_3 = \frac{1+R_{90}}{1+R_0}\frac{R_0}{R_{90}}, \quad \bar{A}_4 = \frac{R_0+R_{90}}{1+R_0}\frac{1+2R_{45}}{R_{90}}. \tag{4.29}$$

Here, two plastic strain ratios R_0 and R_{90} are 0.92 and 0.75 obtained from experiments via digital image correlation as initial guessing conditions for estimating polynomial parameters. Two more cases are considered as R_0 increases from 0.92 to 0.95 and 0.97, and R_{90} is not changed. Then, let the expression of $\bar{A}_2$ and $\bar{A}_3$ in Eq.(4.29) equals to the values in terms of R_0 and R_{90}, the crystallographic slip system weights and R-values used of each case are listed in Table 4.2. The associated polynomial coefficients of the macroscopic quadratic yield stress function and strain-rate potential are calculated and included in Table 4.3.

Taylor model is to assumes the local strain in each single crystal grain is the same as the strain applied to the polycrystalline continuum element [85, 110, 111]. This approach is

Table 4.2: Summary of R-values and slip system weights via Sachs model

Case	R_0	R_{90}	w_1	w_2	w_3
2	0.92000	0.75000	1.86696	1.27364	1.01680
3	0.95000	0.75000	1.91750	1.21245	1.05550
4	0.97000	0.75000	1.95035	1.17270	1.08065

Table 4.3: Summary of polynomial coefficients of YLD and its dual SRP via Sachs model

Case	$\bar{A}_1^{\mathrm{S}}$	$\bar{A}_2^{\mathrm{S}}$	$\bar{A}_3^{\mathrm{S}}$	$\bar{A}_4^{\mathrm{S}}$	$\bar{A}_5^{\mathrm{S}}$	$\bar{A}_6^{\mathrm{S}}$
2	1.00000	-0.95833	1.11806	3.22276	3.48926	3.36201
3	1.00000	-0.97436	1.13675	3.25992	3.52771	3.35593
4	1.00000	-0.98477	1.14890	3.28406	3.55269	3.35198
Case	$\bar{B}_1^{\mathrm{S}}$	$\bar{B}_2^{\mathrm{S}}$	$\bar{B}_3^{\mathrm{S}}$	$\bar{B}_4^{\mathrm{S}}$	$\bar{B}_5^{\mathrm{S}}$	$\bar{B}_6^{\mathrm{S}}$
2	1.25843	1.07865	1.12555	0.31029	0.28659	0.29744
3	1.26389	1.08333	1.11184	0.30676	0.28347	0.29798
4	1.26746	1.08640	1.10320	0.30450	0.28148	0.29833

to calibrate parameters using strain rate potential function instead of yield stress function. The quadratic strain-rate potential for an orthotropic polycrystal will be derived by taking average of quadratic strain-rate potentials of its K constituent single crystals, as shown in Eq.(4.23). When three plastic strain ratios (R_0, R_{45}, R_{90}) and one stress are measured from three uniaxial tensile tests, the four polynomial coefficients of strain rate potential function of a single crystal in terms of (R_0, R_{45}, R_{90}) with the assumption $\sigma_f = \sigma_0$ are:

$$\begin{aligned} B_1 &= \frac{(1+R_0)(1+R_{90})}{1+R_0+R_{90}}, \quad B_2 = \frac{2(1+R_0)R_{90}}{1+R_0+R_{90}}, \\ B_3 &= \frac{(1+R_0)^2 R_{90}}{R_0(1+R_0+R_{90})}, \quad B_4 = \frac{(1+R_0)R_{90}}{(1+2R_{45})(R_0+R_{90})}. \end{aligned} \tag{4.30}$$

The four polynomial coefficients of strain rate potential function for a polycrystal are easily obtained by replacing B with $\bar{B}$ of Eq.(4.23), as

$$\begin{aligned} \bar{B}_1 &= \frac{(1+R_0)(1+R_{90})}{1+R_0+R_{90}}, \quad \bar{B}_2 = \frac{2(1+R_0)R_{90}}{1+R_0+R_{90}}, \\ \bar{B}_3 &= \frac{(1+R_0)^2 R_{90}}{R_0(1+R_0+R_{90})}, \quad \bar{B}_4 = \frac{(1+R_0)R_{90}}{(1+2R_{45})(R_0+R_{90})}. \end{aligned} \tag{4.31}$$

The easiest approach to obtain polynomial coefficients of strain rate potential function per single crystal is to get the polynomial coefficients of yield stress function and convert A to B according to Eq.(4.21). After averaging, let the expression of $\bar{B}_1$, $\bar{B}_2$ and $\bar{B}_3$ in Eq.(4.31) equals to the values in terms of R_0 and R_{90}. Here, there are three sets of R_0 and R_{90} employed in this study: R_0 is 0.92, 0.95 and 0.97, R_{90} is fixed and equals to 0.75. The crystallographic slip weights, R-values, the associated polynomial coefficients of the macroscopic quadratic strain-rate potential and yield stress function of each case are listed in Table 4.4 and Table 4.5.

Table 4.4: Summary of R-values and slip system weights via Taylor model

Case	R_0	R_{90}	w_1	w_2	w_3
5	0.92000	0.75000	2.63313	1.44208	0.75806
6	0.95000	0.75000	2.81390	1.29652	0.79468
7	0.97000	0.75000	2.93616	1.20775	0.81452

4.5.4 Parameter Identification from a Finite Element RVE Model

As described in Section 4.4, both the Sachs and Taylor polycrystal theories are introduced to represent the behavior of polycrystalline material and calibrate the parameters using EBSD as texture data. Due to the limitations of these two approaches, uniform stress or uniform strain in a single crystal is assumed as the initial calibration, which is too ideal

Table 4.5: Summary of polynomial coefficient of SRP and its dual YLD via Taylor model

Case	$\bar{B}_1^{\mathrm{T}}$	$\bar{B}_2^{\mathrm{T}}$	$\bar{B}_3^{\mathrm{T}}$	$\bar{B}_4^{\mathrm{T}}$	$\bar{B}_5^{\mathrm{T}}$	$\bar{B}_6^{\mathrm{T}}$
5	1.25843	1.07865	1.12555	0.29348	0.29097	0.27680
6	1.26389	1.08333	1.11184	0.29012	0.28934	0.27398
7	1.26746	1.08640	1.10320	0.28790	0.28822	0.27206
Case	$\bar{A}_1^{\mathrm{T}}$	$\bar{A}_2^{\mathrm{T}}$	$\bar{A}_3^{\mathrm{T}}$	$\bar{A}_4^{\mathrm{T}}$	$\bar{A}_5^{\mathrm{T}}$	$\bar{A}_6^{\mathrm{T}}$
5	1.00000	-0.95833	1.11806	3.40740	3.43675	3.61271
6	1.00000	-0.97436	1.13675	3.44682	3.45611	3.64996
7	1.00000	-0.98477	1.14890	3.47339	3.46962	3.67563

for estimating the correct parameters for the real tests. In a previous study proposed by Tadano's group, a representative volume element (RVE) was used to obtain the polycrystalline behaviors of FCC Metals by using the Taylor model as the initial assumption [112]. Hence, obtaining R-values from the finite element analysis (FEA) is considered as the third method to gain more accurate parameters of a single crystal. Here, we use the estimated slip system weights via Sachs or Taylor polycrystal model as the input parameters of the modified Hill quadratic equation per single crystal to obtain R-values using FEA under uniaxial tensile condition.

4.5.4.1 Finite Element Model and Analysis of a Polycrystal RVE

A polycrystal RVE model presents as the polycrystalline SS304L foil is employed and simulated to illustrate the modified Hill's model for single crystal and polycrystal plasticity modeling. Eight different cases have been introduced in this section: first case is polycrystal modeling with cubic plastic anisotropy and all slip system weights equal to 1, then the following six cases are polycrystal modelings with orthotropic plastic anisotropy and the estimated slip system weights (w_1, w_2, w_3) of Case #2 to #7 listed in Table 4.2 and Table 4.4 were used, and the last case (Case #8) is to use the intermediate slip system weights between Case #3 and Case #6 with $R_0 = 0.95$ and $R_{90} = 0.75$. The estimated slip system weights for last case is $w_1 = 2.54498, w_2 = 1.27130$ and $w_3 = 0.87292$.

Two loading conditions (RD and TD) are applied to obtain R_0 and R_{90} from simulations. One more diagonal direction loading is employed for simulations using the estimated parameters of Case #2 and #5 to check the effect on R_{45}. Both stress and strain of the strain hardening law are corrected by certain scale factors and discussed in the next section. Young's modulus employed is 200 GPa and Possion's ratio used is 0.3. The RVE model used in the FEA is shown in Fig.4.7, consisting of one cube, three cubes and five cubes. From the previous study [112], an RVE model with 200 and more crystal grains is sufficient to describe the behaviors of FCC polycrystalline metal. The initial geometry of each cube in this study is $10 \times 10 \times 10$ mm^3 with the total number of elements is 2028 (13 by 13 by 12 elements per edge). The total number of crystals of EBSD is 2030, only 2 sets of Euler angles are not used in FEA, the result of the RVE model assigned with 2028 sets of Euler angles randomly are representative of the response of SS304L foil. Based on the results of simulation using different number of grains and the study proposed by Kasemer et al. [113], it concludes that the R-value remains steady as the grain number increases. Therefore, the simplest model (one cube) is chosen for further studies, as shown in Fig.4.7(a). The applied boundary conditions are: at $x = 0$ mm, all nodes are fixed in X-direction, point $(0, 0, 0)$ is prescribed in Y and Z directions and point $(0, 10, 0)$ is fixed in Z direction to prevent the rotations. Two approaches could be used for adding applied loads to the model: certain uniform displacement or uniform force (pressure) distribution. Checked by simulations, the results of applying with either uniform displacement or uniform pressure distribution give very similar force and displacement responses. To mimic a test coupon under a uniaxial tensile test, the latter method is chosen and applied to the surface located at $x = 10$mm.

4.5.4.2 Input Parameters of Individual Single Crystal Grains

The associate quadratic yield stress function of Hill's model [34, 35] in the specimen coordinate system is used and expressed as (setting $\sigma_z = 0$ for simplicity and consistency)

$$\Phi_h(\boldsymbol{\sigma}) = \frac{G+H}{2}\sigma_x^2 + \frac{F+H}{2}\sigma_y^2 - H\sigma_x\sigma_y + N\tau_{xy}^2 + M\tau_{zx}^2 + L\tau_{yz}^2, \tag{4.32}$$

where F, G, H, L, M, and N are the material constants that be determined by the experimental results in general. As described in the previous section, a modified Hill's quadratic

yield function is used to define the input parameters of the simplified crystal plasticity model for FEA. Per single crystal, the rotation matrix of the Bunge Euler angles rotating from the specimen coordinate system to the crystal coordinate system is shown in Eq.(4.16). Applying $\boldsymbol{\sigma}^* = \mathbf{Q}\boldsymbol{\sigma}\mathbf{Q}^\mathsf{T}$, the coefficients of nine stress components (in terms of $\sigma_x, \sigma_y, \sigma_z, \tau_{xy}, \tau_{yz}$, and τ_{zx}) of the average plastic potential of a single crystal for a orthotropic polycrystal material expressed in the crystal cubic coordinate frame are obtained via the Bunge Euler angles and its three mirror-symmetric copies (see Eq.(4.13)). Let $\Phi_2(\boldsymbol{\sigma}_d)$ of Eq.(4.7) equals to $\Phi_2(\boldsymbol{\sigma})$ of Eq.(4.32) (the expression used in ANSYS), the relationships between these two expressions of Hill's model per single crystal are shown as

$$F = A_2 + 2A_3, \quad G = 2A_1 + A_2, \quad H = -A_2, \quad N = A_4, \quad L = A_5, \quad M = A_6. \tag{4.33}$$

Then, the input parameters (the Hill yield surface directional yield ratio R_{ij}) of single crystal in ANSYS are calculated as

$$\begin{aligned}
&R_{xx} = \frac{\sigma_x}{\sigma_f} = \sqrt{\frac{2}{G+H}} = \sqrt{\frac{1}{A_1}}, \quad R_{yy} = \frac{\sigma_y}{\sigma_f} = \sqrt{\frac{2}{F+H}} = \sqrt{\frac{1}{A_3}}, \\
&R_{zz} = \frac{\sigma_z}{\sigma_f} = \sqrt{\frac{2}{F+G}} = \sqrt{\frac{1}{A_1+A_2+A_3}}, \quad R_{xy} = \sqrt{3}\frac{\tau_{xy}}{\sigma_f} = \sqrt{\frac{3}{N}} = \sqrt{\frac{3}{A_4}}, \\
&R_{yz} = \sqrt{3}\frac{\tau_{yz}}{\sigma_f} = \sqrt{\frac{3}{L}} = \sqrt{\frac{3}{A_5}}, \quad R_{zx} = \sqrt{3}\frac{\tau_{zx}}{\sigma_f} = \sqrt{\frac{3}{M}} = \sqrt{\frac{3}{A_6}}.
\end{aligned} \tag{4.34}$$

For the polycrystal microstructure, the input parameters of each grain are different and computed from its own Euler angles. The effect of the strain hardening also needs to be considered for polycrystal modeling, because stress-strain curve obtained from the experiment usually reflects the overall mechanical behavior of all grains. Therefore, for a polycrystal model in which the characterization of each grain is defined separately, strain hardening curve should be corrected with the scale factor of the stress and strain for this study are $\sqrt{1.732}$ and $\frac{1}{\sqrt{1.732}}$.

4.5.4.3 Results

The force verse axial displacement, true axial stress and strain curve, and R-value verse axial displacement of Case #2 with RD as the loading condition are shown in Fig.4.8, it shows

that the R-value is not a constant and changed along with axial deformation. At the initial stage, a hugh variation is observed and may cause by the developing of grain heterogeneity of the model. R-value is virtually constant with slight decreasing when the large strain is applied. The nodal displacement, stress component distribution, elastic strain component distribution, and plastic strain component distribution in the X-axis of simulations of the same case are displayed in Fig.4.9.

The corresponding plastic strain ratio R via FEA is calculated as shown

$$R(\varepsilon_a^p) = \frac{\mathrm{d}\varepsilon_w^p}{\mathrm{d}\varepsilon_t^p}, \tag{4.35}$$

where ε_a^p is true plastic strain in axial direction, $\mathrm{d}\varepsilon_w^p$ and $\mathrm{d}\varepsilon_t^p$ are true plastic strain increment in width and thickness. Here, the average strain of each surface of the RVE model were examined and used for the plastic strain ratio calculations, and the calculated R-values are included in Table 4.6 at the true axial plastic strain is around 10%. As well known, the austenite phase of SS304L can transform into the martensitic phase when certain deformation is induced. In previous paper [114], researchers claim that the predicted R-value of uniaxial tensile test is in good agreement with the experiment even phase transformation is not considered within a certain strain level (about the strain of 0.15) as shown in Fig.9 of their paper. In this study, the true axial plastic strain is about 10% (the engineering strain of about 11%) and within the range as they proposed [114]. Therefore, the effect caused by the phase transformation that happened within grains could be ignored.

For Case #2 and #5, one additional simulation was carried out with the loading direction is diagonal direction (45° rotated from the RD of test coupon). The predicted R-value via FEA is 0.96985 for Case #2 and 0.95494 for Case #5, respectively.

4.5.5 Discussions

As detailed in the previous sections, three approaches were used to calibrate the parameters of a single crystal with orthotropic plastic anisotropy: Sachs polycrystal model, Taylor polycrystal model, and FEA model. The summarized table of predicated R-values and estimated weights of the slip system of a single crystal used in simulations are shown in Table 4.6. Here, the superscript S is the results using Sachs polycrystal model, T relates to the

Table 4.6: Summary of slip system weights and R-values via FEA and Sachs/Taylor model

Case	w_1	w_2	w_3	R_0^{F}	R_{90}^{F}	$R_0^{\mathrm{S}}/R_0^{\mathrm{T}}$	$R_{90}^{\mathrm{S}}/R_{90}^{\mathrm{T}}$
1	1.00000	1.00000	1.00000	0.94300	0.96065	R_0^{S}:0.96962 R_0^{T}:0.95601	R_{90}^{S}:0.97049 R_{90}^{T}:0.90368
2	1.86696	1.27364	1.01680	0.91808	0.84387	0.92000	0.75000
3	1.91750	1.21245	1.05550	0.93828	0.82760	0.95000	0.75000
4	1.95035	1.17270	1.08065	0.95060	0.81692	0.97000	0.75000
5	2.63313	1.44208	0.75806	0.87366	0.76947	0.92000	0.75000
6	2.81390	1.29652	0.79468	0.91070	0.73117	0.95000	0.75000
7	2.93616	1.20775	0.81452	0.93433	0.70725	0.97000	0.75000
8	2.54498	1.27130	0.87292	0.91849	0.75575	0.95000	0.75000

results obtained from Taylor polycrystal model, and F is simulated or predicted values using FEA. Case #1 is the simulation using cubic plastic anisotropy and all slip system weights is the same and equals to 1, as discussed in Section 4.5.2. When orthotropic plastic anisotropy is applied, that is, three slip system weights (w_1, w_2 and w_3) are independent parameters, and the remaining slip system weights can be expressed by these three weights shown in Eq.(4.12).

As R-values showed in Table 4.6, it should be noted that there is no exact match between the simulation (Case #1 to #8) and experiment, Case #8 has the closest match with experimental R_0 and R_{90}, about 0.002 and 0.005 difference from the experimental results receptively. The slightly larger scatter on R_{90} may cause by the strain hardening law used in FEA was obtained from a RD tensile test, not a TD tensile test. In the study by other researchers [114], the stress-strain curve of TD is lower than the curve got from RD test, which may affect the R-values of simulations. For Case #1 (cubic plastic anisotropy), R_{90} is larger than R_0 for Sachs model that is contrary from the values obtained from experiments, the same trend is obtained for Taylor model but R_{90} is far away from experimental R_{90}. That is, R-values obtained from FEA model with orthotropic plastic anisotropy imposed instead of cubic plastic anisotropy give more accurate predictions and close to the experimental results.

From the results of Case #2 and #5 shown, the largest R-value of one set with different loading conditions is R_{45}, R_{45} for Case #2 and #5 is about 0.97 and 0.96, which is larger than R_0 of each case. The same trend but not the identical value is observed by Jeong et al. [114]. Other parameters that may affect R-values of the simulations are not considered in this study, such as grain morphology, numerical discretization, etc.

Calibrations of a single crystal via Sachs and Taylor polycrystal models are reported in Table 4.3 - Table 4.5, including the slip system weights and the corresponding polynomial coefficients of the quadratic plastic potential per single crystal. Case #2 and #5 are cases calibrated via Sachs and Taylor models with the imposed R-values obtained from experiments directly. As shown in Table 4.3 and Table 4.5, it is noticeable that even the slip system weights are quite different, but some polynomial coefficients of the quadratic plastic potential are identical ($\bar{A}_1^{\mathrm{S}}$ to $\bar{A}_3^{\mathrm{S}}$ for Case #2 and $\bar{A}_1^{\mathrm{T}}$ to $\bar{A}_3^{\mathrm{T}}$ for Case #5) and related to the imposed R-values. Similar situations are found from other two sets of the calibrated parameters (Case #3 and #6, Case #4 and #7) with R_0 is changed. It verified the found in Chapter 3, the slip system weights may not be unique even some or all associate polynomial coefficients $\bar{A}$ of yield function are identical. $\bar{A}_4$, $\bar{A}_5$ and $\bar{A}_6$ are not identical among the cases using Sachs and Taylor methods with the same R-values imposed, but the results shows that $\bar{A}_4^{\mathrm{S}} < \bar{A}_4^{\mathrm{T}}$, $\bar{A}_5^{\mathrm{S}} > \bar{A}_5^{\mathrm{T}}$, and $\bar{A}_6^{\mathrm{S}} < \bar{A}_6^{\mathrm{T}}$. By artificially increasing R_0 from 0.92 to 0.97 for both models, $\bar{A}_2$ decreases as well as the rest coefficients ($\bar{A}_3$ to $\bar{A}_5$) increase. $\bar{A}_1$ is always 1 as the imposed condition, $\bar{A}_6$ shows different trends: $\bar{A}_6^{\mathrm{T}}$ increases and $\bar{A}_6^{\mathrm{S}}$ decreases when R_0 increases.

The associated polynomial coefficients of dual strain rate potential are listed in Table 4.3 and Table 4.5 as well. According to the expressions (see Eq.(4.21)), the first three polynomial coefficients ($\bar{B}_1$, $\bar{B}_2$, $\bar{B}_3$) of strain rate potential only relate to the first three polynomial coefficients ($\bar{A}_1$, $\bar{A}_2$, $\bar{A}_3$) of yield stress function, thus the first three polynomial coefficients ($\bar{B}_1$, $\bar{B}_2$, $\bar{B}_3$) of strain rate potential via either Sachs or Taylor model using the same R-values as initial guess are identical, and the inverse trend are found for the rest coefficients: $\bar{B}_4^{\mathrm{S}} > \bar{B}_4^{\mathrm{T}}$, $\bar{B}_5^{\mathrm{S}} < \bar{B}_5^{\mathrm{T}}$, and $\bar{B}_6^{\mathrm{S}} > \bar{B}_6^{\mathrm{T}}$. With R_0 increasing, $\bar{B}_3$ to $\bar{B}_5$ decrease as well as $\bar{B}_1$ and $\bar{B}_2$ increases. $\bar{B}_6$ via Sachs model increases, while $\bar{B}_6$ via Taylor model decreases.

In summary, the simplified rate-independent version of the crystal plasticity model pre-

sented in the section with an isotropic slip hardening model as slip strength and a quadratic polynomial with cubic or orthotropic plastic anisotropy in the local crystallographic axes as the slip potential is an effective method to calibrate the parameters of the quadratic macroscopic plastic potential of a single crystal. For our focus, the first three coefficients ($\bar{A}_1$ to $\bar{A}_3$ or $\bar{B}_1$ to $\bar{B}_3$) are important to R-value predictions, which the R-values of FEA model show either larger or smaller than the values obtained from Sachs or Taylor in most cases. Compared R-values with Sachs and Taylor models, the R-values of FEA model are more accurate and reflect the material responses of tensile tests. Case #8 has the closest match with experimental R_0 and R_{90} with crystallographic slip system weights is $w_1 = 2.54498, w_2 = 1.27130$ and $w_3 = 0.87292$.

4.6 Conclusions

In this chapter, the macroscopic and microscopic quadratic plastic potentials used for modeling continuum plasticity of an FCC single crystal have been evaluated for both general and reduced plastic anisotropy. By their equivalency, the number and type of independent material constants have been identified for six specific cases of plastic anisotropy. Quadratic plastic potential of texture components is subsequently evaluated as well based on various degrees of plastic anisotropy of constituent single crystals. It is found that a commonly used macroscopic quadratic plastic potential of FCC crystals with orthotropic plastic anisotropy can be derived directly from its microscopic counterpart based on crystallogrphic slips. Some simulations of a RVE model using ANSYS input parameters obtained by the simplified rate-independent Hill's model for a polycrystal and EBSD data show the validation of this micro-to-macro transition method with some constitutive assumptions are made. Calibration on parameters of the quadratic plastic potential and slip system weights of SS304L grain is also presented via three methods: Sachs polycrystal model, Taylor polycrystal model and FEA model. The simulated R-value via FEA model is more accurate and close to the experimental results, and the case with orthotropic plastic anisotropy imposed and a certain slip system weights used ($w_1 = 2.54498, w_2 = 1.27130$ and $w_3 = 0.87292$) gives the best match.

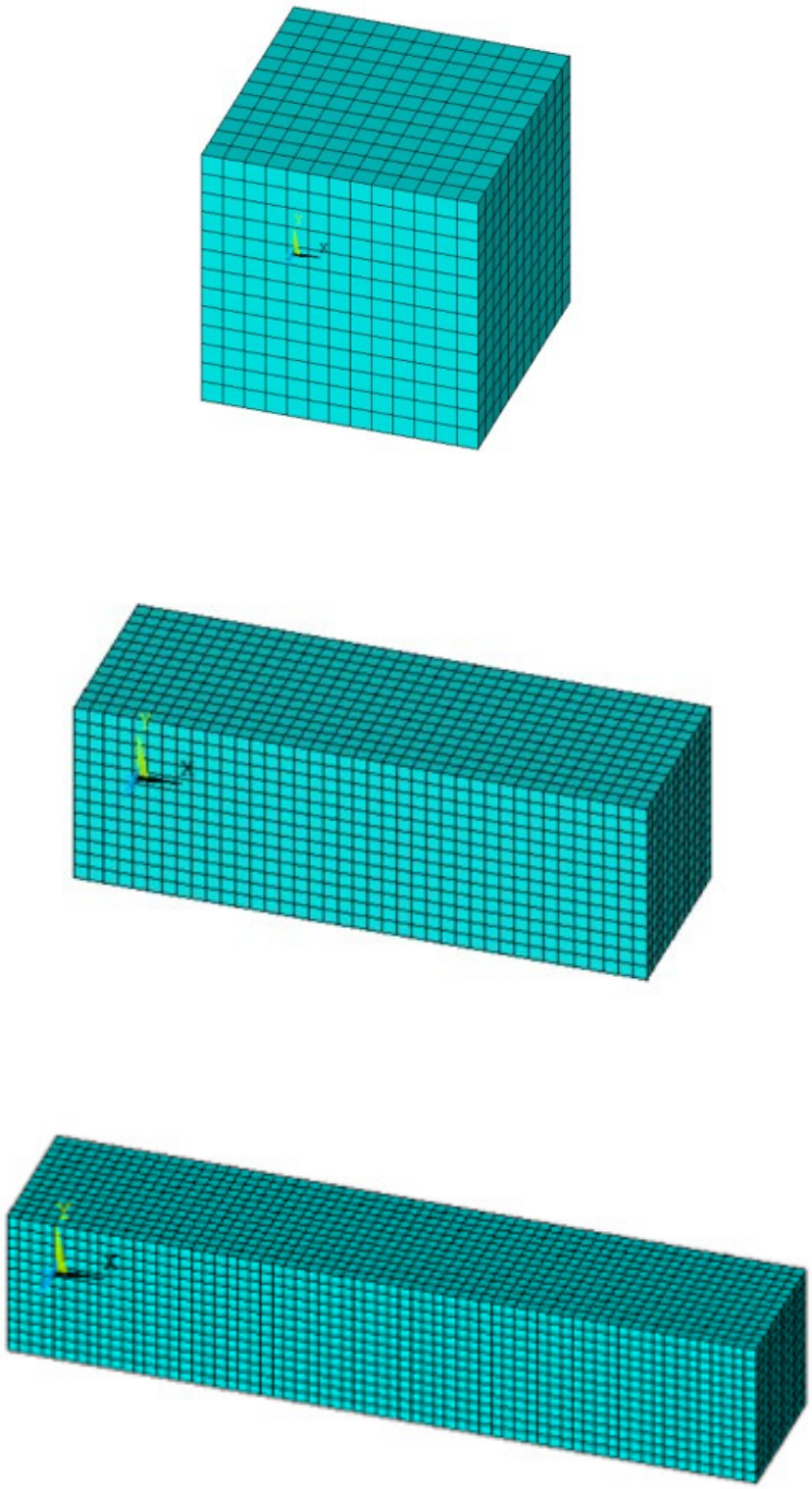

Figure 4.7: Geometry of a RVE model: (a) one cube; (b) three cubes; (c) five cubes(from top to bottom).

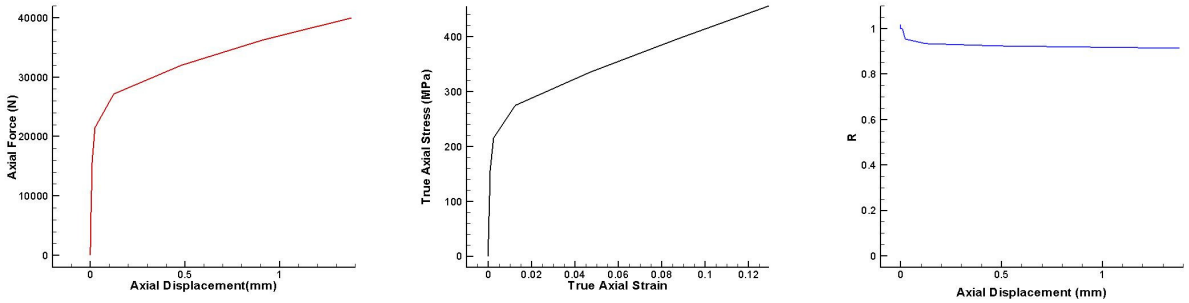

Figure 4.8: Simulation Results of Case #2: (a) force vs axial displacement ; (b) true stress verse true strain ; (c) R-value verse axial displacement.

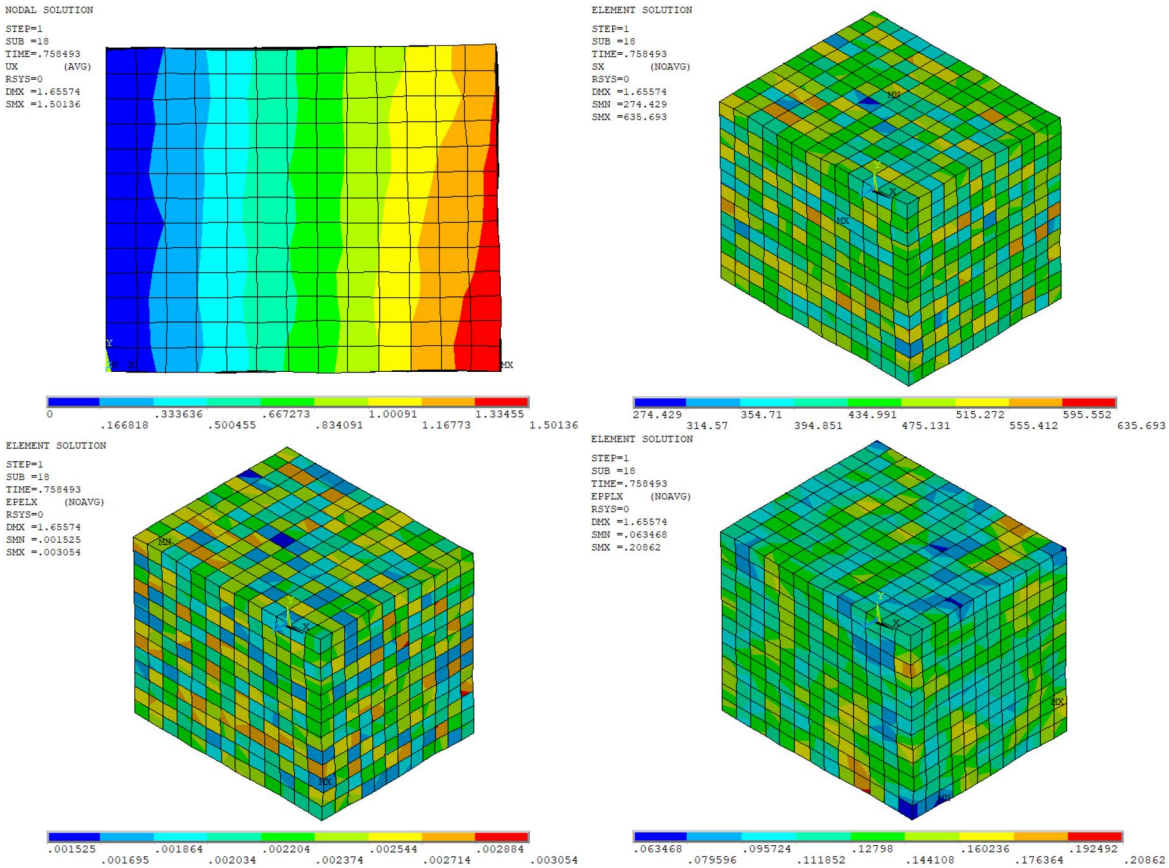

Figure 4.9: The contour plots of Case #2 in loading direction (X-axis of local coordinate system in ANSYS): (a) top left : nodal displacement ; (b) top right : stress component ; (c) bottom left : elastic strain component ; (d) bottom right : plastic strain component.

Chapter 5

EXPERIMENTAL INVESTIGATION AND NUMERICAL ANALYSIS OF MICRO-CHANNEL FORMING OF STAINLESS STEEL FOILS

5.1 Introduction

Fuel cells have gained increasing attentions and are highly efficient and environmentally friendly substitutes for internal combustion engines in the automotive industry. Forming is one of the major processes commonly used in the fabrication of fuel cell parts by placing metal sheet between a pair of forming tools where tools deform metal pieces into a specific shape since it is a mass-production economical process. Ford has adopted metal forming for automotive part manufacturing since the 20th century, and such process is still used for automotive fuel cell manufacturing in nowadays [115]. Metal forming process uses punch and die as a pair of tools to form sheet metal into different pre-defined shapes: the male part is called punches or upper die, which moves down and deforms the metal, and the female part is called die or lower die. Both punch and lower die are made of the hardened steel and match the desired contour of the part. The trend of metal forming for automation manufacturing nowadays is focused on down-scaling the size of the products to reduce the cost and increase exchange efficiency in reaction area for fuel cells. Therefore, micro forming is one of the suitable methods for the mass production. Due to the limitations of machines and manufacturing conditions, micro forming process is difficult to control precision of products during high-volume handling processes [11].

Since metal needs to be deformed into different shapes during forming process, material used for this process is required to flow easily in order to be formed into various shapes. In recent years, ultra-thin stainless steel is most commonly used in such forming processes due to its high tensile stress, resistance to corrosion, and ductility. However, using stainless steel also leads to an extensive elastic deformation recovery in the specimen after manufacturing

process. Such kind of recovery is called springback, which is a material behavior related to the release of elastic deformation after working load is removed. In fuel cell industry, one of the critical concerns about micro forming is the application of metallic material with 100 μm thick and below [116]. To reduce springback effect on final shape, there are three most common approaches by changing processing conditions used in industry: bending the pieces by applying through tension force, increasing the working load, and increasing the holding time on the material. Besides processing conditions, material properties, tool's geometries and test procedures are also considered factors that mostly affect springback behaviors. To understand the mechanism that how springback happens and to predict more accurate shape of the deformed part, many research groups have developed and investigated via various methods over the past few years, such as analytical method [117–119] and numerical method [22–26]. Various material properties and different geometry and shape of tools have been extensively studied [14, 27–29]. Multi-stage forming processes have also been evaluated in various fields [15, 16, 120]. The shape of every stage will affect final product forming quality. Compared with tests, the computer-based simulation method provides much easier and affordable approach to check the associate springback behaviors with different material and test conditions quickly and efficiently. Therefore, the studies of material springback via simulations are significant and necessary to guide engineers on improving the quality of the products and decreasing production costs.

Ultra-thin SS304L foil is an austenitic low-carbon stainless steel widely used in industries due to its material properties, such as good formability, high strength, and high hardness. This type of material has limited grains distributed through the thickness, hence it could use either a macroscopic or microscopic plasticity model to simulate specimen responses under different test conditions. Different plasticity models may have a great influence on material behaviors.

In this chapter, both experimental and computational methods are carried out to predict effects of springback compensation of SS304L, which lead by material properties and test conditions (the max load reached). For numerical approach, a macroscopic plasticity theory and a microscopic plasticity theory with cubic or orthotropic plastic anisotropy described in Chapter 4 are examined to estimate springback behaviors of material. The direct compar-

isons between experiments and two simulation methods are presented to evaluate replication and difference caused by various possible factors among these three approaches.

5.2 Material and Methods

5.2.1 Material and Specimen Preparation

The ultra-thin stainless steel foil sheet investigated in this study is SS304L with 0.075 mm thickness. Test specimens are prepared with the longitudinal axis aligned with the rolling direction (RD) of foil sheet. Waterjet cutting was employed to cut specimens into a 5 mm wide strip from one large foil sheet. Length of each specimen has less effect on springback behaviors, thus paper cutter was used to trim strip into a specimen with certain length manually. The length of each cut specimen was measured using a caliper before the test, and the original length of the tested specimen was about 15mm, as shown in Fig.5.1. To reduce edge effect caused by paper cutter, each specimen was compressed and flatten with a pair of clean, smooth steel compression flat patterns of Instron machine.

Figure 5.1: 75 μm thick specimen with the length is around 15 mm.

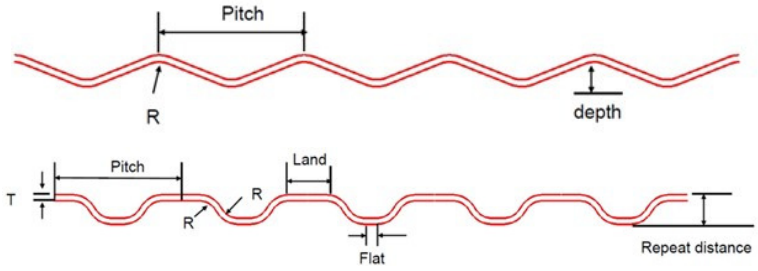

Figure 5.2: The schematic drawings : (a) 1st line : preform forming tool and (b) 2nd line : conformal final forming tool.

5.2.2 Micro Channel Forming Tool Preparation

Micro channel forming tool plays an essential role in micro channel forming and may affect the amount of springback of the bent material. Each pair of forming tool consists of a punch and a lower die and is used to deform the foil specimens permanently. Hence, it is important to design a proper toolset with a specified pitch, depth, land, bottom/flat, and the number of repeated profiles. The schematic drawings of different forming tools are displayed in Fig.5.2, there are five repeated profiles as forming channels of the toolset used in this design.

Preform profile (see the first drawing of Fig.5.2) as the simplest and representative one is evaluated in this study, and its associate geometry is listed in Table 5.1. The schematic drawing of half channel of preform forming tool in Solidworks is shown in Fig.5.3 .

Table 5.1: Geometry of preform forming toolset (in mms)

Name	Pitch	Depth	R
PF1.3R20T75	1.3	0.235	0.20

Preform forming toolset could be used in one-stage forming test or the first stage of the two-stage forming test, which consists of three parts per half channel: two curve parts and a straight part connects these two curve parts. The expressions for calculating the central angle γ of the curve part are

$$\begin{aligned}
\tan\gamma = \frac{D + R(\frac{1}{\cos\gamma} - 1) + (R+t)(\frac{1}{\cos\gamma} - 1)}{P} &= \frac{D - 2R(1-\cos\gamma)}{P - 2R\sin\gamma}, \\
P\sin\gamma + (2R + t - D)\cos\gamma &= 2R + t, \\
\frac{P}{\sqrt{P^2 + (2R+t-D)^2}}\sin\gamma + \frac{2R+t-D}{\sqrt{P^2+(2R+t-D)^2}}\cos\gamma & \\
= \frac{2R+t}{\sqrt{P^2+(2R+t-D)^2}}\cos\gamma, &
\end{aligned} \tag{5.1}$$

where P is half-length of the pitch, t refers to thickness of foil specimen, 0.075mm, D is depth, R represents the radius of the curve part. The central angle of curved part of this preform design is 23.0118°.

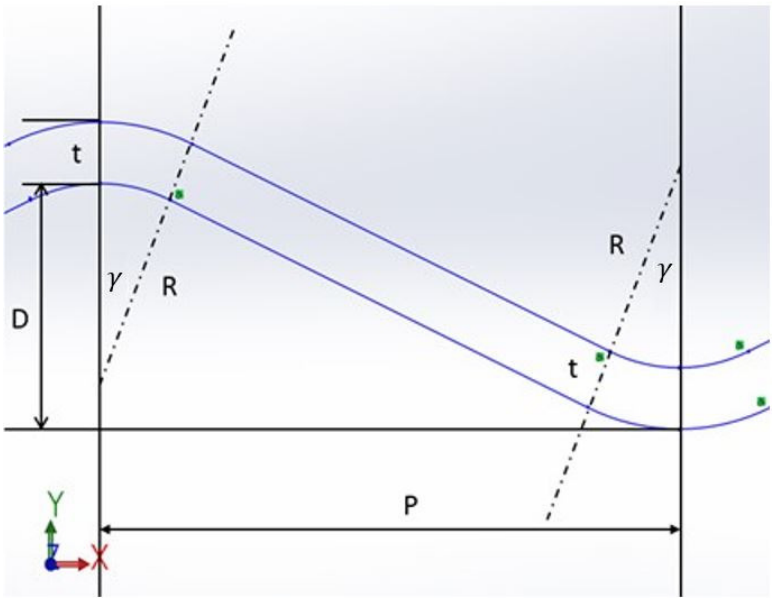

Figure 5.3: Schematic drawing of the half channel of prefrom forming toolset in Solidworks.

Forming toolset was machined by Micro waterjet Company, and its material is S7 HRC 52-54. The surface finish of tool is 0.4-0.8 microns, and heat treatments are required before machining. The tolerance of parallel and perpendicular is 0.01 and 0.025, respectively. The overall dimensions of tools are about 56.5 mm × 6.35 mm × 14.50 mm for punch and 56.5 mm × 6.35 mm × 10.0 mm for lower die, the overview of the assembled preform toolset is shown in Fig.5.4.

Figure 5.4: The overview of assembled preform set : pitch=1.3mm, depth=0.235mm, and the radius of the curve part R=0.20mm.

5.2.3 Test Equipment

Micro channel forming tests were carried out at room temperature with an Instron 5967 dual column tabletop universal testing system with a max capacity of 30kN. The machine was equipped with the compression flat patterns where the forming toolset placing on through strong stainless-steel magnets (see Fig.5.5). The moving head traveled with a speed of 0.005 mm/s, and the reading of load cell was recorded continuously at a 100 Hz data acquisition rate. The effective travel distance (tool starts to have contact surface with specimen till the end of loading step) is about 0.28 mm per test, it holds for 50 seconds when the max load is reached, about 2000N. Load control mode was used for the loading part, while displacement

control mode was employed for the unloading part. Per test, a high-resolution USB3 digital camera with a macro zoom lens was used to record test history. The frame rate of the recording camera was 4 fps with the image size is 1960×1200 pixels, and a typical pixel resolution is about 2.1 μm per pixel on average. There are roughly 350 or more images recorded for a complete test, as only one out of four images was saved to the computer. Two additional light sources were used to lighten test environment: a lamp was used to provide the front lighting, and the other one was backlighting source provided by a diffuse LED white light panel. By turning the front light on, specimen deformation is easily observed in the images, and backlighting is to check the gap between specimen and toolset at the max load or the profile of specimen by turning off the front lighting. After each test, a KEYENCE digital microscope VHX500 equipped with two different lenses were also used to capture specimen profile from the top and side view.

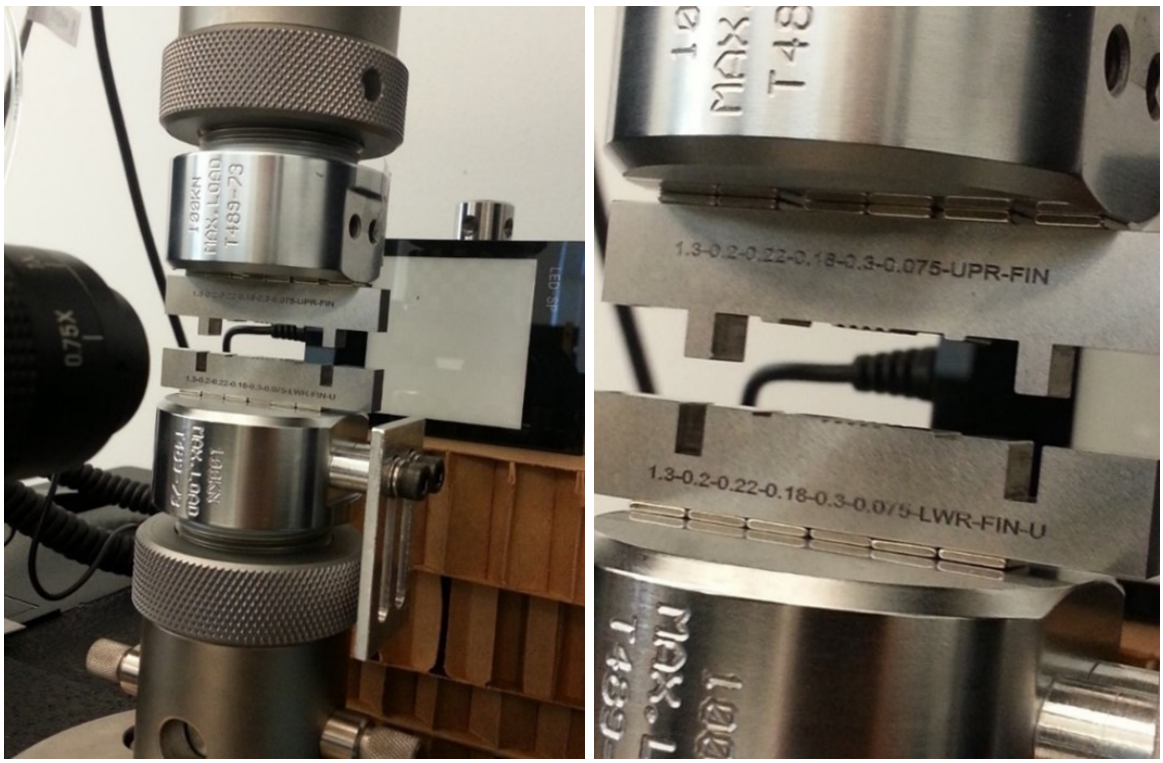

Figure 5.5: Test setup : (a) left : the overview of test setup and (b) right : the zoom-in view of the punch and lower die.

5.3 Experimental Results

According to the number of stage, there are two types of forming tests could be performed: one-stage test and two-stage test. One-stage forming test is also called one-step test, which is to form specimen only one-time using forming toolset. Two-stages forming test (or two-steps test) refers to use preform toolset first to form specimen from flat condition to the shape of channel profile of preform tool and to shape the same specimen to the profile of final tool in the second forming. As only preform forming tool is analyzed in this study, one-stage preform forming test is presented in the following sections. Test information about forming tool set and loading condition (the peak load presented) used in the experiments is listed in Table 5.2. The applied max peak load per 1 mm wide is about 400 N/mm.

Table 5.2: One-stage test with preform forming set

Tool	Peak Load (N)
P2(PF1.3R20T75)	2000

An example set of continuously recorded images using preform forming set (P2) with the peak load is 400 N/mm is shown in Fig.5.6, the punch and lower die have full contact with specimen at the max load. The left image in the first line is a recorded image of the initial holding, images in the middle and right are recorded images under loading condition. In the second line: the left and middle images are recorded at the max load with front lighting and diffuse backlighting condition, and the right image is a recorded image at unloading condition. Fig.5.7 depicts force versus displacement curve of the Instron machine data. The images of specimen profile after removing from the tools were taken under the microscope: Fig.5.8 is the overview of five channels part with 30X magnification taken from the top and side view, while Fig.5.9 is zoom-in image of the middle three channels with 200X magnification form side view taken from left to right. The resolutions of these two magnifications are about 16.1

μm/pixel for one 30X low-resolution lens and 0.6267 μm/pixel for one 200X high-resolution lens. Fig.5.10 shows the length measurements of this specimen by caliper before and after stamping test, about 0.38 mm reduction in length.

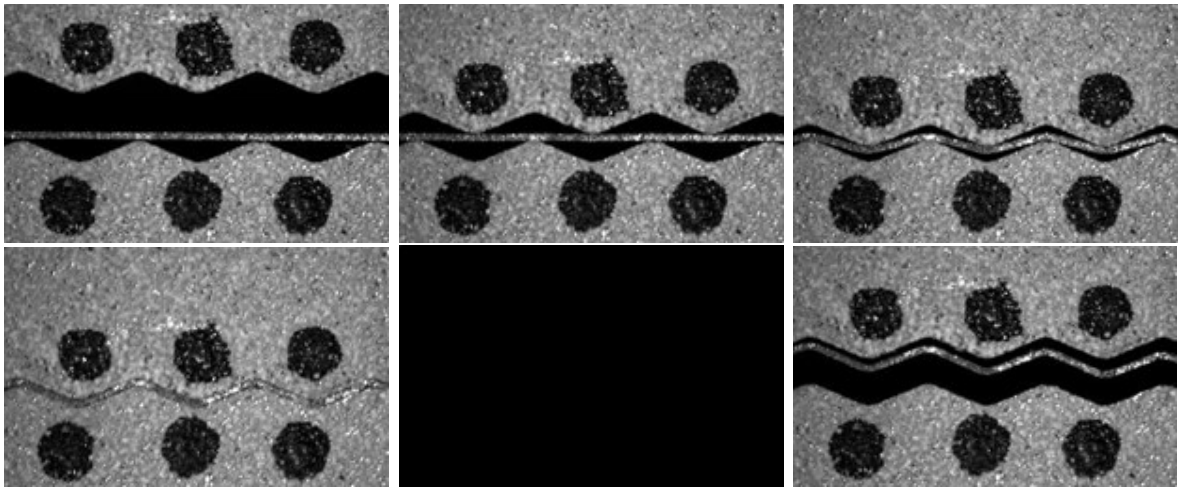

Figure 5.6: Continuously recorded images with preform set and max load is 400 N/mm.

5.4 Finite Element Analysis of Micro Channel Forming

Two-dimensional finite element analysis (FEA) with preform forming toolset was carried out using ANSYS Mechanical (APDL) in this section. For performed 2D simulations, foil model can be treated as a plane strain element behavior because specimen is sufficiently long comparing with its thickness (0.075 μm). Considering the running cost of simulations, half geometries of the test coupon and toolset were selected to simulate. Like the experimental setup, there is no contact surface between tool and simulated specimen at the initial setup. Per simulation, there are two steps introduced to mimic the loading part and the unloading part of one stage experiment: the first step is to apply load to the upper edge of punch to enforce foil specimen deform to a certain shape, and the second step is to release force by moving the punch back to the initial position. The general Hill's model for macroscopic

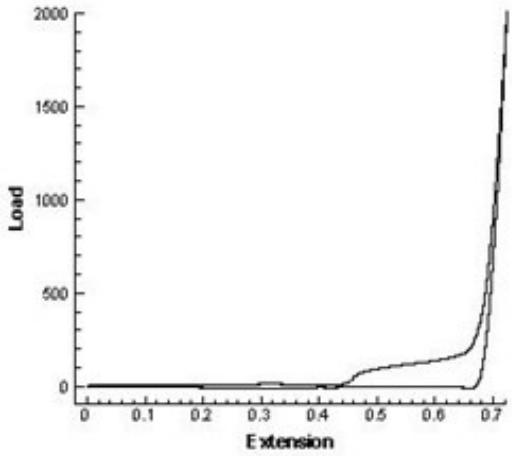

Figure 5.7: The extension versus load curve obtained from Instron.

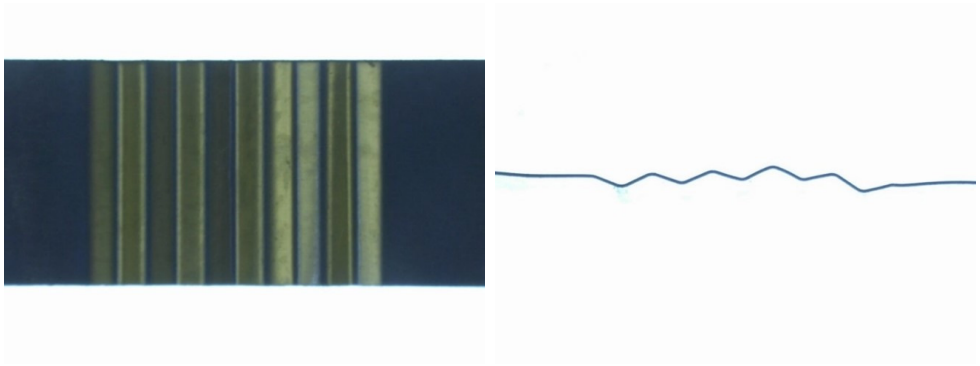

Figure 5.8: The images of test specimen profile of five repeated channels taken under digital microscope with a low-resolution lens : (a) left: top view and (b) right: side view.

plasticity and the modified Hill's model for polycrystal plasticity discussed in Chapter 4 were employed as foil's material model. Cubic and orthotropic plastic anisotropy of plastic potentials for polycrystals were assumed in the following simulation, which is presented in Chapter 4 and the previous studies [92, 93].

5.4.1 FEA Results Using Macroscopic Plasticity Model

In this section, several cases with preform forming toolset are included. To-be-simulated foil specimen is treated as a single crystal using the general Hill's model presented in Chapter

Figure 5.9: The images of test specimen side view profile of the middle three channels taken under digital microscope with a high-resolution lens (from left to right: the second channel to the fourth channel).

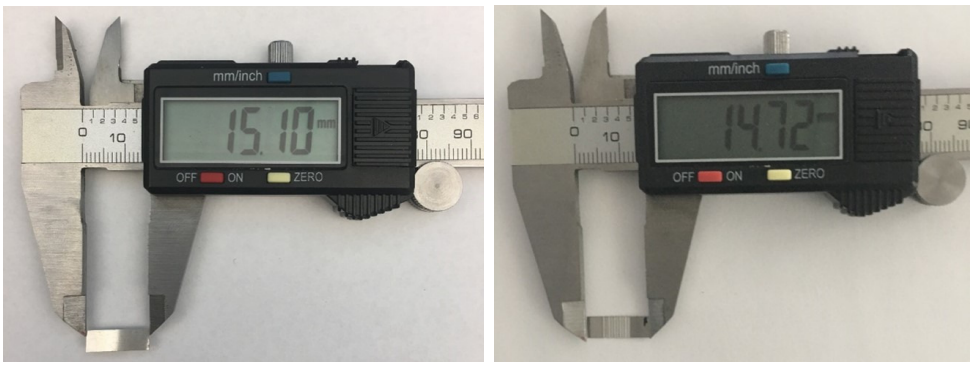

Figure 5.10: Length Measurements by caliper : (a) left : before the test and (b) right : after the test.

4 calibrated by tensile test. That is, one set of ANSYS input parameters of Hill's model was used in this type of simulation for all elements. The initial geometry of the meshed foil is 3.8 mm $\times$ 0.075 mm rectangular area. The micrograph of the in-plane cross-section shows that there are 7 or 8 grains distributed through thickness. Hence, the foil model with few elements (6 or more elements) distribute along thickness is sufficient for simulation purposes. There are two different mesh sizes in this area: 6 elements and 10 elements distributed through 0.075mm thick foil, the corresponding size per element represents 12.5 μm and 7.5 μm, respectively. The mesh size of elastic elements used in the forming toolset part was multiple times larger than the foil's element size. There are four strain hardening rules which interpret the relationship between true plastic strain and true stress shown in Fig.5.11. For simulated cases with 10 elements distributed through thickness of foil part (single layer model), one

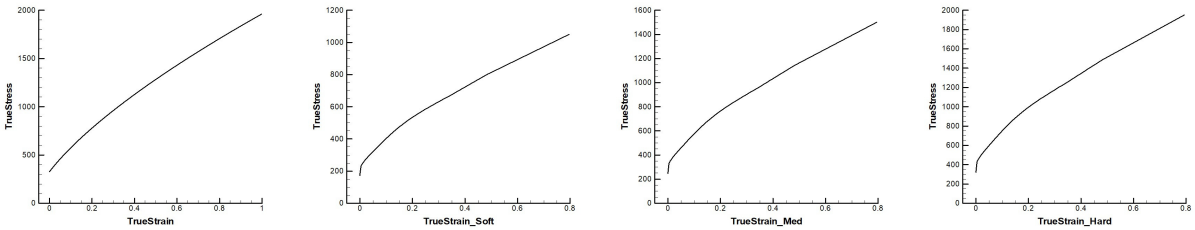

Figure 5.11: True stress versus true plastic strain of strain hardening rule : (a) SS1; (b) SS2; (c) SS3; (d) SS4 (from left to right).

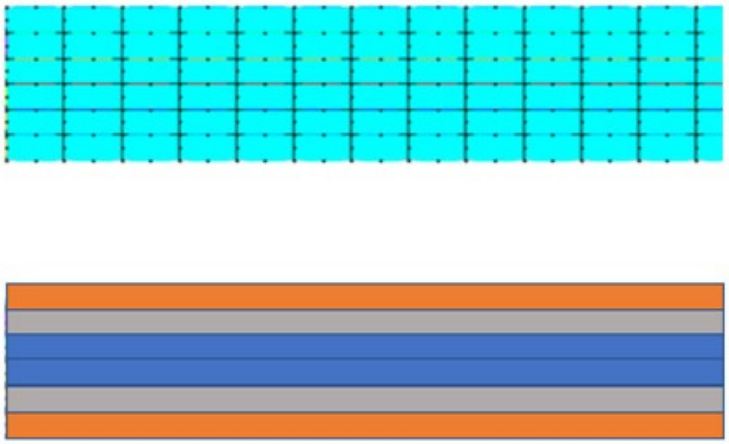

Figure 5.12: Six-layer setup of foil : 1) orange zone : soft plastic strain hardening rule (SS2), 2) gray zone : medium plastic strain hardening rule (SS3), and 3) blue zone: hard plastic strain hardening rule (SS4).

strain-hardening rule SS1 was employed for all foil elements. One or three strain-hardening laws were employed with the cases using 6 elements through thickness of foil part in the simulation, the meshed foil was also considered as a six-layer model (see Fig.5.12). Each layer can be classified as the outer, middle, and inner layer by its vertical location. The outer layer (orange layer) is the layer where will have direct contact with either punch or lower die has a softer plastic strain hardening rule (SS2), while the inner layer (blue layer) will have the most harder plastic strain hardening rule (SS4). The convergence criteria in displacement and force were customized, which is much smaller than the default of ANSYS,

about 0.001, and Possion's ratio was 0.3. To check effects of Young's modulus and coefficient of friction (CoF) between tool and specimen, there are two different values imposed in the simulations. The displacement was applied to the top line of punch in order to achieve certain load levels in FEA to match experimental load level. Except that, all other boundary conditions employed in simulations of this part were the same: left boundary lines of upper punch, foil sample and lower die were fixed in the horizontal direction, the bottom line of the lower die was fixed.

Here, preform forming toolset with the max load is 400 N/mm is considered in the simulations, and the detailed geometry information is presented in Table 5.1. The information about the setup of each one-stage forming simulation is listed in Table 5.3. An example of the associated setup in ANSYS using preform tool before each run is displayed in Fig.5.13.

Table 5.3: One-stage simulation with preform forming tool (P2)

FEA Case	Plastic Strian Hardening Type	No. Element Through Thickness	CoF	Young's Module (GPa)	Applied Displacement (mm)
P2a	SS1	10	0.18	200	0.5250
P2b	SS1	10	0.40	200	0.5250
P2c	SS3	6	0.40	200	0.5250
P2d	SS2,3,4	6	0.40	200	0.5250
P2e	SS2,3,4	6	0.40	150	0.5250

As shown in Table 5.3, some selected representative simulations with different material parameters are introduced. One typical single layer (P2c) and 6-layer (P2d) simulation case using preform tool are presented, the contour plots of deformed foil at max load (around 400 N/mm) and after releasing load are shown in Fig.5.14 and Fig.5.16. Fig.5.15 and Fig.5.17 display stress and elastic strain distribution within punch and lower die at two loading statues.

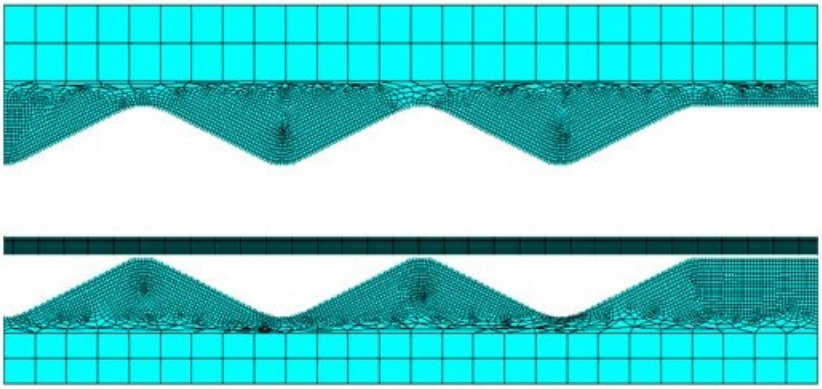

Figure 5.13: Simulation setup with preform set.

5.4.2 FEA Results Using Polycrystal Plasticity Model

As detailed in Chapter 4, entire polycrystalline SS304L thin foil in a channel forming process will be modeled with detailed grain structures. That is, the slip potential for multi slips in each single grain is represented by an analytical stress function such as a quadratic polynomial with cubic or orthotropic plastic anisotropy in the local crystallographic axes, and the slip strength of the crystal is represented by an isotropic slip hardening model. In this section, grain structure of foil is presented via a Voronoi tessellation. In material science, a Voronoi tessellation represents polycrystal microstructures in metal alloys, such as stainless steel. The morphology of each crystal is convex, ununiform, and exhibits randomness. These characters are highly governed by distributing many points (also called seeds) in the plane and the proximity between each two-point. To generate two-dimensional grain geometries, a software called Neper was used to create a random distribution of seeds that represents grains fitting in a specified area. Neper is a powerful package developed by Romain Quey at CNRS and MINES Saint-Etienne used for polycrystal generation and meshing [121, 122]. In Neper, it also provides a way to define a set of parameters of a microstructure model, such as number of grains, dimensions, the space of tessellation, aspect ratio, grain orientation, etc. The Voronoi tessellation and grain orientation provided by electron back-scattering diffraction (EBSD) technique were employed to reconstruct grain microstructures. To check effects caused by geometric morphology and randomness of microstructure, five random

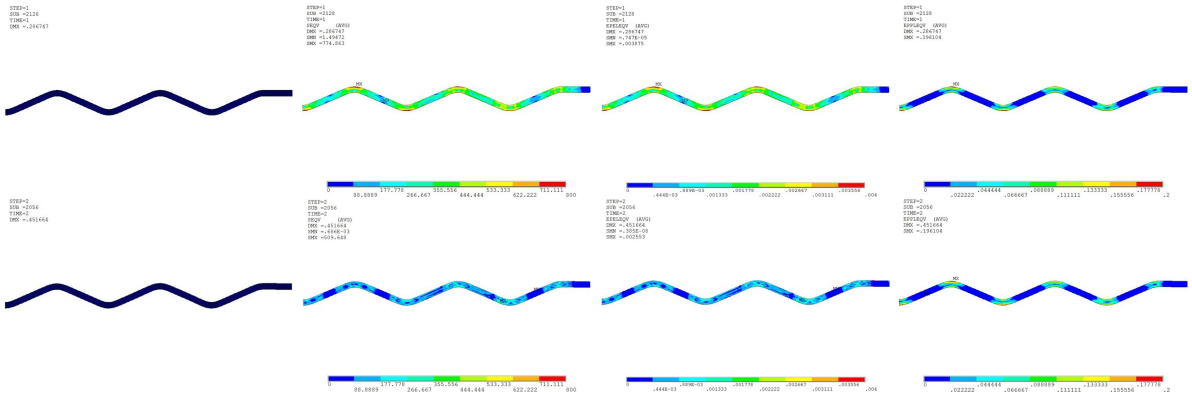

Figure 5.14: Case P2c foil result (single layer model): 1st line (at max load): (a) deformed foil, (b) von Mises stress distribution, (c) von Mises elastic strain distribution, (d) von Mises plastic strain distribution ; 2nd line (after releasing the load): (e) deformed foil, (f) von Mises stress distribution, (g) von Mises elastic strain distribution, (h) von Mises plastic strain distribution (from left to right).

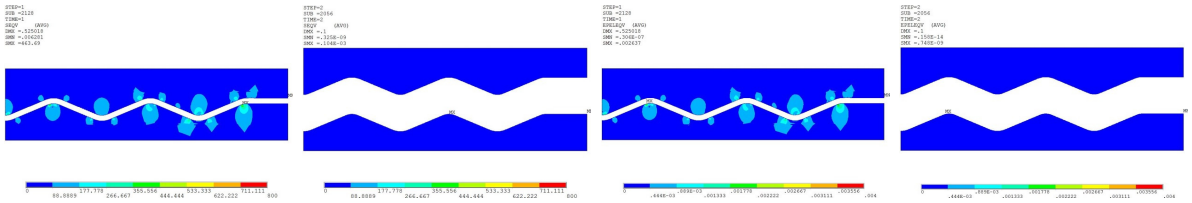

Figure 5.15: Case P2c tool result (single layer model): (a) and (b) are von Mises stress distribution at the max load and after releasing the load; (c) and (d) are von Mises elastic strain distribution at the max load and after releasing the load (from left to right).

two-dimensional Voronoi diagrams sharing the same code were generated via Neper and are displayed in Fig.5.18. The associate Voronoi diagrams regenerated in ANSYS based on the output of Neper are depicted in Fig.5.19.

A 3.8 mm $\times$ 0.075 mm rectangular area with an aspect ratio per grain is 10:7 was used to present the foil part: each element in the area is considered as a single crystal or grain. The total number of grains presented foil in Fig.5.19 is three times of the total number of grains from EBSD data, about 6090 grains in total. The average element number through thickness of foil is about 12 (6.25 μm per element), the randomness of texture leads to distribution

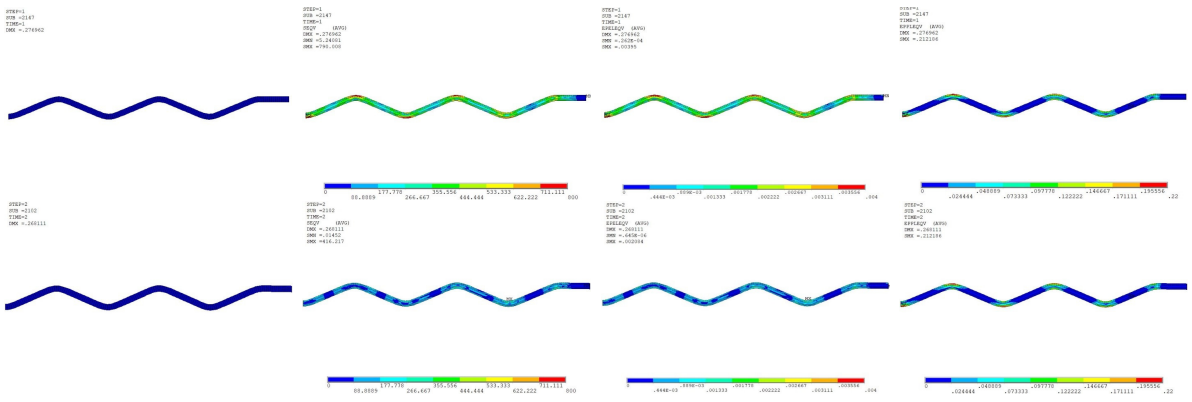

Figure 5.16: Case P2d foil result (6-layer model): 1st line (at max load): (a) deformed foil, (b) von Mises stress distribution, (c) von Mises elastic strain distribution, (d) von Mises plastic strain distribution ; 2nd line (after releasing the load): (e) deformed foil, (f) von Mises stress distribution, (g) von Mises elastic strain distribution, (h) von Mises plastic strain distribution (from left to right).

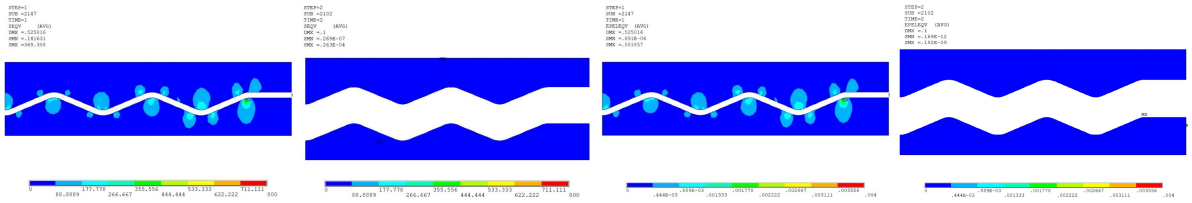

Figure 5.17: Case P2d tool result (6-layer model): (a) and (b) are von Mises stress distribution at the max load and after releasing the load; (c) and (d) are von Mises elastic strain distribution at the max load and after releasing the load (from left to right).

difference of elements along thickness by its location. Like macroscopic simulations, there are two mesh sizes for punch and lower die about 2 and 10 times of the average size of foil. Each grain was assigned with a unique Hill's model parameters calibrated via Bunge Euler angles of SS304L obtained from EBSD texture data. The strain hardening curve used for each grain (SS5) was scaled based on the strain hardening law (SS3) of Fig.5.11(c) with a factor is $\frac{1}{\sqrt{1.732}}$ for strain and $\sqrt{1.732}$ for stress, as shown in Fig.5.20. The same boundary conditions discussed in Section 5.4.1 were applied to all cases with cubic plastic anisotropy in this part, all slip system weights for this anisotropy equal to 1. The convergence criterion for

Figure 5.18: Two-dimensional 6090 grains Voronoi diagram created via Neper, the domain size is 3.8 mm × 0.075 mm with aspect ratio is 10:7 and the orientation of fiber is along horizontal direction (from top to bottom : Set 1 to Set 5).

displacement and force was 0.001, Young's modulus was 200 GPa, and Possion's ratio was 0.3 for all cases. CoF used in the simulation between punch/lower die and foil was 0.4, which is obtained from some SS304L friction tests. The initial setup of punch/lower die used in this type of simulations is the same as shown in the previous section, while foil part was replaced by microstructure model displayed in Fig.5.19, and the associate simulation information is listed in Table 5.4. For the case (P2k) imposed with orthotropic plastic anisotropy per grain, the displacement applied at the top of punch is different to meet the max load of experiments. Three independent slip system weights are introduced as $w_1 = 2.54498$, $w_2 = 1.27130$ and $w_3 = 0.87292$, the remaining slip system weights could be expressed in terms of these three weights. As the result of the fourth Voronoi diagram as foil is the most closely match to the average of five cases with cubic plastic anisotropy, this typical set is used as a representative case for orthotropic plastic anisotropy modeling.

The associated plots of ANSYS for polycrystal simulation using preform tool and the first Voronoi diagram set as meshed foil are shown in Fig.5.21. In this simulation, the max load reached is about 400 N/mm, which replicates the same load level obtained from experiments. Fig.5.22 focus on the corresponding localized results (left edge) of the foil of Fig.5.21, while

Figure 5.19: The corresponding foil model consists of 6090 grains in ANSYS (from top to bottom : Set 1 to Set 5).

Table 5.4: 6090 grains one-stage simulation with preform tool

FEA Case	Microst-ructure	Plastic Strian Hardening Type	No. Element Through Thickness	CoF	Young's Module (GPa)	Applied Displacement (mm)
P2f	1^{st} Set	SS5	12	0.40	200	0.5250
P2g	2^{nd} Set	SS5	12	0.40	200	0.5250
P2h	3^{rd} Set	SS5	12	0.40	200	0.5250
P2i	4^{th} Set	SS5	12	0.40	200	0.5250
P2j	5^{th} Set	SS5	12	0.40	200	0.5250
P2k	4^{th} Set	SS5	12	0.40	200	0.5254

Fig.5.23 displays stress and elastic strain distribution within punch and lower die at the max load and after load releases. The localized foil results of Fig.5.21 show that different grain indeed has different stress and strain responses, and it will affect the springback behaviors eventually.

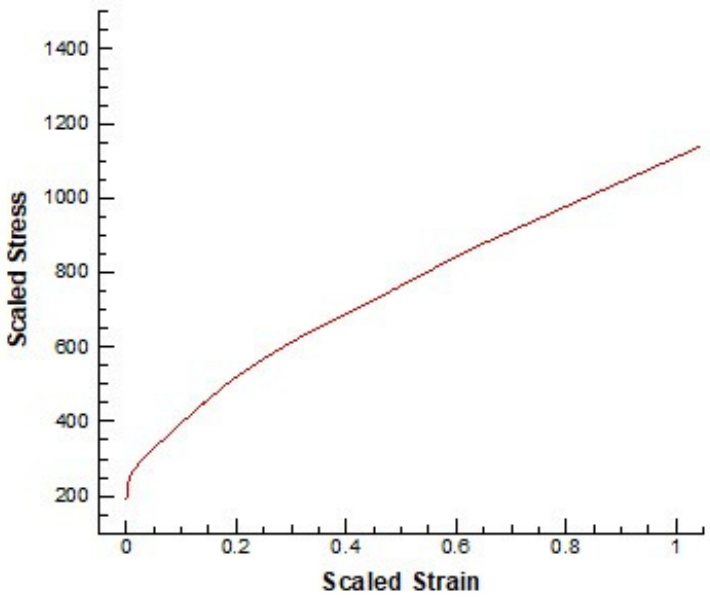

Figure 5.20: The scaled stress-strain hardening law (SS5) base on SS3 with certain scale factor.

5.5 Springback Sensitivity Study of Micro Channel Forming Operations

Springback is a material behavior that refers to the release of elastic deformation after working load removes [22,29,119]. In this study, bending the specimens with tension force was employed to decrease springback effects on shape forming. Studying springback responses of experimental and computational results helps to understand material behaviors better and have reasonable predictions.

5.5.1 Definition for Springback Measurement

In recent studies, there are several options to describe springback measurement for either experimental or computational test: height reduction of the channel (peak to valley) [123] and springback angle [124, 125]. Because it is difficult to pin down the start point and the endpoint of the channel part, length measurement is not a measurement option to evaluate the springback behaviors in this study. As illustrated in the previous section, there are five repeated and identical profiles of the channel forming part used in experiments and

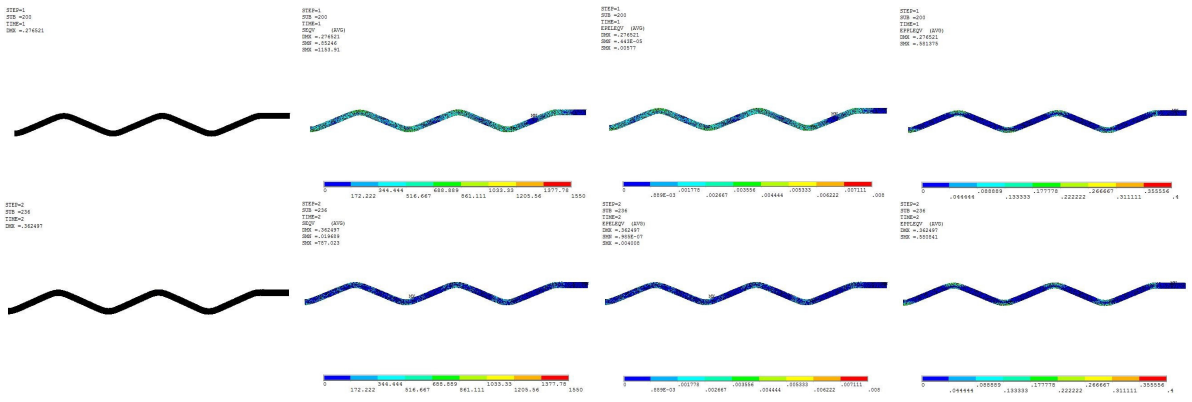

Figure 5.21: Case P2f foil result (the first Voronoi diagram set used) : 1st line (at max load): (a) deformed foil, (b) von Mises stress distribution, (c) von Mises elastic strain distribution, (d) von Mises plastic strain distribution; 2nd line (after releasing the load): (e) deformed foil, (f) von Mises stress distribution, (g) von Mises elastic strain distribution, (h) von Mises plastic strain distribution (from left to right).

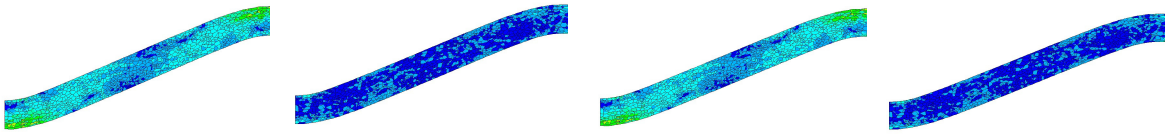

Figure 5.22: Case P2f localized foil result (the first Voronoi diagram set used, left edge) : (a) and (b) are von Mises stress distribution at the max load and after releasing the load; (c) and (d) are von Mises elastic strain distribution at the max load and after releasing the load (from left to right).

two and half of the same profiles simulated in FEA. In this study, two approaches were employed to evaluate springback: local measurement and global measurement. The first method is to measure changes in height and bended angle channel by channel or half channel by half channel, while the second method is to consider five channels as a whole piece and check the average changes at the center and the end of the foil. The measurements were achieved by using a software called ImageJ, which is a powerful open-source Java-based image processing program developed at the National Institutes of Health and University of Wisconsin [126, 127].

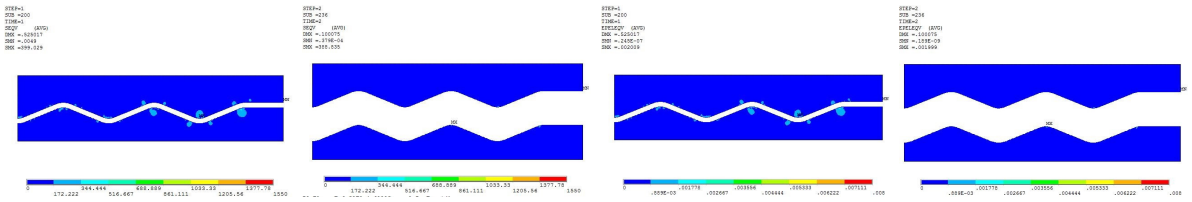

Figure 5.23: Case P2f tool result (the first Voronoi diagram set used) : (a) and (b) are von Mises stress distribution at the max load and after releasing the load; (c) and (d) are von Mises elastic strain distribution at the max load and after releasing the load (from left to right).

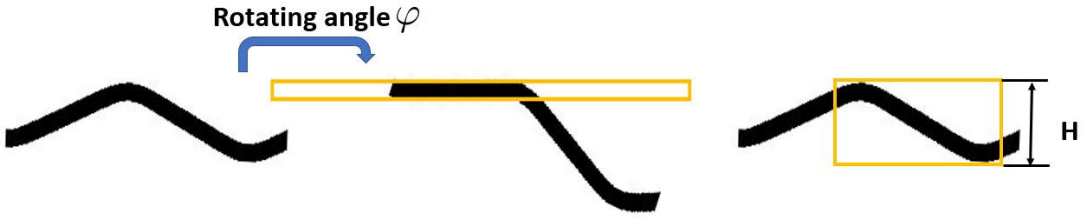

Figure 5.24: Schematic drawing of local springback measurement : (a) captured foil image after removing load; (b) rotated captured image (rotating image in ImageJ); (c) foil height measurement based on captured image (from left to right).

For local measurement, the schematic drawing shows how to define height and rotating angle in Fig.5.24. Here, φ is a rotated angle that obtains by rotating the captured images either from experiments or simulations to aligned with the edge of a reference box drawn in ImageJ, and the springback angle $\triangle\varphi$ is relevant to the difference between the rotated angle of punch or lower die and the rotated angle of deformed foil, as shown in following

$$\triangle\varphi = \varphi_d - \varphi_f, \tag{5.2}$$

where φ_d is the rotated angle by rotating punch or lower die to match the drawn reference box, φ_f is the rotated angle by rotating deformed foil specimen after removing loads to match the drawn reference box, and $\triangle\varphi > 0$. The reduction in height of the channel profile part between the punch or lower die and a deformed foil specimen reflects height change

from peak to valley of the profile shown in Fig.5.24(c), the expression for calculating height change is

$$\triangle H = H_d - H_f, \tag{5.3}$$

where H_d is the height of punch or lower die (peak to valley), H_f is the height of deformed foil (peak to valley), $\triangle H$ is height reduction between these two heights with $\triangle H > 0$.

Focusing on springback prediction per channel or half channel, it may be easier to lead to a scatter result, global measurement is introduced to get a more consistent result case by case. Due to the limits of lab equipment, the images taken under microscopic or captured from FEA were stitched side by side before further analysis and displayed in Fig.5.25. The edges of forming tools or foil specimens were detected using edge detection function of ImageJ, and the images need to be rotated to keep the end of the edge horizontal before overlapping these two images (see Fig.5.26). The overlapped image of forming tool and foil sample is aligned at the valley of central channel (the third channel counted from left). The same procedures for measuring height and angle were carried out for global measurements.

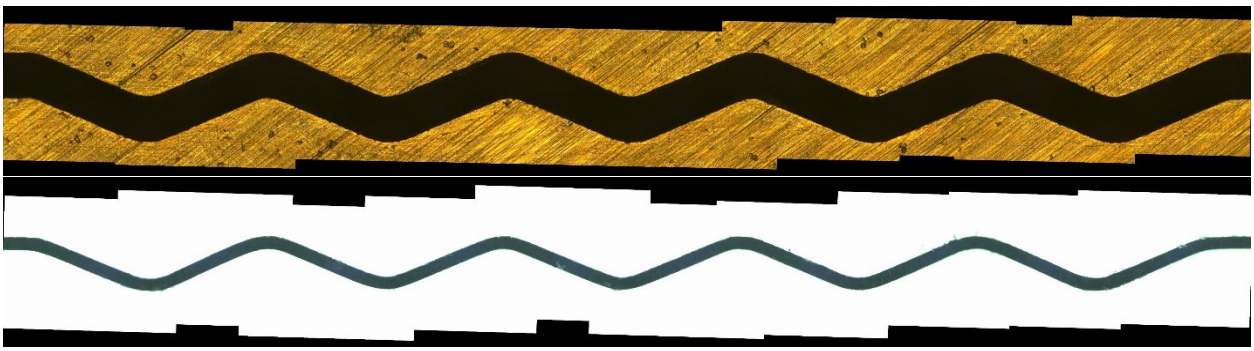

Figure 5.25: Stitched microscopic images : (a) preform forming tool (P2) and (b) deformed foil (from top to bottom).

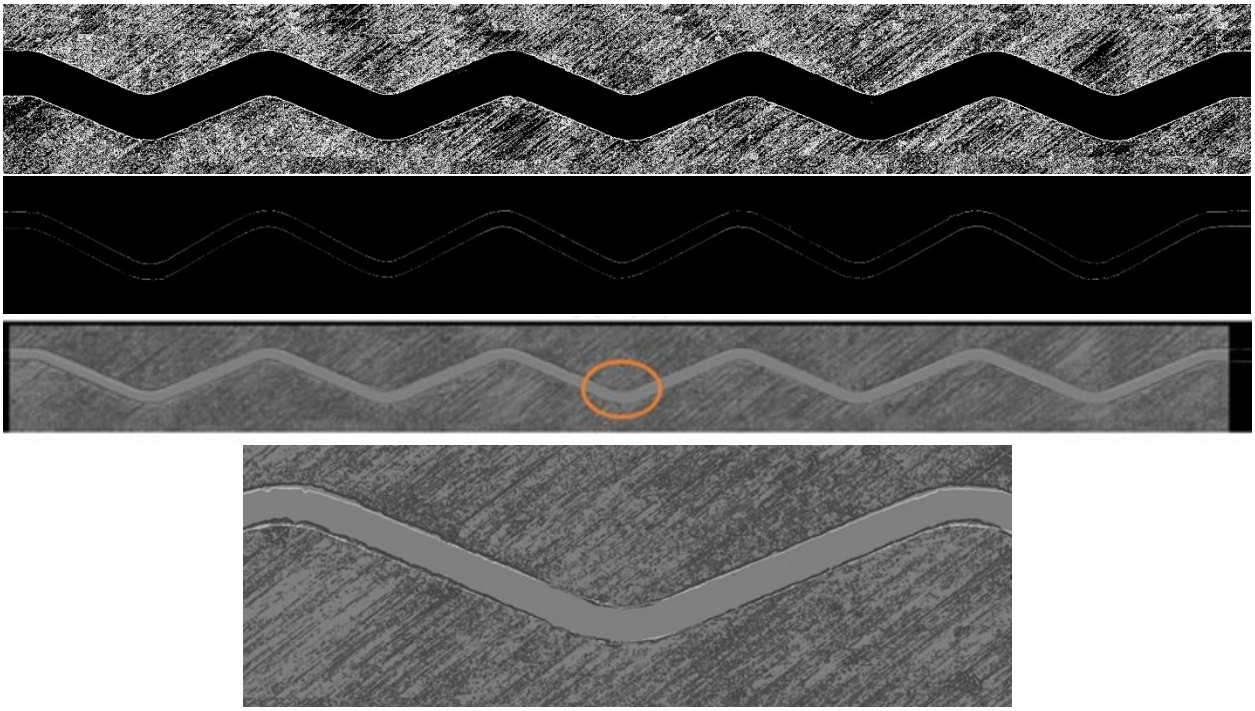

Figure 5.26: Edge profile images: (a) profile of preform forming tool (P2); (b) profile of deformed foil; (c) overlapped image of preform tool and deformed foil aligned at center (marked with open circle); (d) enlarged profile of middle channel of overlapped image: white line is deformed foil, black line is preform tool (from top to bottom).

5.5.2 Results and Discussions

As shown in Table 5.2, tests were carried out in the experiments with max load is 400 N/mm (2000N, 5mm width). The max load, the average values of height reduction and springback angle using local and global measurement methods are listed in Table 5.5. In this table, the superscript L refers to the local measurement method and G is the measurement using the global method, and subscript E represents the results obtained from experiments.

Table 5.5: Springback measurement based on experimental images

Max Load (N/mm)	$\triangle H_{\mathrm{E}}^{\mathrm{L}}$ (μm)	$\triangle \varphi_{\mathrm{E}}^{\mathrm{L}}$ (°)	$\triangle H_{\mathrm{E}}^{\mathrm{G}}$ (μm)	$\triangle \varphi_{\mathrm{E}}^{\mathrm{G}}$ (°)
400	4.20	1.56	6.97	1.08

The springback measurement results of FEA cases listed in Table 5.3 for macroscopic plasticity model and in Table 5.4 for crystal plasticity model with cubic and orthotropic plastic anisotropy are shown in Table 5.6, where subscript F represents the results of simulations, the superscript L refers to local measurement method and G is the measurement using global method. Here, all values are average value based on all channels. The average max plastic strain of foil reached in the simulations is about 0.3 for the macroscopic case and 0.4 for the microscopic case.

Table 5.6: Springback measurement based on FEA results

Case	Max Load (N/mm)	$\triangle H_{\mathrm{F}}^{\mathrm{L}}$ (μm)	$\triangle \varphi_{\mathrm{F}}^{\mathrm{L}}$ ($^{\mathrm{o}}$)	$\triangle H_{\mathrm{F}}^{\mathrm{G}}$ (μm)	$\triangle \varphi_{\mathrm{F}}^{\mathrm{G}}$ ($^{\mathrm{o}}$)
P2a	411	3.780	0.816	6.259	0.200
P2b	399	4.298	0.796	7.821	0.800
P2c	389	4.358	0.840	8.598	0.460
P2d	413	3.725	0.840	7.813	0.400
P2e	366	2.638	0.920	4.688	0.250
P2f	399	3.773	0.950	10.938	0.800
P2g	409	3.591	1.160	6.250	0.900
P2h	399	3.591	0.880	6.250	0.860
P2i	402	3.010	1.080	7.813	0.860
P2j	405	3.700	0.960	8.598	0.700
P2k	393	2.870	0.760	7.143	0.800

From Table 5.3 and Table 5.4, Young's modulus, CoF, and strain hardening for macroscopic model and grain heterogeneity distribution and plastic anisotropic type for polycrystal model are considered as factors that affect the results of springback behavior in this study. Except for the factors mentioned, the max load reached, loading condition applied at the top of punch (displacement control or pressure control), channel profile and test procedures are changeable variables that are not taken into consideration this time.

5.5.2.1 Effect of Contact Friction

Contact friction is an important but not very well known factor that affect springback predictions. As results shown in Table 5.6, Case P2a and P2b are two cases with the same simulation setup, except CoF is 0.18 for Case P2a and 0.4 for Case P2b. For local springback measurement, P2b shows a larger reduction in height and two cases have similar springback angles. However, P2b has larger changes on both height and springback angle for global measurement. The inconsistency between local and global method may be due to deformed foil is curved as a whole piece displayed in Fig.5.16, especially affecting the height reduction measurement for local ones. The force response has been revealed to slight change with the same conditions except for different CoF used in the simulations, this situation could be assumed that both cases have same max load. With the same max load and higher CoF employed, it is harder to deform foil to the desired shape like the one with lower CoF. That is, the elastic-recoverable deformation takes a more leading proportion with the increase of CoF, more height reduction and larger springback angle.

5.5.2.2 Effect of Strain Hardening

Strain hardening is related to plastic deformation of material, P2c is considered as one layer with only one strain hardening law used and P2d is a six-layer case with different strain hardening law employed. Here, the strain hardening law for one layer case is the same as the law used in the inner layer of the six-layer case. The thickness of each layer in the six-layer model is identical. The max load reached and the reduction in height in Table 5.6 show a significant difference. For springback angle, there is no difference using local measurement methods and a small difference for global one. The yield strength of the outer layers is lower than the middle and inner layer and further from the neutral layer during the test, so they are subjected to the stronger either tensile or compression stresses. As a result, the effect of the outer layer for springback behavior is even more significant. With a soft outer layer, it is easier to deform permanently. Hence, less height reduction and smaller springback angle occur with a softer strain-hardening law used as the outer layer.

5.5.2.3 Effect of Young's Modulus

Using the same other simulated conditions, the only difference introduced in Case P2d and P2e is Young's modulus with P2d is 200GPa and P2e is 150GPa. The results included in Table 5.6 indicate that the increase of max load with Young's modulus decreases, height reduction for global method and springback angle for global and local method are very close. The height measurement via the local method is different, which may be due to the curved profile of foil. Young's modulus of a material is the stiffness that reflects the easiness for bending and stretching. With the same displacement applied, high Young's modulus needs more force than the lower one, as verified in the simulation. In this simulated setup, changing Young's modulus shows barely any effect on height and springback angle measurements.

5.5.2.4 Effect of Grain Heterogeneity Distribution

Specimens with different random grain heterogeneity distribution are shown in Fig.5.18, the results of Table 5.6 illustrate that grain heterogeneity distribution for polycrystal simulation affects the height reduction and springback angle straightforwardly. Due to the random assignment of grain mechanical properties, various grain heterogeneity distribution leads to different load responses, height reductions and measured springback angles. For spring angle measurement either via local or global measuring methods, values of five cases are very close. However, results on height reduction are more scattered. From the previous study [124], it is noticeable that the scatter effect will be minimized by averaging. One set in FEA will result in uncertainty of grain distributions because the material model is randomly assigned to the grain. Therefore, the average of max load is 402.8 N/mm. For local measurement method, the average of height $\triangle H_{\mathrm{F}}^{\mathrm{L}}$ is 3.533 μm and springback angle $\triangle \varphi_{\mathrm{F}}^{\mathrm{L}}$ is 1.006°, while average of height $\triangle H_{\mathrm{F}}^{\mathrm{G}}$ and springback angle $\triangle \varphi_{\mathrm{F}}^{\mathrm{G}}$ are 7.970 μm and 0.824° for global method. Compared with the average values, P2i is the case with the results are the closest to the average values of five cases. For polycrystalline simulation, grain heterogeneity distribution is one of the factors should be considered for the scatter of springback predictions, except the factors introduced for macroscopic model.

5.5.2.5 Effect of Plastic Anisotropic Type

As discussion about plastic anisotropy in Section 4.3.3, orthotropic plastic anisotropy has three undetermined material constants, which has more flexibility than cubic anisotropy with only one material constant is needed to be known and equals to 1. Different displacements (Case P2i and P2k) were applied to guarantee the max load of FEA is approximate to experimental max load. The results indicate that grain plastic anisotropic type imposed affects the prediction on springback, height reduction and change of springback angle decrease as imposing orthotropic plastic anisotropy instead of cubic plastic anisotropy per grain. Different plastic anisotropic types may also affect the estimation of R-values and yield strength. Therefore, the plastic anisotropic type of polycrystals is another factor should be taken into consideration on springback predictions for polycrystal cases.

5.5.2.6 Discussions

According to Table 5.6, the results of springback measurement show that CoF and strain hardening have clearly effects, however, the effect of Young's modulus is small in this study. Proposed by Zang et al. [128] and Adzima et al. [123], Young's modulus is not a constant value: larger springback prediction will occur if the decrease of Young's modulus was taken into account. With large plastic strain achieved, the curved region of either peak or valley of foil is dominated by plastic deformation and influences springback predictions [129]. Therefore, Young's modulus will have less effect on the predictions. As discussed in the previous part, the decrease of CoF and the change of strain hardening law (softer one as the outer layer, harder one as inner layer) in the layered model will result less height reduction and smaller springback angle. As two measurement methods were introduced to estimate springback predictions, the global one is more reliable by eliminating scatters between channels caused by the curved profile of foil. Case P2b has the largest height reduction and springback angle within the macroscopic approach, while the smallest springback angle is obtained in P2a, and P2e has the smallest height reduction. For polycrystal simulated cases, grain heterogeneity distribution and plastic anisotropic type of grains are two additional main factor affecting springback predictions. Using EBSD and Voronoi tessellation, this approach represents grain size, shape, and the associated mechanical proprieties obtained by

introducing micromechanical continuum crystal plasticity theory with cubic and orthotropic plastic anisotropy. Comparing these two simulation approaches, the results of polycrystal simulations show larger height reduction and springback angle. It concludes that if information about the microtexture of material is available, using the polycrystal plasticity model to mimic forming process is a better choice when the time-consuming is relatively less.

The global measurement method gives more consistent and reliable results and attempt to validate experiments by using current simulated approaches, experimental result is 6.97 μm for height reduction and 1.08^{o} for springback angle. For simulated results, the height reduction is 7.821 μm and the springback angle is 0.800^{o} for the macroscopic model (P2b), while the average height reduction is 7.970 μm and the average springback angle is 0.824^{o} for polycrystal cases with cubic plastic anisotropy. Against the peak load obtained in experiments, these computational cases replicate experimental test conditions with the max load is around 400 N/mm. From the results, it can be observed that the simulation underestimates springback angle and overestimated height reduction, it may relate to the residual cold-working effect of test specimen that affect springback behaviors or measurement errors introduced by low resolution of the output image for simulated cases. In addition, stress distribution, the change of Young's modulus during simulations, and different strain hardening per grain may also be the factors that affect springback behaviors as well. Additional work is needed to understand both macroscopic and crystal scale springback behavior completely.

5.6 Conclusions

Micro channel forming tests using designed tools and ultra-thin SS304L foil as specimen were carried out with Instron 5967 testing system at room temperature, and peak load is reached by using load control mode during loading step, about 2000 N. The corresponding simulations are examined by two approaches: macroscopic plasticity model that foils treated as a single crystal and microscopic plasticity model for polycrystal that each element treated as a single crystal. For polycrystal simulated cases, a reduced orientation data extracted from the original EBSD has been used as the input data for the microstructural modeling including 6090 representative grains. The shape and location of these representative grains were defined based on the Voronoi tessellation generated by Neper. The difference in grain

heterogeneity distribution leads to a slight difference response which is expected. As the peak load achieved in the experiments, these two computational approaches replicate experimental results. By comparing numerical and experimental results, two approaches for simulation were able to describe contact friction, strain hardening, grain heterogeneity distribution and plastic anisotropy type effects on the springback behaviors under micro channel forming.

Chapter 6
SUMMARY AND FUTURE WORK

6.1 Summary

The research in this dissertation has focused on anisotropic plasticity modeling of thin aluminum AA6111-T4 sheet metals and ultrathin 304L stainless steel foils and their applications in sheet metal forming simulations using finite elements. The anisotropic plastic flow of thin sheet metal is often characterized by plastic strain ratios determined in a series of uniaxial tensile tests with angles between the tensile loading axis and the rolling direction of the sheet metal ranging from 0 to 90 degrees. Existing experimental methods used to measure the plastic strain ratios in common practice are briefly reviewed and a new approach using a digital image-based full-field strain mapping technique and associated camera calibration is introduced in Chapter 2. Potential sources of errors in both old and new methods are discussed, emphasizing achieving the best precision and accuracy in plastic strain ratio values. Some theoretical results relating the anisotropic plasticity models to the plastic strain ratios are included as well. It evaluates the impact of eliminating the elastic strain in the unloaded state to check the possible improvement in the consistency of R-value measurements at different angles and the effect of defective samples on the error values of R.

Two formulations of a fourth-order orthotropic yield function in plane stress, Gotoh's complete fourth-order polynomial function with nine coefficients and the popular Yld2000-2d function with a stress exponent of 4 and eight material constants, have been evaluated in Chapter 3. Calibrated with the same independent experimental inputs, the similarities and differences of these two formulations of a sheet metal modeling are investigated: these two expressions are shown to be identical for an in-plane isotropic sheet metal, and material constants of Yld2000-2d function are not unique. For any on-axis biaxial loading, Yld2000-2d function may fully match the capability of Gotoh's yield function. With seven or eight

independent inputs are used to identify parameters of these two functions with reduced plastic anisotropy, Yld2000-2d function may be made to closely approximate match to the calibrated Gotoh's function and used as an effective convexification method for calibrating a non-convex fourth-order polynomial function.

The relevant quadratic plastic potentials of FCC single crystals and texture components are investigated in Chapter 4 to assess the effects of crystallographic slips in crystal plasticity on the formulation of a macroscopic plastic potential for an FCC polycrystalline material. By their equivalency, the number and type of independent material constants have been identified for six specific cases of plastic anisotropy. A simplified rate-independent continuum crystal plasticity model is used to model the polycrystalline SS304L ultra-thin foils. That is, an isotropic slip hardening model represents the slip strength of the crystal. Simultaneously, a convex quadratic plastic potential in the local crystallographic axes is assumed to be the slip potential for multi-slips in each FCC single crystal. There are three polycrystal models that could be used to calibrate three independent parameters of a single crystal plasticity model with orthotropic plastic anisotropy using EBSD texture data and the plastic strain ratios obtained from uniaxial tensile tests via DIC. The simulation results of a representative volume element model using calibrated ANSYS input parameters obtained via EBSD data and estimated parameters via Sachs or Taylor model as initial guesses show the validation of this micro-to-macro transition method. To closely match with the plastic strain ratios (R_0 and R_{90}) measured from experiments, the single crystal plasticity model with orthotropic plastic anisotropy should be used with three independent slip system weights are $w_1 = 2.54498$, $w_2 = 1.27130$ and $w_3 = 0.87292$.

Experimental investigations and computational simulations have been carried out in Chapter 5 to evaluate the springback behaviors of formed SS304L micro channels. Micro channel forming tests of SS304L foils have been carried out with an Instron materials testing machine and designed preform forming tools at room temperature. The corresponding numerical simulations are examined by two anisotropic plasticity modeling approaches: the macroscopic plasticity model in which foils are treated as a homogeneous featureless continuum and polycrystal plasticity model in which individual single crystal grains with various orientations are explicitly modeled. Compared with the peak load achieved in the

experiments, these two computational methods replicate the experiments' results. The polycrystal simulations using EBSD microtexture data and a calibrated single crystal plasticity model give a better springback prediction of measured springback from experiments. The results of carried out simulations conclude that contact friction, strain hardening, grain heterogeneity distribution, and plastic anisotropic type have effects on micro channel forming and its springback behaviors.

6.2 Future Work

To obtain a more precise and accurate R-value via image-based measurements experimentally, potential errors caused by the relative out-of-plane motion of the test coupon from the stationary camera may be reduced or eliminated using two thin flat reference targets attached to a tensile coupon. By loosely holding two spray-painted thin flat steel squares as the reference targets at the two ends of the gage section of the test coupon using either rubber bands or small magnets, the virtual strains purely due to the possible out-of-plane motion of the tension coupon during testing can thus be continuously captured. The out-of-plane motion effect on both longitudinal and transverse axial strains of the gage section of the test coupon can then be corrected. The sole effect of non-homogeneous deformation during the initial stage of the tensile testing on the measured R-values can thus be more directly assessed.

The quadratic yield function for modeling an FCC single crystal can be extended to model a BCC single crystal, so the micro channel forming using ultrathin ferritic stainless steel 439 foils may be studied as well. Further more, both quadratic functions may be replaced by the quartic yield functions for higher degrees of plastic anisotropy. Additional uniaxial tensile experiments shall be carried out with three off-axis loading directions (22.5°, diagonal direction 45°, and 67.5°) and the more precise experimental measurements of R-values as described above. Because the enhanced modeling capabilities of a quartic yield function, both R-values and yield stresses from the experiments may be used for calibrating many more slip system weights. Macroscopic and polycrystal plasticity models using quartic plastic potentials will need to be implemented via a user material subroutine (UMAT) for finite element simulations of micro channel forming of ultrathin SS304Land SS439 foils.

The study about springback predictions of SS304L or SS439 foil under micro channel forming could be further improved from several aspects. First, an elastic-hysteresis model could be developed for more precisely analyzing the unloading behaviors. Second, finite element simulations of micro channel forming could be carried out using different sets of various punch and lower die at several load levels and test procedures (such as two-stage forming with preform set as the first stage, conformal or non-conformal set as the second stage). With more advanced EBSD measurement tools, representative 3D microtexture data of a ultrathin foil could be obtained to help develop fully 3D finite element polycrystal models with measured grain sizes and shapes in addition to their orientations. Developing the 3D finite element polycrystal model of ultrathin stainless steel foils and analyzing their micro channel forming in a timely manner may need to migrate to a high performance computing (HPC) platform.

BIBLIOGRAPHY

[1] J. Cao and M. Banu, "Opportunities and challenges in metal forming for lightweighting: review and future work," *Journal of Manufacturing Science and Engineering*, vol. 142, no. 11, 2020. 1

[2] W. F. Hosford and J. L. Duncan, "Sheet metal forming: a review," *Jom*, vol. 51, no. 11, pp. 39–44, 1999. 1

[3] U. Dixit, S. Joshi, and J. P. Davim, "Incorporation of material behavior in modeling of metal forming and machining processes: A review," *Materials & Design*, vol. 32, no. 7, pp. 3655–3670, 2011. 1

[4] K. Lange, *Handbook of metal forming*, 1985. 1

[5] Y. Lim, R. Venugopal, and A. G. Ulsoy, "Advances in the control of sheet metal forming," *IFAC Proceedings Volumes*, vol. 41, no. 2, pp. 1875–1883, 2008. 1

[6] H. Palaniswamy, A. Yadav, S. Kaya, and T. Altan, "New technologies to form lightweight automotive components," in *Proceedings of 4th International Conference and Exhibition on Design and Manufacturing of Machines and Dies/Molds, June*, 2007, pp. 21–23. 1

[7] Z. Yu, Z. Lin, and Y. Zhao, "Evaluation of fracture limit in automotive aluminium alloy sheet forming," *Materials & design*, vol. 28, no. 1, pp. 203–207, 2007. 1

[8] R. Lapovok, I. Timokhina, P. W. J. McKenzie, and R. O'Donnell, "Processing and properties of ultrafine-grain aluminium alloy 6111 sheet," *Journal of materials processing technology*, vol. 200, no. 1-3, pp. 441–450, 2008. 1

[9] S. Golovashchenko, N. Reinberg, A. Hassannejadasl, and D. Green, "Hardening of a6111-t4 aluminum alloy at large strains and its effect on sheet forming operations," *Journal of Materials Engineering and Performance*, vol. 28, no. 4, pp. 2465–2476, 2019. 1

[10] Y. Shen, X. Li, X. Sun, Y. Wang, and L. Zuo, "Twinning and martensite in a 304 austenitic stainless steel," *Materials Science and Engineering: A*, vol. 552, pp. 514–522, 2012. 1

[11] A. R. Razali and Y. Qin, "A review on micro-manufacturing, micro-forming and their key issues," *Procedia Engineering*, vol. 53, pp. 665–672, 2013. 1, 4, 97

[12] C. Sudarsan, K. S. Prasad, S. Hazra, and S. K. Panda, "Forming of serpentine micro-channels on ss304 and aa1050 ultra-thin metallic sheets using stamping technology," *Journal of Manufacturing Processes*, vol. 56, pp. 1099–1113, 2020. 1, 82

[13] D. Banabic, *Sheet metal forming processes: constitutive modelling and numerical simulation*. Springer Science & Business Media, 2010. 1, 2

[14] B. K. Chun, H. Y. Kim, and J. K. Lee, "Modeling the bauschinger effect for sheet metals, part ii: applications," *International Journal of Plasticity*, vol. 18, no. 5-6, pp. 597–616, 2002. 2, 98

[15] W. Chen, Z. Liu, B. Hou, and R. Du, "Study on multi-stage sheet metal forming for automobile structure-pieces," *Journal of Materials Processing Technology*, vol. 187, pp. 113–117, 2007. 2, 98

[16] H. J. Bong, J. w. Lee, J. H. Kim, F. Barlat, and M. G. Lee, "Two-stage forming approach for manufacturing ferritic stainless steel bipolar plates in pem fuel cell: Experiments and numerical simulations," *International Journal of Hydrogen Energy*, vol. 42, no. 10, pp. 6965–6977, 2017. 2, 98

[17] M. Samuel, "Experimental and numerical prediction of springback and side wall curl in u-bendings of anisotropic sheet metals," *Journal of Materials Processing Technology*, vol. 105, no. 3, pp. 382–393, 2000. 2

[18] R. Cusset, F. Azzouz, J. Besson, M. Dragon-Louiset, V. Jacques, and H. Proudhon, "Modeling plasticity of an aluminum 2024t351 thick rolled plate for cold forming applications," *International Journal of Solids and Structures*, vol. 202, pp. 463–474, 2020. 2

[19] H. Bunge, K. Pöhlandt, and A. E. Tekkaya, *Formability of metallic materials: plastic anisotropy, formability testing, forming limits*. Springer Science & Business Media, 2000. 2

[20] F. Barlat, J. Brem, J. Yoon, K.Chung, R. Dick, D. Lege, F. Pourboghrat, S. Choi, and E. Chu, "Plane stress yield function for aluminum alloy sheets—part 1: theory," *International Journal of Plasticity*, vol. 19, no. 9, pp. 1297–1319, 2003. 2, 3, 33, 35, 38, 39, 45, 60

[21] F. Barlat and D. Kim, "Advanced constitutive modeling and application to industrial forming processes," *MATEC Web of Conferences (NUMIFORM2016)*, vol. 80, p. 15013, 2016. 2

[22] K. Li, W. Carden, and R. Wagoner, "Simulation of springback," *International Journal of Mechanical Sciences*, vol. 44, no. 1, pp. 103–122, 2002. 2, 98, 115

[23] I. Ragai, D. Lazim, and J. A. Nemes, "Anisotropy and springback in draw-bending of stainless steel 410: experimental and numerical study," *Journal of Materials Processing Technology*, vol. 166, no. 1, pp. 116–127, 2005. 2, 98

[24] R. Wagoner and M. Li, "Simulation of springback: through-thickness integration," *International Journal of Plasticity*, vol. 23, no. 3, pp. 345–360, 2007. 2, 98

[25] H. S. Kim and M. Koç, "Numerical investigations on springback characteristics of aluminum sheet metal alloys in warm forming conditions," *journal of materials processing technology*, vol. 204, no. 1-3, pp. 370–383, 2008. 2, 98

[26] S. Panthi, N. Ramakrishnan, M. Ahmed, S. S. Singh, and M. Goel, "Finite element analysis of sheet metal bending process to predict the springback," *Materials & Design*, vol. 31, no. 2, pp. 657–662, 2010. 2, 98

[27] B. Haddag, T. Balan, and F. Abed-Meraim, "Investigation of advanced strain-path dependent material models for sheet metal forming simulations," *International Journal of Plasticity*, vol. 23, no. 6, pp. 951–979, 2007. 2, 98

[28] T. Clausmeyer, A. Güner, A. E. Tekkaya, V. Levkovitch, and B. Svendsen, "Modeling and finite element simulation of loading-path-dependent hardening in sheet metals during forming," *International Journal of Plasticity*, vol. 63, pp. 64–93, 2014. 2, 98

[29] A. Wang, K. Zhong, O. El Fakir, J. Liu, C. Sun, L. L. Wang, J. Lin, and T. A. Dean, "Springback analysis of aa5754 after hot stamping: experiments and fe modelling," *The International Journal of Advanced Manufacturing Technology*, vol. 89, no. 5-8, pp. 1339–1352, 2017. 2, 98, 115

[30] M. Ardeljan, I. J. Beyerlein, B. A. McWilliams, and M. Knezevic, "Strain rate and temperature sensitive multi-level crystal plasticity model for large plastic deformation behavior: Application to az31 magnesium alloy," *International Journal of Plasticity*, vol. 83, pp. 90–109, 2016. 2, 4, 67

[31] C. K. C. Lieou and C. A. Bronkhorst, "Thermodynamic theory of crystal plasticity: formulation and application to polycrystal fcc copper," *Journal of the Mechanics and Physics of Solids*, vol. 138, p. 103905, 2020. 2, 4, 67

[32] G. Taylor, "The mechanism of plastic deformation of crystals. part i.—theoretical," *Proceedings of the Royal Society of London. Series A, Containing Papers of a Mathematical and Physical Character*, vol. 145, no. 855, pp. 362–387, 1934. 2, 4, 67

[33] J. Bishop and R. Hill, "Cxxviii. a theoretical derivation of the plastic properties of a polycrystalline face-centred metal," *The London, Edinburgh, and Dublin Philosophical Magazine and Journal of Science*, vol. 42, no. 334, pp. 1298–1307, 1951. 2, 4

[34] R. Hill, "A theory of the yielding and plastic flow of anisotropic metals," *Proceedings of the Royal Society of London. Series A. Mathematical and Physical Sciences*, vol. 193, no. 1033, pp. 281–297, 1948. 2, 3, 7, 8, 9, 33, 39, 67, 70, 89

[35] R.Hill, *The Mathematical Theory of Plasticity*. Oxford: Clarendon Press, 1950. 2, 3, 7, 9, 33, 67, 70, 89

[36] M. Gotoh, "A theory of plastic anisotropy based on a yield function of fourth order (plane stress state)—i," *International Journal of Mechanical Sciences*, vol. 19, no. 9, pp. 505–512, 1977. 2, 3, 33, 34, 38, 39, 45, 48, 60, 67

[37] D. Rees, "A tensor function for the r-value of sheet metal," *Applied Mathematical Modelling*, vol. 21, no. 9, pp. 579–590, 1997. 3

[38] J. Min, J. E. Carsley, J. Lin, Y. Wen, and B. Kuhlenkötter, "A non-quadratic constitutive model under non-associated flow rule of sheet metals with anisotropic hardening: modeling and experimental validation," *International Journal of Mechanical Sciences*, vol. 119, pp. 343–359, 2016. 3

[39] K. Wang, J. Li, T. B. Stoughton, J. E. Carsley, and B. E. Carlson, "Effect of preform annealing on plastic anisotropy of an age-hardenable al-mg-si alloy," *Journal of Materials Processing Technology*, vol. 252, pp. 381–388, 2018. 3

[40] F. Barlat, J. W. Yoon, and O. Cazacu, "On linear transformations of stress tensors for the description of plastic anisotropy," *International Journal of Plasticity*, vol. 23, no. 5, pp. 876–896, 2007. 3, 33, 35, 36, 56, 60

[41] H. Aretz, "A non-quadratic plane stress yield function for orthotropic sheet metals," *Journal of Materials Processing Technology*, vol. 168, no. 1, pp. 1–9, 2005. 3, 35, 36, 45, 60

[42] E. Schmid and W. Boas, "Plasticity of crystals," 1950. 4, 67

[43] R. Hill, "Generalized constitutive relations for incremental deformation of metal crystals by multislip," *Journal of the Mechanics and Physics of Solids*, vol. 14, no. 2, pp. 95–102, 1966. 4, 67

[44] R. Asaro, "Micromechanics of crystals and polycrystals," *Advances in Applied Mechanics*, vol. 23, pp. 1–115, 1983. 4, 67

[45] J. L. Bassani, "Plastic flow of crystals," *Advances in Applied Mechanics*, vol. 30, pp. 191–258, 1993. 4

[46] M. A. Sutton, J. J. Orteu, and H. Schreier, *Image correlation for shape, motion and deformation measurements: basic concepts, theory and applications*. Springer Science & Business Media, 2009. 5

[47] F. Q. Zhong, P. P. Indurkar, and C. G. Quan, "Three-dimensional digital image correlation with improved efficiency and accuracy," *Measurement*, vol. 128, pp. 23–33, 2018. 5

[48] W. Hosford and R. Caddell, *Metal Forming: Mechanics and Metallurgy. 2nd Edition*. Englewood Cliffs, New Jersey: Prentice Hall, 1983. 7, 8, 9

[49] J. Newby and B. Niemeier, Eds., *Formability of Metallic Materials—2000 A.D.* ASTM, Philadelphia, PA: ASTM Special Technical Publication No.753, 1982. 7, 9

[50] S. Kalpakjian, *Manufacturing Processes for Engineering Materials. 2nd Edition.* Reading, Massachusetts: Addison-Wesley, 1991. 7

[51] W. F. Hosford, *The Mechanics of Crystals and Textured Polycrystals.* Oxford: Oxford University Press, 1993. 7, 9

[52] J. Detraux, A. Dogui, and H. Gaaloul, "Some results about the use of orthotropic elastoplasticity for sheet metal forming," in *Large Plastic Deformations—Fundamental Aspects and Applications to Metal Forming*, ser. MECAMAT'91, Balkema, Rotterdam, C. Teodosiu, J. Raphanel, and E. Sidoroff, Eds., 1993, pp. 387–393. 8

[53] H. Wu, H. Hong, and Y. Shiao, "Anisotropic plasticity with application to sheet metals," *International Journal of Mechanical Sciences*, vol. 41, pp. 703–724, 1999. 8

[54] J. Britt, R. Labrecque, and K. Murty, "Mechanical anisotropy and crystallographic texture in tiaimn alloy sheet," in *Advances in Engineering Plasticity and its Applications*, ser. Elsevier Science Publishers B.V., W. Lee, Ed., 1993, pp. 387–393. 9

[55] W. Tong, "On the measurement of plastic flow anisotropy of sheet metals," *Reports of Research in Mechanics of Solids and Materials Science. Department of Mechanical Engineering, Yale Unviersity, New haven, Connecticut*, 2001. 10, 17

[56] B. Smith, X. Li, and W. Tong, "Error assessment of strain mapping by digital image correlation," *Esperimental Techniques*, vol. 22, no. 4, pp. 19–21, 1998. 12, 20

[57] W. Tong, "Detection of plastic deformation patterns in a binary aluminum alloy," *Experimental Mechanics*, vol. 37, no. 4, pp. 452–459, 1997. 12

[58] W. Tong, "Strain characterization of propagative deformation bands," *Journal of the Mechanics and Physics of Solids*, vol. 46, no. 10, pp. 2087–2102, 1998. 12

[59] G. Yang, J. Sheng, W. Tong, B. E. Carlson, H. Wang, and R. Kovacevic, "Tensile behavior of fusion-brazed aluminum alloy coach-peel joints fabricated by a dual-beam laser," *Journal of Materials Processing Tech.*, vol. 261, pp. 184–192, 2018. 19

[60] W. Tong, M. Alharbi, and J. Sheng, "On the new shear constraint for plane-stress orthotropic plasticity modeling of sheet metals," *Experimental Mechanics*, vol. 60, no. 7, pp. 889–905, 2020. 19, 34

[61] J. Blaber, B. Adair, and A. Antoniou, "Ncorr: Open-source 2D digital image correlation Matlab software," *Experimental Mechanics*, vol. 55, no. 6, pp. 1105–1122, 2015. 22

[62] W. Tong, "Formulation of Lucas–Kanade digital image correlation algorithms for non-contact deformation measurements: a review," *Strain*, vol. 49, pp. 313–334, 2013. 22

[63] B. Pan, K. Li, and W. Tong, "Fast, robust and accurate digital image correlation calculation without redundant computation," *Experimental Mechanics*, vol. 53, pp. 1277–1289, 2013. 22

[64] R. Hill, "Theoretical plasticity of textured aggregates," *Mathematical Proceedings of the Cambridge Philosophical Society*, vol. 85, pp. 179–191, 1979. 33

[65] R. Hill, "Constitutive modelling of orthotropic plasticity in sheet metals," *Journal of the Mechanics and Physics of Solids*, vol. 38, no. 3, pp. 405–417, 1990. 33, 35, 60

[66] S. Soare, J. Yoon, and O. Cazacu, "On the use of homogeneous polynomials to develop anisotropic yield functions with applications to sheet forming," *International Journal of Plasticity*, vol. 24, no. 6, pp. 915–944, 2008. 33, 38, 39, 45, 60, 61

[67] W. Tong, "Algebraic convexity conditions for gotoh's nonquadratic yield function," *Journal of Applied Mechanics*, vol. 85, no. 7, 2018. 33, 38, 40, 41, 42, 60, 61

[68] F. Yoshida and H. H. T. Uemori, "A user-friendly 3d yield function to describe anisotropy of steel sheets," *International Journal of Plasticity*, vol. 45, pp. 119–139, 2013. 33, 34, 60

[69] S. Soare and F. Barlat, "Convex polynomial yield functions," *Journal of the Mechanics and Physics of Solids*, vol. 58, no. 11, pp. 1804–1818, 2010. 34, 38

[70] T. Kuwabaraa, K. Hashimoto, E. Iizuka, and J. W. Yoon, "Effect of anisotropic yield functions on the accuracy of hole expansion simulations," *Journal of Materials Processing Technology*, vol. 211, pp. 475–481, 2011. 34, 45, 48, 56, 60

[71] W. Tong and M. Alharbi, "Comparative evaluation of non-associated quadratic and associated quartic plasticity models for orthotropic sheet metals," *International Journal of Solids and Structures*, vol. 128, pp. 133–148, 2017. 34, 38, 41, 43, 60, 61, 62

[72] W. Tong, "An improved method of determining Gotoh's nine material constants for a sheet metal with only seven or less experimental inputs," *International Journal of Mechanical Sciences*, vol. 140, pp. 394–406, 2018. 34, 35, 38, 39, 41, 43, 45, 46, 47, 54, 55, 56

[73] B. Sener, E. S. Kilicarslan, and M. Firat, "Modelling anisotropic behavior of aisi 304 stainless steel sheet using a fourth-order polynomial yield function," *Procedia Manufacturing*, vol. 47, pp. 1456–1461, 2020. 34, 59, 60

[74] R. Uppaluri and D. Helm, "A convex fourth order yield function for orthotropic metal plasticity," *European Journal of Mechanics / A Solids*, vol. 87, p. 104196, 2021. 34, 38, 45, 59, 60, 61, 62, 66

[75] R. Hill, "Basic stress analysis of hyperbolic regimes in plastic media," in *Mathematical Proceedings of the Cambridge Philosophical Society*, vol. 88, no. 2. Cambridge University Press, 1980, pp. 359–369. 35

[76] W.Tong, "Generalized fourth-order hill's 1979 yield function for modeling sheet metals in plane stress," *Acta Mechanica*, vol. 227, no. 10, pp. 2719–2733, 2016. 35, 39, 41, 56

[77] W. Tong, "On the parameter identification of polynomial anisotropic yield functions," *ASME Journal of Manufacturing Science and Engineering*, vol. 138, pp. 071 002–1–071 002–8, 2016. 38, 39, 45, 56, 61

[78] W. Tong, "On the certification of positive and convex gotoh's fourth-order yield function," in *Journal of Physics: Conference Series*, vol. 1063, no. 1. IOP Publishing, 2018, p. 012093. 38, 41, 42, 60

[79] W. Tong, "Application of Gotoh's orthotropic yield function for modeling advanced high-strength steel sheets," *ASME Journal of Manufacturing Science and Engineering*, vol. 138, pp. 094 502–1–094 502–5, 2016. 43, 48, 60

[80] W. Hu, "Constitutive modeling of orthotropic sheet metals by presenting hardening-induced anisotropy," *International journal of plasticity*, vol. 23, no. 4, pp. 620–639, 2007. 45

[81] T. Aamaishi, H. Tsutamori, E. Iizuka, K. Sato, Y. Ogihara, and Y. Matsui, "A yield function for anisotropic sheet material described by 3rd-degree spline curve and its applications," *Key Engineering Materials*, vol. 725, pp. 653–658, 2017. 48

[82] T. van den Boogaard, J. Havinga, A. Belin, and F. Barlat, "Parameter reduction for the yld2004-18p yield criterion," *International journal of material forming*, vol. 9, no. 2, pp. 175–178, 2016. 56

[83] J. Jackiewicz, "Assessing coefficients of the barlat yield criterion for anisotropic aluminum alloy sheets by means of the evolutionary strategy," *Materials and manufacturing processes*, vol. 24, no. 3, pp. 375–383, 2009. 60

[84] W. Tong, "Calibration of a complete homogeneous polynomial yield function of six degrees for modeling orthotropic steel sheets," *Acta Mechanica*, vol. 229, no. 6, pp. 2495–2519, 2018. 62

[85] J. F. W. Bishop and R. Hill, "Cxxviii. a theoretical derivation of the plastic properties of a polycrystalline face-centred metal," *The London, Edinburgh, and Dublin Philosophical Magazine and Journal of Science*, vol. 42, no. 334, pp. 1298–1307, 1951. 67, 72, 85

[86] J. L. Bassani, "Plastic flow of crystals," *Advances in applied mechanics*, vol. 30, pp. 191–258, 1993. 67

[87] S. Harren, T. C. Lowe, R. J. Asaro, and A. Needleman, "Analysis of large-strain shear in rate-dependent face-centred cubic polycrystals: correlation of micro-and macromechanics," *Philosophical Transactions of the Royal Society of London. Series A, Mathematical and Physical Sciences*, vol. 328, no. 1600, pp. 443–500, 1989. 67

[88] L. Anand and M. Kothari, "A computational procedure for rate-independent crystal plasticity," *Journal of the Mechanics and Physics of Solids*, vol. 44, no. 4, pp. 525–558, 1996. 67

[89] T. Mánik and B. Holmedal, "Review of the taylor ambiguity and the relationship between rate-independent and rate-dependent full-constraints taylor models," *International Journal of Plasticity*, vol. 55, pp. 152–181, 2014. 67

[90] F. Montheillet, P. Gilormini, and J. J. Jonas, "Relation between axial stresses and texture development during torsion testing: a simplified theory," *Acta Metallurgica*, vol. 33, no. 4, pp. 705–717, 1985. 68

[91] P. Lequeu, "Comparison of crystallographic and continuum yield surfaces for textured polycrystals," Ph.D. dissertation, McGill University, 1986. 68

[92] M. Darrieulat and F. Montheillet, "A texture based continuum approach for predicting the plastic behaviour of rolled sheet," *International Journal of Plasticity*, vol. 19, no. 4, pp. 517–546, 2003. 68, 74, 78, 80, 82, 106

[93] O. Cazacu, B. Revil-Baudard, and N. Chandola, "A yield criterion for cubic single crystals," *International Journal of Solids and Structures*, vol. 151, pp. 9–19, 2018. 68, 106

[94] M. Arminjon, "A regular form of the schmid law. application to the ambiguity problem," *Textures and Microstructures*, vol. 14, pp. 1121–1128, 1991. 68

[95] W. Gambin, "Refined analysis of elastic-plastic crystals," *International journal of solids and structures*, vol. 29, no. 16, pp. 2013–2021, 1992. 68

[96] M. Darrieulat and D. Piot, "A method of generating analytical yield surfaces of crystalline materials," *International journal of plasticity*, vol. 12, no. 5, pp. 575–610, 1996. 68

[97] W. Tong, H. Tao, and X. Q. Jiang, "Modeling the rotation of orthotropic axes of sheet metals subjected to off-axis uniaxial tension," *Journal of Applied Mechanics*, vol. 71, no. 4, pp. 521–531, 2004. 68, 70

[98] O. Chahaoui, M. L. Fares, D. Piot, and F. Montheillet, "Monoclinic effects and orthotropic estimation for the behaviour of rolled sheet," *Journal of Materials Science*, vol. 46, no. 6, pp. 1655–1667, 2011. 74, 80

[99] O. Chahaoui, M. Fares, D. Piot, and F. Montheillet, "Mechanical modeling of macroscopic behavior for anisotropic and heterogeneous metal alloys," *Metals and Materials International*, vol. 19, no. 5, pp. 1005–1019, 2013. 74, 80

[100] G. Nolze, "Characterization of the fcc/bcc orientation relationship by ebsd using pole figures and variants," *Z. Metallkd*, vol. 95, no. 9, pp. 744–755, 2004. 75

[101] T. P. Van, K. Jöchen, and T. Böhlke, "Simulation of sheet metal forming incorporating ebsd data," *Journal of Materials Processing Technology*, vol. 212, no. 12, pp. 2659–2668, 2012. 75

[102] T. Britton, J. Jiang, Y. Guo, A. Vilalta-Clemente, D. Wallis, L. Hansen, A. Winkelmann, and A. Wilkinson, "Tutorial: Crystal orientations and ebsd—or which way is up?" *Materials Characterization*, vol. 117, pp. 113–126, 2016. 75

[103] H. Bunge, *Texture Analysis in Material Science*. Butterworths, 1982. 76

[104] R. Hill, "Constitutive dual potentials in classical plasticity," *Journal of the Mechanics and Physics of Solids*, vol. 35, no. 1, pp. 23–33, 1987. 76

[105] M. Arminjon and B. Bacroix, "On plastic potentials for anisotropic metals and their derivation from the texture function," *Acta Mechanica*, vol. 88, pp. 219–243, 1990. 76

[106] A. Ziletti, D. Kumar, M. Scheffler, and L. M. Ghiringhelli, "Insightful classification of crystal structures using deep learning," *Nature communications*, vol. 9, no. 1, pp. 1–10, 2018. 82

[107] F. Bachmann, R. Hielscher, and H. Schaeben, "Texture analysis with mtex–free and open source software toolbox," in *Solid State Phenomena*, vol. 160. Trans Tech Publ, 2010, pp. 63–68. 82

[108] G. Sachs, "On the derivation of a condition of flowing," *Z Verein Deut Ing*, vol. 72, pp. 734–736, 1928. 85

[109] W. Tong, C. Xie, and N. Zhang, "On the micromechanical basis of an anisotropic plastic flow theory of polycrystalline sheet metals," *Technical Report (38pp)*, 2005. 85

[110] G. I. Taylor, "Plastic strain in metals," *J. Inst. Metals*, vol. 62, pp. 307–324, 1938. 85

[111] J. Bishop and R. Hill, "Xlvi. a theory of the plastic distortion of a polycrystalline aggregate under combined stresses." *The London, Edinburgh, and Dublin Philosophical Magazine and Journal of Science*, vol. 42, no. 327, pp. 414–427, 1951. 85

[112] Y. Tadano, M. Kuroda, and H. Noguchi, "Quantitative re-examination of taylor model for fcc polycrystals," *Computational materials science*, vol. 51, no. 1, pp. 290–302, 2012. 88, 89

[113] M. Kasemer, G. Falkinger, and F. Roters, "A numerical study of the influence of crystal plasticity modeling parameters on the plastic anisotropy of rolled aluminum sheet," *Modelling and Simulation in Materials Science and Engineering*, vol. 28, no. 8, p. 085005, 2020. 89

[114] Y. Jeong, F. Barlat, and M.-G. Lee, "Application of crystal plasticity to an austenitic stainless steel," *Modelling and Simulation in Materials Science and Engineering*, vol. 20, no. 2, p. 024009, 2012. 91, 92, 93

[115] A. Mayyas and M. Mann, "Emerging manufacturing technologies for fuel cells and electrolyzers," *Procedia Manufacturing*, vol. 33, pp. 508–515, 2019. 97

[116] L. Peng, D. Liu, P. Hu, X. Lai, and J. Ni, "Fabrication of metallic bipolar plates for proton exchange membrane fuel cell by flexible forming process-numerical simulations and experiments," *Journal of Fuel Cell Science and Technology*, vol. 7, no. 3, 2010. 98

[117] D. Zhang, Z. Cui, X. Ruan, and Y. Li, "An analytical model for predicting springback and side wall curl of sheet after u-bending," *Computational Materials Science*, vol. 38, no. 4, pp. 707–715, 2007. 98

[118] M. G. Lee, J. H. Kim, K. Chung, S. J. Kim, R. H. Wagoner, and H. Y. Kim, "Analytical springback model for lightweight hexagonal close-packed sheet metal," *International Journal of Plasticity*, vol. 25, no. 3, pp. 399–419, 2009. 98

[119] K. Y. Seo, J. H. Kim, H. S. Lee, J. H. Kim, and B.-M. Kim, "Effect of constitutive equations on springback prediction accuracy in the trip1180 cold stamping," *Metals*, vol. 8, no. 1, p. 18, 2018. 98, 115

[120] H. J. Bong, F. Barlat, J. Lee, M.-G. Lee, and J. H. Kim, "Application of central composite design for optimization of two-stage forming process using ultra-thin ferritic stainless steel," *Metals and Materials International*, vol. 22, no. 2, pp. 276–287, 2016. 98

[121] R. Quey, P. Dawson, and F. Barbe, "Large-scale 3d random polycrystals for the finite element method: Generation, meshing and remeshing," *Computer Methods in Applied Mechanics and Engineering*, vol. 200, no. 17-20, pp. 1729–1745, 2011. 110

[122] E. Ghazvinian, M. Diederichs, and R. Quey, "3d random voronoi grain-based models for simulation of brittle rock damage and fabric-guided micro-fracturing," *Journal of Rock Mechanics and Geotechnical Engineering*, vol. 6, no. 6, pp. 506–521, 2014. 110

[123] F. Adzima, T. Balan, and P. Manach, "Springback prediction for a mechanical micro connector using cpfem based numerical simulations," *International Journal of Material Forming*, pp. 1–11, 2019. 115, 123

[124] Z. Fang, Z. Jiang, D. Wei, and X. Liu, "Study on springback in micro v-bending with consideration of grain heterogeneity," *The International Journal of Advanced Manufacturing Technology*, vol. 78, no. 5-8, pp. 1075–1085, 2015. 115, 122

[125] Z. Xu, L. Peng, and E. Bao, "Size effect affected springback in micro/meso scale bending process: Experiments and numerical modeling," *Journal of Materials Processing Technology*, vol. 252, pp. 407–420, 2018. 115

[126] M. D. Abràmoff, P. J. Magalhães, and S. J. Ram, "Image processing with imagej," *Biophotonics international*, vol. 11, no. 7, pp. 36–42, 2004. 116

[127] T. J. Collins, "Imagej for microscopy," *Biotechniques*, vol. 43, no. S1, pp. S25–S30, 2007. 116

[128] S. Zang, J. Liang, and C. Guo, "A constitutive model for spring-back prediction in which the change of young's modulus with plastic deformation is considered," *International Journal of Machine Tools and Manufacture*, vol. 47, no. 11, pp. 1791–1797, 2007. 123

[129] Z. Cinar, M. Asmael, Q. Zeeshan, and B. Safaei, "Effect of springback on a6061 sheet metal bending: a review," *J Kejuruteraan*, vol. 33, no. 1, pp. 13–26, 2021. 123